Spring 2020

Molecular Spectroscopy: A Study of Molecules in Earth and Planetary Atmospheres

Mahdi Yousefi Atashgah
Old Dominion University, myous005@odu.edu

Recommended Citation

Atashgah, Mahdi Y.. "Molecular Spectroscopy: A Study of Molecules in Earth and Planetary Atmospheres" (2020). Doctor of Philosophy (PhD), Dissertation, Physics, Old Dominion University, DOI: 10.25777/j9br-ak98
https://digitalcommons.odu.edu/physics_etds/124

MOLECULAR SPECTROSCOPY: A STUDY OF MOLECULES IN EARTH AND PLANETARY ATMOSPHERES

by

Mahdi Yousefi Atashgah
B.S. December 2007, Tabriz University, Iran
M.S. May 2011, Shahid Beheshti University, Iran
M.S. May 2015, Old Dominion University

A Thesis Submitted to the Faculty of the Department of Physics
Old Dominion University in Partial Fulfillment of the
Requirements for the Degree of

DOCTOR OF PHILOSOPHY

PHYSICS

OLD DOMINION UNIVERSITY
May 2020

Approved by:

Peter Bernath (Director)

Charles Sukenik (Member)

Lepsha Vuskovic (Member)

Alex Godunov (Member)

Craig Bayse (Member)

ABSTRACT

MOLECULAR SPECTROSCOPY: A STUDY OF MOLECULES IN EARTH AND PLANETARY ATMOSPHERES

Mahdi Yousefi Atashgah
Old Dominion University, 2020
Director: Dr. Peter Bernath

The four most abundant isotopologues (N_2O, ^{15}NNO, $N^{15}NO$, and $NN^{18}O$) of nitrous oxide have been measured in the Earth's atmosphere by infrared remote sensing with the Atmospheric Chemistry Experiment (ACE) Fourier transform spectrometer. These satellite observations have provided a near global picture of N_2O isotopic fractionation. The relative abundance of the heavier isotopologues increase with altitude and with latitude in the stratosphere as the air becomes older.

Near global 85°S–85°N atmospheric measurement of carbonyl sulfide (OCS), including the minor $OC^{34}S$ and $O^{13}CS$ isotopologues, were made by the Atmospheric Chemistry Experiment Fourier transform spectrometer (ACE-FTS) in low Earth orbit. ACE-FTS data provide volume mixing ratio (VMR) profiles of OCS, $OC^{34}S$ and $O^{13}CS$ from 8 km in the troposphere up to 31 km in the stratosphere. The global zonal and seasonal distributions of OCS isotopologues were studied. OCS observations made with the MkIV balloon-borne Fourier transform spectrometer (FTS) are also presented. The results indicate a slight enrichment of $OC^{34}S$ and a significant enrichment of $O^{13}CS$ as the altitude increases. The contribution of OCS to the background Stratospheric Sulfate Aerosol Layer (SSA) is discussed and ACE-FTS data indicate that OCS is a major contributor.

Vibration-rotation line lists for AlF, $Al^{35}Cl$ and $Al^{37}Cl$ have been prepared in their ground electronic states ($X^1\Sigma^+$). Experimental rotational and ro-vibrational lines were employed to calculate a potential energy surface (PES) by direct potential fitting. The PES was used to calculate ro-vibrational energy levels. Born-Openheimer Breakdown (BOB) corrections were included in the energy level calculations for AlCl. Ro-vibrational energy levels were calculated for the v=0 to v=11 vibrational levels and up to J_{max} =200 for the rotational levels. Dipole moment functions (DMFs) covering the range of the PES turning points were calculated for AlCl and AlF by *ab initio* methods and used to determine line intensities. Partition functions for temperatures up to 3000 K were calculated. AlF and AlCl have been detected in

circumstellar envelopes and are predicted to occur in cool stellar and sub-stellar atmospheres.

A new line list for the $A^2\Sigma^+ - X^2\Pi$ electronic transition of OH has been calculated. Line positions have been taken from the literature and refitted with Western's PGOPHER program. Line intensities were calculated using a new *ab initio* Transition Dipole Moment Function (TDMF) obtained with Molpro 2012. The new TDMF and the potential functions from LeRoy's RKR program have been used as input to LeRoy's LEVEL program in order to calculate Transition Dipole Moment Matrix Elements (TDMMEs). These matrix elements were transformed from Hund's case (b) to Hund's case (a) as required for the PGOPHER program. The line list was calculated with PGOPHER for bands with $v' = 0 - 4$ in the $A^2\Sigma^+$ state and $v'' = 0 - 9$ for the $X^2\Pi$ state.

Methane (CH_4) spectra in the ν_3 band near 3.3 μm were measured for 0 Torr, 50 Torr, 150 Torr, 240 Torr, 320 Torr, and 400 Torr pressure of added hydrogen. The spectra were recorded using a high resolution Fourier transform spectrometer. The CH_4 spectra were measured at 5 different temperatures from room temperature up to $\sim$ 1100 K. A multi-spectrum non-linear least-squares fit method was used to determine the line parameters at each temperature. Voigt lineshape functions were used to determine the broadening and shifting of methane lines in the P and R branches. Additionally, Hartmann–Tran lineshape functions (quadratic Speed-Dependent Hard Collision, qSDHC, including line mixing) were used to measure speed dependent line shifting. Temperature-dependence of coefficients were determined from a fit of line parameters as a function of temperature. Finally, the dependence of pressure broadening (γ_0) and shift (δ_0) parameters on the rotational quantum number (J) was studied.

ACKNOWLEDGEMENTS

First of all, I would like to show my gratitude to my advisor, Dr. Peter Bernath for his support and guidance in each step of my Ph.D. research. His outstanding lectures and discussions gave me perspective, and his guidance helped me to finish my graduate studies successfully and grow as a research scientist.

I would also like to express my gratitude to the Physics Department at Old Dominion University for their support.

I should express my love and gratitude to my parents, sisters, and brother who have always supported and loved me. My love for them is unconditional and making them happy is my priority in life. Finally, I like to show my love and gratitude to my grandmother who passed away while I was in the US and far away from her. I could not meet her one last time. She was a mother to me. She brought me up and loved me unconditionally. I will always love her and remember her.

TABLE OF CONTENTS

Page

Chapter

LIST OF TABLES

LIST OF FIGURES

Figure Page

CHAPTER 1

INTRODUCTION

The observation of planetary atmospheres has utilized electromagnetic radiation in the visible, infrared, and microwave regions of the spectrum. Earth's atmosphere is opaque for most of the radiation, especially ultraviolet radiation coming from outer space. However, the narrow "windows" in the infrared region, where the atmosphere is transparent, have created a unique opportunity to obtain information about molecular constituents, temperatures, cloud compositions, atmospheric pressure, and other physical properties of the planetary atmospheres.

Spectroscopy is the most useful method for the remote observation and probing of physical properties of planetary objects. In recent years there have been growing discoveries of exoplanets (e.g. hot Jupiters). The infrared range provides the possibility of probing the atmosphere of exoplanets. These observations have been made by the Spitzer/IRAC-IRSMIPS and the Hubble Space Telescope/NICMOS-WFC3 from space and also from ground based telescopes (VLT, IRTF, Keck). While the spectra measured using ground and space based telescopes are invaluable for studying of planetary objects, there are some limitations to spectral observations. For example, high resolution spectra observations have implicit complexity by nature, while low resolution spectra, due to instrument limitations, decrease the complexity. That deficit can mask real details that would decrease ambiguity to the interpretation. This makes the extraction of quantitative information difficult. Ground and space based observations can be complemented by high resolution laboratory Fourier transform spectroscopy to reduce this deficit.

One example is the spectra of Saturn shown in Figure 1, measured by Larson et al. [1] which does not show any evidence for the existence of NH_3, even though it is

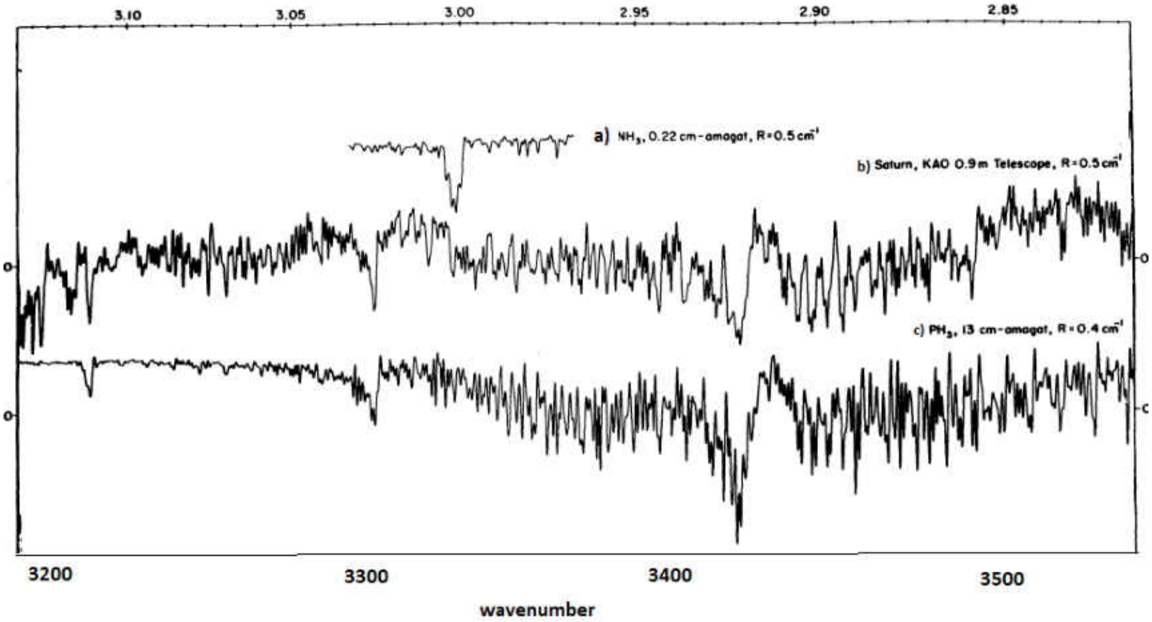

FIG. 1: High resolution spectra of Saturn obtained by KAO telescope indicating the presence of PH_3, but, unexpectedly, NH_3 is not detected [1].

commonly assumed that clouds on Saturn are NH_3 ice crystals. Later, Larson et al. measured the spectrum of PH_3 in the laboratory and compared it to the spectrum of Saturn in order to determine PH_3 abundance on Saturn. This problem illustrates that more complex molecular bands must be analyzed to determine abundances and physical quantities of the atmosphere. Some of the most important parameters include energy levels (line positions), line intensity, collision induced line broadening, and line shift coefficients.

Another important molecule is methane (CH_4), the main carbon bearing molecule, which, after water, is the most important opacity source in the atmosphere of exoplanets (see Figure 2). In the exoplanets' atmospheres, CH_4 experiences collisions with H_2 (like giant planets) or N_2 (like Titan). This results in a pressure induced broadening and line shifting of CH_4. In order to obtain a better CH_4 molecular abundance on these exoplanets, a set of quantitative physical parameters of methane are required. To obtain these parameters, high resolution infrared spectra of methane broadened by H_2 or N_2 molecules are necessary. As the part of my dissertation, I studied the collision induced line broadening and shifting of hot methane that is reported in Chapter 8.

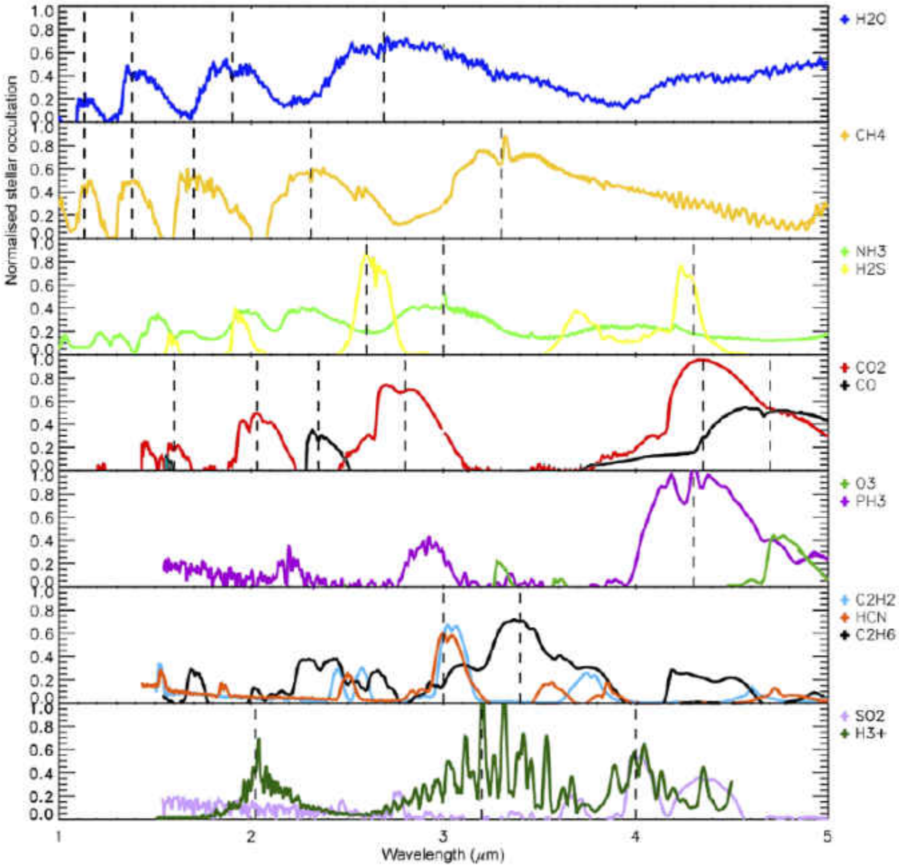

FIG. 2: Absorptions contributions from different molecules in the transmission spectrum of a hot, gaseous exoplanet [2].

Infrared spectroscopy can also help to understand the physics of evolution of stars. One example is the carbon rich (C-rich) asymptotic giant branch stars (AGB). Studying the spectra from carbon rich stars (e.g. IRC+10216) in particular can provide key information about mass loss process in the stars. AlCl and AlF are two molecules that were predicted in the atmosphere of C-rich and O-rich stars. While the spectra obtained from these stars show the existence of AlF and AlCl, accurate vibrational-rotational linelists of these diatomic molecules are required to better understand the physical processes in these stars. A laboratory infrared spectrum of these molecules that covers vibrational-rotational transitions is essential for calculating a reliable linelist. As the part of my dissertation, I calculated a new vibrational-rotational linelist for AlF and AlCl using the spectra obtained by Zhang et al. [97] and Hedderich et al. [80] that is reported in Chapter 6.

Some other molecules have importance in atmospheric science and astrophysics because of their presence in the Earth's atmosphere and the interstellar medium. One example is the OH radical. Although OH electronic states have been extensively studied, there is still a need to understand the contribution of higher rotational states to the intensity of OH lines. This requires accurate laboratory measurements of OH spectra, as well as computational approaches, in order to determine the transition dipole moment of OH between its electronic states. As the part of my dissertation, I calculated an updated linelist for the electronic A–X transition of OH that is reported in Chapter 7.

Infrared spectroscopy is the most important tool in the remote sensing of Earth's atmosphere. There are several satellites with FTS instruments on board for atmospheric measurements. Two examples are the ACE-FTS high resolution Fourier transform spectrometer on board the Atmospheric Chemistry Experiment (ACE) satellite and the MIPAS high resolution Fourier-transform spectrometer on board ENVISAT.

The ACE-FTS spectrometer on board the ACE satellite measures atmospheric trace molecules using the Sun as the source in the limb geometry. The ACE-FTS also measures the heavier isotopologues of trace molecules in the atmosphere. One can gain information about atmospheric dynamics, sources, and sinks of these molecules by measuring the isotopic composition of these molecules in the stratosphere. As the part of my dissertation, I measured N_2O and its heavier isotopologues which are a potent greenhouse gases, and OCS and its heavy isotopologues, which are responsible for sulfate aerosol in the stratosphere. My goal is to measure the enrichment of heavier isotopologues of N_2O and OCS molecules.

CHAPTER 2

ATMOSPHERIC BACKGROUND

2.1 Introduction

This chapter provides the scientific background utilized for the study of global stratospheric distribution of nitrous oxide (N_2O) and its heavier isotopologues (Chapter 4), as well as global stratospheric distribution of carbonyl Sulfide (OCS) and its heavier isotopologues (Chapter 5).

2.2 Earth atmospheric structure and composition

2.2.1 Atmospheric composition

The Earth's atmosphere mainly consist of gases such as molecular nitrogen (N_2) [78.08%], molecular oxygen (O_2) [20.98%], and a small amount of argon (Ar) [0.93%], which make up more than 99.9 % of dry air. Other gases, which exist in trace amounts from part per million to part per trillion, include the greenhouse gases such as, CO_2, CH_4, and N_2O are listed in Table 1.

These trace gases are important in terms of regulating the Earth's climate. For example, greenhouse gases increase the Earth's surface temperature to about 288 K [4] by absorbing sunlight that would otherwise escape from the atmosphere out into space, making it possible for life on Earth. The ability of greenhouse gases to be transparent to the inbound visible light from the Sun yet opaque to the energy radiated from the Earth makes them crucial for life on Earth. Since the industrial revolution, human activities such as energy production, agriculture, and so on, have increasingly added greenhouse gases to the atmosphere. This increased

TABLE 1: Atmospheric gas constituents

Gas (Symbol)	Content
Nitrogen (N_2)	78.084%
Argon (Ar)	0.934%
Carbon dioxide (CO_2)	0.033%
Neon (Ne)	18.20 ppm
Helium (He)	5.20 ppm
Krypton (Kr)	1.10 ppm
Sulfur dioxide (SO_2)	1.00 ppm
Methane (CH_4)	2.00 ppm
Nitrous oxide (N_2O)	0.5 ppm
Xenon (Xe)	0.09 ppm

the greenhouse effect, which, in turn, led to an increased average surface temperature. A stronger greenhouse effect will lead to changes in the global climate pattern and warm up Earth's atmosphere. Some of the consequences would be warming the oceans, partially melting glaciers, increasing sea levels, and heavy rainfall. Therefore, monitoring and controlling anthropocentric emissions into the atmosphere, including greenhouse gases, has become increasingly crucial.

In contrast to greenhouse gases, aerosol particle emissions backscatter solar radiation and contribute to a global mean negative radiative forcing of about -0.5 W m^{-2}, enhanced by a factor of two or more by indirect effects of the particles on clouds [3]. Sulfur containing gases such as OCS and SO_2 are two of the major molecules contributing to the stratospheric aerosols.

2.2.2 Atmospheric vertical structure

The vertical distribution of temperature, pressure, density, and composition of the atmosphere constitutes atmospheric structure. The Earth's atmosphere is composed of multiple layers. These layers, starting from the surface, are called the troposphere, the stratosphere, the mesosphere, the thermosphere, and the exosphere. They are separated based on the vertical temperature profile (see Figure 3). The atmospheric pressure decreases approximately exponentially, expressed by $P(z)=P(0)e^{-z/H}$ where

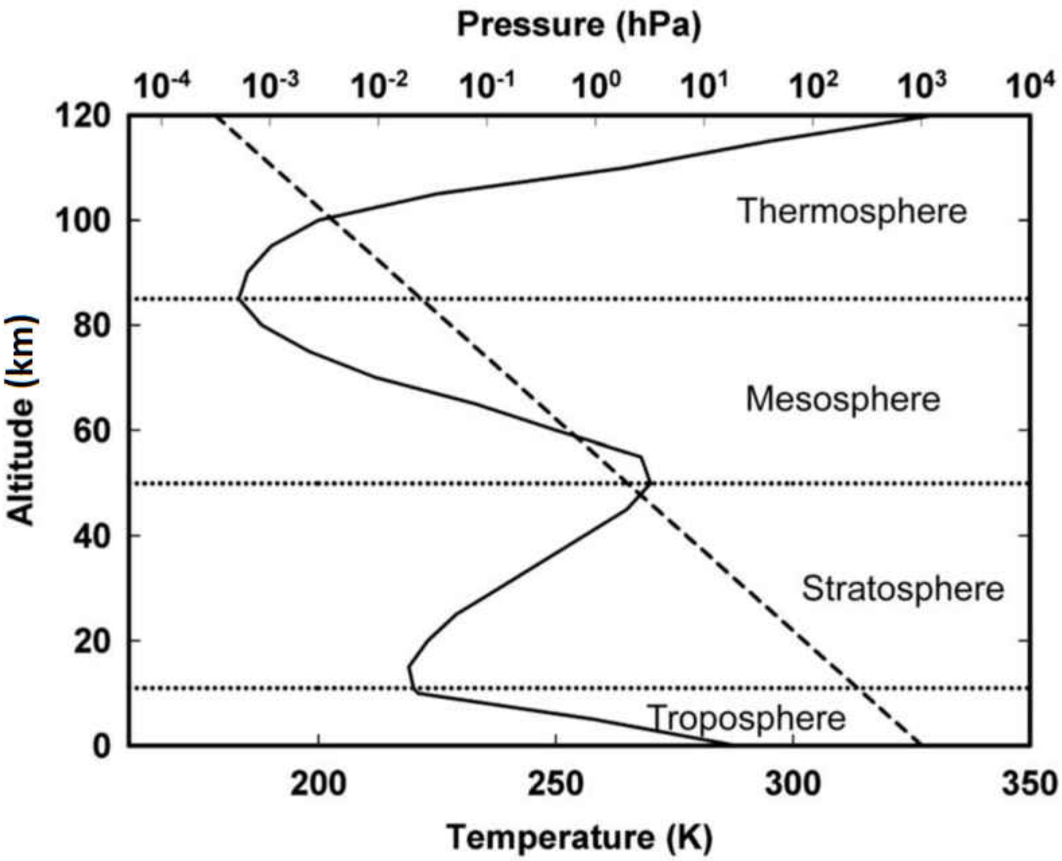

FIG. 3: Layers of atmosphere and their temperature (solid line) and pressure (dash line) structure with altitude (top scale, base 10 logarithms) where 1 standard atmosphere=1013 hPa [5]

P(0) is the pressure at the surface, P(z) is the pressure at altitude z, and H is atmospheric scale height. This shows an exponential decrease of atmospheric pressure as altitude increases. As a result, 99.999 % of the air mass is below an altitude of 80 km.

2.2.2.1 The troposphere

The troposphere is the atmospheric layer closest to the Earth's surface and contains the largest percentage (around 80%) of the mass of the total atmosphere. Its depth extends from the surface to altitudes ranging from 8 to 18 km. Essentially, all weather, such as precipitation, winds, storms, and clouds (except a few observed in the stratosphere and mesosphere) occurs in the troposphere. The density and the temperature of the troposphere decrease as the altitude increases (see Figure

3). The air motion in the troposphere is controlled by the turbulence that is caused by the uneven heating of Earth's surface by sunlight and keeps the tropospheric air well mixed. The layer that separates the troposphere and the stratosphere is called the tropopause, which is an isothermal layer that extends above the troposphere. The tropopause acts as a barrier against the air rising from the troposphere into the stratosphere.

2.2.2.2 The stratosphere

The stratosphere lies above the tropopause and extends from about 20 to 48 km above the surface. Compared to the troposphere, the stratosphere has significantly less air density (about one thousandth of that at sea level) with less water vapor, which leads to dryer air. Temperature increases in the stratosphere because of the presence of ozone (O_3) molecules that absorb ultraviolet sunlight. This creates the strong temperature inversion characteristic of the stratospheric layer, in which vertical mixing is slow, unlike the troposphere.

2.2.2.3 Mesosphere

The mesosphere extends from above the stratosphere (stratopause) to altitudes of about 85 km. With increasing altitude in the mesosphere, the temperature decreases. The coldest temperatures in Earth's atmosphere occur at the top of this layer.

2.2.2.4 The thermosphere

The thermosphere extends from above the mesopause up to altitudes about 500 km. The thermosphere is characterized by the rapid increase in temperature that results from the absorption of short wavelength radiation by N_2 and O_2.

2.3 Atmospheric circulation

Because Earth is a rotating system, air moving in a horizontal direction is deflected by a Coriolis force. For instance, consider air moving in the northern hemisphere, where Earth's rotation is counterclockwise, as it is presented in Figure 4. As the air parcel moves from the equator, where the Coriolis force is zero, it deflects eastward, moving towards the poles, where the Coriolis force is maximum. The

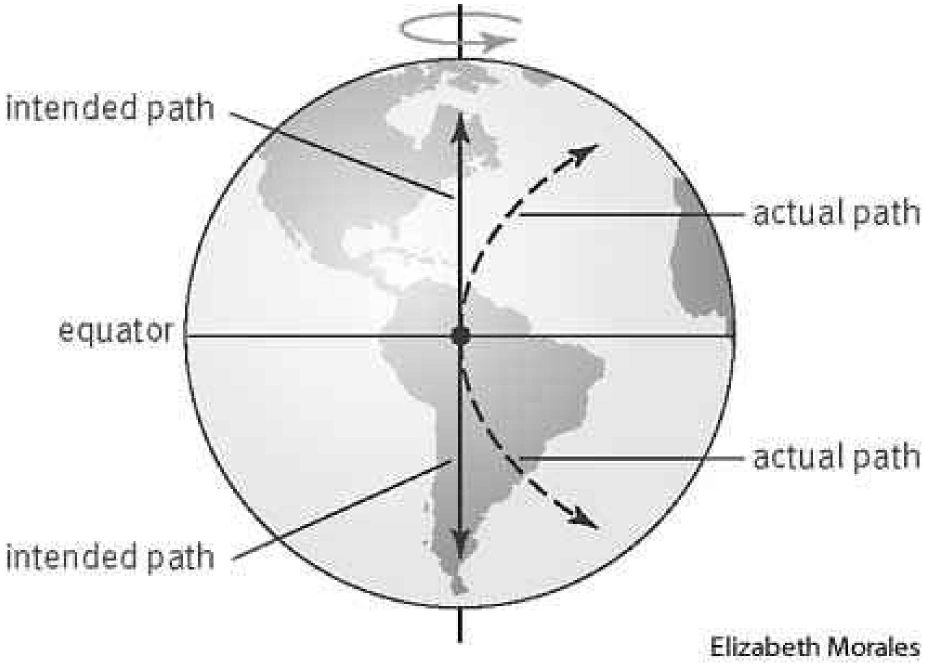

FIG. 4: Illustration of the Coriolis force in the Northern Hemisphere [6].

winds in the northern hemisphere deflect to the right of their intended path because of Coriolis force. This effect reverses in the southern hemisphere.

Air masses also move along pressure gradients from high to low pressure. Consider an air parcel in the northern hemisphere that moves as the result of the pressure gradient (see Figure 5). As the air parcel acquires speed, the increasing Coriolis force deflects it to the right, until eventually these two forces cancel each other out, leading to the steady flow of air.

Another existing force is friction, which becomes important at the surface, where it reduces the Coriolis effect by decreasing air velocity. This causes the vertical flow of air at the pressure center. This vertical flow is upwelling for the low pressure center and downwelling for the high pressure center (see Figure 6).

Meridional air flow is mainly governed by the temperature difference between the equator and the poles. The warm air at the equator rises upward and turns poleward at the upper troposphere. However, because of the Coriolis force, the air flow deflects, and, instead of reaching the poles, descends at around 30°, and returns to the equator. This circulation pattern is known as the Hadley cell. A similar circulation pattern, called the polar cell, at higher latitudes, causes air to ascend at

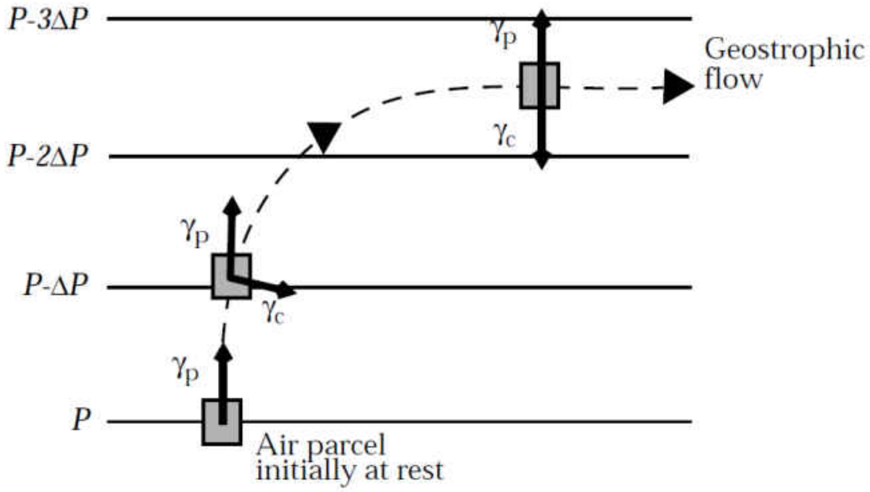

FIG. 5: Diagram of idealized geostrophic flow [4].

about 60° and to descend at the poles. Another air circulation pattern known, as the Ferell cell, is created over mid latitudes, where part of the rising air at about 60° moves toward the equator and collides with air circulation from the Hadley cell. A schematic of these air circulation cells is presented in Figure 7.

2.3.1 Stratospheric circulation

The major air circulation pattern in the stratosphere is the Brewer-Dobson circulation (BDC). A schematic of the Brewer-Dobson circulation is shown in Figure 8. The Brewer-Dobson circulation consists of a meridional circulation cell in each hemisphere, where air rises across the tropical tropopause, moves poleward, and sinks into the extratropical troposphere. Although this circulation is similar to the tropospheric circulations, its cause is more complex than thermal heating at the surface. The major known drivers of BDC are Rossby waves (waves that naturally occur in rotating fluids) and the dissipation of gravity waves across the tropopause. Note that BDC is crucial for distribution of water vapor and ozone in the stratosphere.

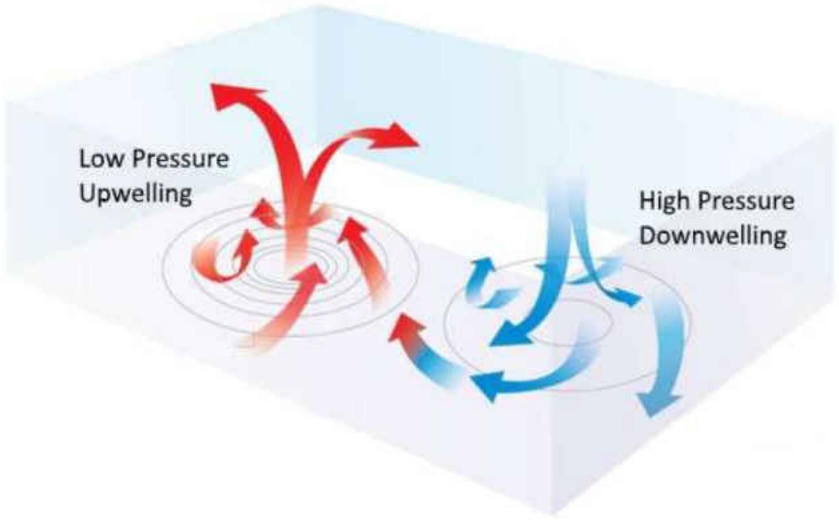

FIG. 6: Vertical motion of air resulted from non-ideal geostrophic flow [7].

2.4 Measuring the atmosphere

There are two main methods for measuring chemical composition of the atmosphere. The first method involves direct measurements of air samples for laboratory analysis. The common methods for the direct analysis are mass spectrometry, gas chromatography, and Fourier transform infrared spectroscopy. Another way of direct measurement is the *in situ* measurement of air using these instruments on the site.

The other main method is remote sensing of the atmosphere, where mainly optical spectrometers are used to measure atmospheric composition. These spectrometers can be placed on the Earth's surface, a balloon, an aircraft, or a satellite. In remote sensing, data is obtained from an object by collecting light scattered or emitted from the object. Remote sensing has become one of the most important methods of measuring the atmosphere, since most of the atmosphere is out of reach. Remote sensing makes measurements of the upper atmosphere possible and provides information such as column density, vertical profile, and so on, that is not achievable by direct measurement methods.

Two main types of remote sensing are active and passive remote sensing. In active remote sensing, the optical instrument scans an object by sending an electromagnetic (EM) wave and collecting the reflected or backscattered light from the object (e.g.,

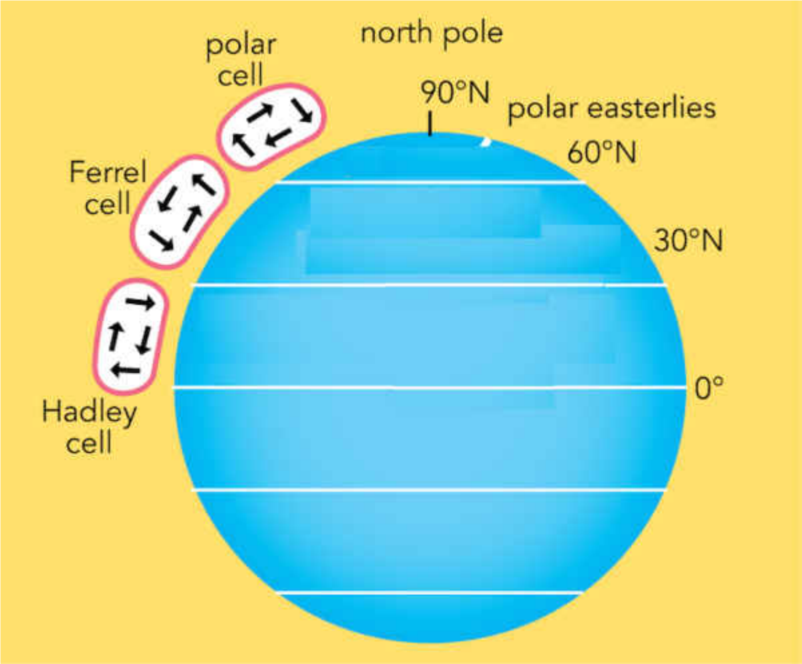

FIG. 7: Global atmospheric circulation patterns in the Northern Hemisphere (Image by Byron Inouye).

radar). In passive remote sensing, the system detects EM radiation (visible through thermal radiation) using one of two sources. In the visible to near infrared region, it uses radiation from the Sun that is reflected from Earth's surface or scattered by the atmosphere. In the infrared region, it uses thermal radiation that is emitted directly by materials on the Earth, which combines with self-emitted thermal radiation in the atmosphere as it propagates upward.

2.4.1 Atmospheric spectra and microwindows

The spectra recorded of the atmosphere show the characteristic absorption and emission features that can be used in remote sensing. Absorption of radiation is governed by the interaction between light and matter. Once radiation traverses from a medium, its intensity decreases. This decrease depends on the absorption cross section of the medium (σ_z), the number of molecules per unit volume (n), and also the path length (dz). The decrease in intensity is expressed by the Beer-Lambert

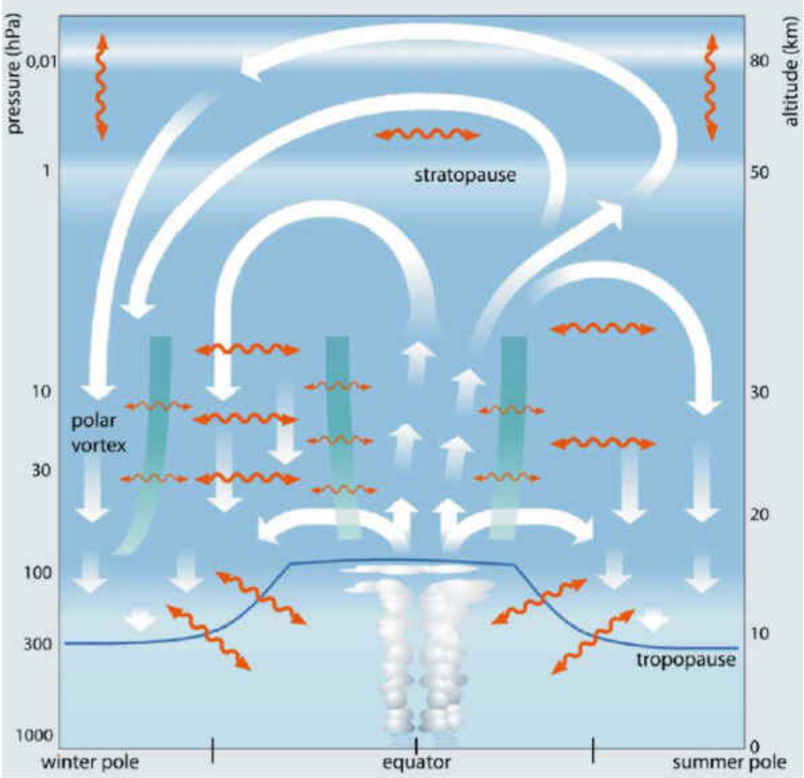

FIG. 8: Schematic of the BDC [8].

law (ignoring thermal emission)

$$I = I_0 exp(-\int_0^z n\sigma_z dz). \tag{1}$$

In the case where n is independent of z, equation 1 can be simplified to

$$I = I_0 exp(-n\sigma_z z), \tag{2}$$

a more complete expression of the Beer-Lambert law includes both scattering (σ_{sca}) and absorption (σ_{abs}) of light

$$I = I_0 exp(-n(\sigma_{sca} + \sigma_{abs})z). \tag{3}$$

Most of the radiation coming from the Sun is absorbed by molecules in the atmosphere. This prevents harmful radiation such as, x-ray or UV from reaching to the Earth's surface. In particular, the molecules of water, carbon dioxide, oxygen, and ozone in our atmosphere, block solar radiation. In contrast to absorption bands,

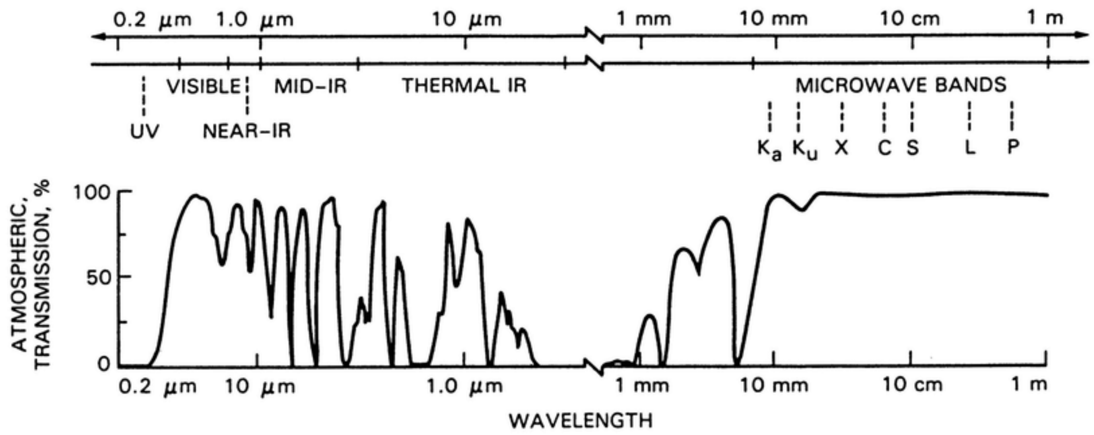

FIG. 9: Atmospheric windows in the electromagnetic spectrum [9].

there are spectral bands for which the atmosphere is transparent with little or no absorption (see Figure 9). These spectral bands are known as “atmospheric windows”, since they allow the EM to pass through the atmosphere onto the Earth’s surface. Most of the remote sensing instruments operate in one or more of these “windows” by using detectors tuned to specific frequencies.

2.4.2 Photochemistry and isotopic chemistry of the atmosphere

The atmospheric composition is determined by emissions (sources), deposition (sinks), chemical reactions, and atmospheric dynamics (transport). The major drive (directly and indirectly) of atmospheric chemistry is based on photochemical reactions. For example, the OH free radical is the primary oxidizing agent in the atmosphere, produced from the reaction of water vapor with metastable oxygen atoms $O(^1D)$, that is produced by photolysis of ozone molecules, $(O_3 + h\nu(\lambda \leq 310\,\mathrm{nm}) \longrightarrow O_2(a^1\Delta_g) + O(^1D))$. Also it is worth noting that isotopologue abundance is driven mainly by photolysis. Isotopologues are molecultes that differ in their isotopic composition. This means that they have the similar chemical formula, but at least one atom has a different atomic mass. Isotopologues with their atoms in different locations are called isotopomers.

The enrichment of isotopes can be predicted by photochemical methods, due to the difference in photolysis rates for any two isotopes at a specific wavelength. In most

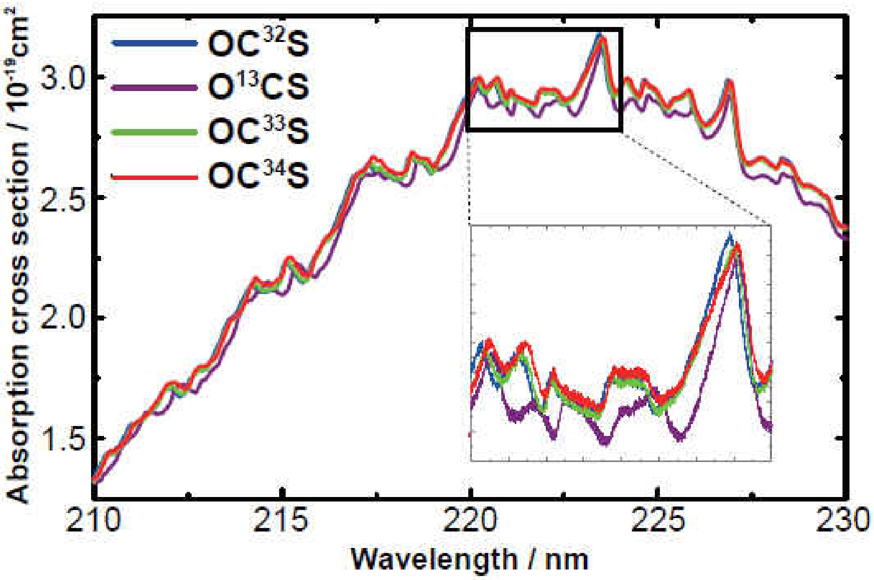

FIG. 10: Comparison of absorption cross sections of OC^{33}S, OC^{34}S, and O^{13}CS and OC^{32}S measured from 210 to 230 nm [10].

cases, the heavy isotopologues are photolyzed at a slower rate than the lighter isotopologues; therefore, as altitude increases and photochemistry by sunlight becomes more important, the atmosphere becomes more enriched in heavier isotopologues. This comes from the fact that isotopically substituted molecules exhibit different reaction rates, known as the kinetic isotope effect (KIE). To understand how isotopic mass differences results in isotopic abundance varation, it is useful to consider a harmonic oscillator model for the vibrational levels a diatomic molecule, where vibrational frequencies are inversely proportional to the square root of the reduced mass,

$$\nu = \frac{1}{2\pi}\sqrt{\frac{k}{\mu}}, \quad \mu = \frac{m_1 m_2}{m_1 + m_2}. \tag{4}$$

The vibrational energy of molecule in the ground state, known as the zero point energy (ZPE), is $E_0 = (1/2)h\nu$. Isotopic substitution results in a shift in the zero point energy. Change in the ZPE, leads to a change in the absorption cross section for different isotopologues. For example, consider three OC^{33}S, OC^{34}S, and O^{13}CS, minor isotopologues of carbonyl sulfide with the main OC^{32}S isotopologue. The cross section for minor isotopologues can be expressed as ${}^{x}\sigma(E+\Delta ZPE) = {}^{32}\sigma(E)$, where E is the photon energy and ΔZPE is the zero point energy difference between major

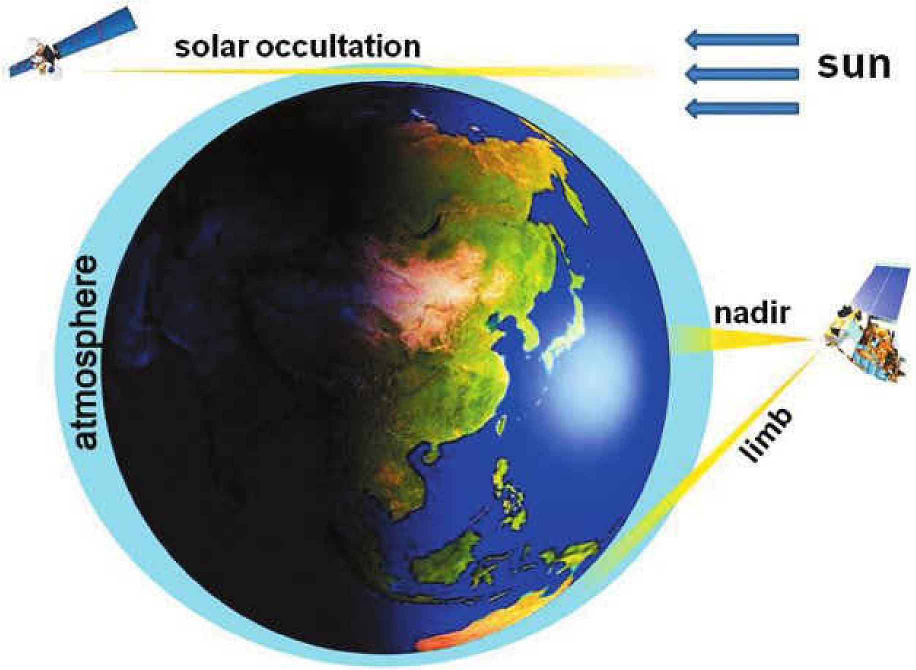

FIG. 11: Vertical (nadir) and horizontal (limb and solar occultation) satellite observation concept [11].

$OC^{32}S$ and a given isotopologue, and x represents each isotopologue (i.e. x = 32, 33, 34, or 36). This results in a change in the cross sections from the main isotopologue for each minor isotopologue (see Figure 10).

The molecular loss rate in the atmosphere by photolysis is given by [26]:

$$J_{p_x} = \int_{\lambda} \Phi(\lambda)\sigma_x(\lambda)F(\lambda)d\lambda. \tag{5}$$

where Φ is the photolysis quantum yield (assumed to be unity), σ is the absorption cross section for isotopologue x, and F is a photon flux respectively. From equation 5 one can infer that, different isotopologues have different photolysis rate.

2.4.3 Satellite observation

Satellite remote sensing provides a powerful method for global atmospheric measurements. It provides excellent spatial coverage that is not possible to achieve with the direct measurement methods. Satellite instruments can be classified according to their observation geometry into the limb-viewing or the nadir-viewing sounders.

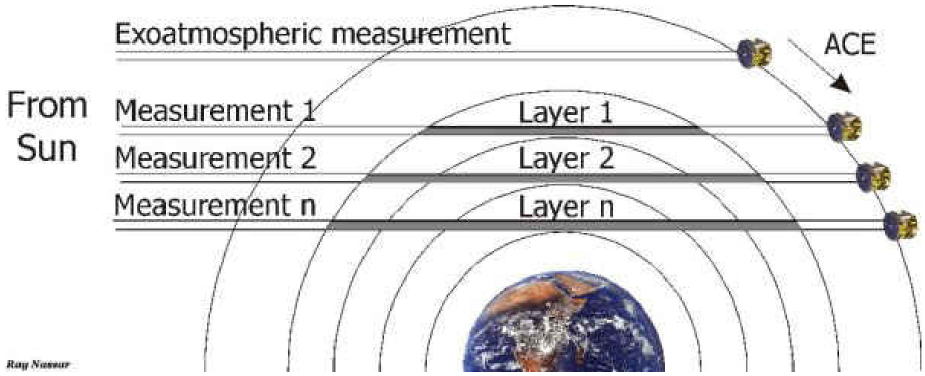

FIG. 12: Solar occultation geometry of ACE satellite [13].

Limb sounders observe the atmosphere tangentially, while nadir sounders have a downward observation geometry directed towards the Earth's surface. Figure 11 shows a schematic of these two types of satellites. Limb geometry is the natural choice for stratospheric measurements because the light is not masked by thick air below, leads to a long ray path which increases its sensitivity, and makes it suitable for measurement of atmospheric species with low concentrations.

In addition, the variation of observation angle allows vertical scanning of the atmosphere and increases vertical resolution of atmospheric measurements. Limb sounders are also classified by their measurement methods which are based on emission, scattering, solar occultation, and stellar occultation. In contrast to limb measurements, the altitude information of nadir observations is determined by pressure broadening of spectral lines and varying opacities, which gives a better horizontal resolution compared to the limb geometry. This allows a column density measurement of the atmosphere in the nadir geometry.

2.4.3.1 Solar occultation

Solar occultation is a technique in which the instrument records the radiance from the Sun, and attenuated along a horizontal ray-path through the atmosphere by absorption and scattering (see Figure 12). These measurements are carried out at a series of tangent altitudes, increasing in altitude during a sunrise or decreasing in altitude during a sunset. Then a slant column from multiple layers can be calculated. One can obtain profiles of the atmosphere from these slant columns.

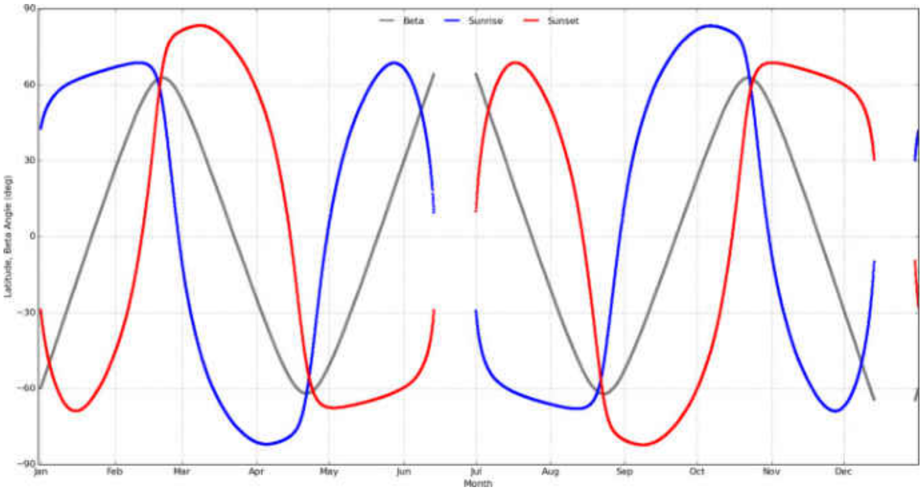

FIG. 13: ACE measurement latitude for sunrise and sunset and beta angle as a function of time of year [15].

2.4.3.2 ACE satellite

The ACE-FTS is a high resolution (0.02 cm^{-1}) infrared Fourier transform spectrometer on board the Canadian satellite SCISAT, known as the Atmospheric Chemistry Experiment (ACE) satellite [14, 15]. SCISAT was launched in 2003 and is still currently active. The satellite orbits around the Earth at a height of 650 km with 74° inclination angle to the equator. SCISAT makes measurements by solar occultation. The satellite period is 98 minutes which enables a measurement about every 49 minutes. About 30 measurement locations each day from two longitude circles (sunrise and sunset) and the latitude of those circles changes slowly with about 2 month required to cover the globe (see Figure 13). The pressure and temperature profiles as a function of altitude are determined from the ACE-FTS spectra by analyzing selected CO_2 lines using a fixed assumed volume mixing ratio (VMR) profile for CO_2 below 60 km, since CO_2 is well mixed and has a nearly constant VMR over much of middle atmosphere [16]. The temperature is determined from the relative intensity of the CO_2 lines and the pressure from the optical depth of the lines. The pressure is converted to altitude using a weather forecast model. The VMR retrieval of molecules and related isotopologues is done by using a set of microwindows, which are small portions of spectrum (typically less than 0.5 cm^{-1}) for the molecule of interest, which contains minimal interference from other molecules.

CHAPTER 3

SPECTROSCOPY BACKGROUND

3.1 Introduction

This chapter provides the principles of molecular spectroscopy and the Fourier transform measurement technique used to calculate vibrational-rotational linelists for AlF and AlCl diatomic molecules (Chapter 6), calculate a linelist for the electronic ($A^2\Pi - X^2\Sigma$) transition of the OH free radical (Chapter 7), and determine pressure induced broadening parameters for high temperature CH_4 (Chapter 8).

Spectroscopy is the field of science that provides possibilities for a deeper understanding of the fundamental properties of molecules, such as the molecular structure, the nature of the chemical bonds, molecular abundances, and so on, using the interaction between light and matter. To describe it simply, atoms and molecules absorb light and make a transition to an excited energy level. In some cases this results in a transition from an excited energy level to lower energy levels, which, results in emission spectra. Spectroscopy has many applications in physics, astronomy, atmospheric science, geoscience, medical science, information technology, and so on. For example, the importance of spectroscopy in the study of planets, stellar objects, and exoplanets has been growing as a result of the use of ground and space based telescopes for recording spectra of these objects.

3.2 Electronic, vibrational and rotational energy levels

3.2.1 Schrödinger equation

The energy levels of a molecule can be calculated from the Schrödinger equation

$$\hat{H}\psi = E\psi. \tag{6}$$

where $\hat{H}$ is the total Hamiltonian operator [18]

$$\begin{aligned}\hat{H} = -\frac{\hbar^2}{2}\sum_{i=1}^{n_e}\nabla_i^2 - \frac{\hbar^2}{2}\sum_{I=1}^{n_N}\frac{1}{M_I}\nabla_I^2 - \sum_{i=1}^{n_e}\sum_{I=1}^{n_N}\frac{z_I e^2}{4\pi\epsilon_0 r_{iI}} \\ + \sum_{i=1}^{n_e}\sum_{j\geq i}^{n_e}\frac{e^2}{4\pi\epsilon_0 r_{ij}} + \sum_{I=1}^{n_N}\sum_{J\geq I}^{n_N}\frac{z_I z_J e^2}{4\pi\epsilon_0 R_{IJ}} \\ = \hat{T} + \hat{T}_N + \hat{V}_{eN} + \hat{V}_{ee} + \hat{V}_{NN},\end{aligned} \tag{7}$$

where n_e is the number of electrons, n_N is the number of nuclei, i and j represent the indices of the electrons, I and J represent the indices of the nuclei, z_I and M_I are the charges and mass of nucleus I, respectively, and r_{ij} is the distance between particles i and j. The various operators in equation 7 are: 1. the electronic kinetic energy ($\hat{T}$), 2. the nuclear-nuclear kinetic energy ($\hat{T}_N$), 3. the electron-nuclear attraction potential ($\hat{V}_{eN}$), 4. the electron-electron repulsion potential ($\hat{V}_{ee}$), 5. nuclear-nuclear repulsion potential ($\hat{V}_{NN}$).

The solution to the Schrödinger equation is not easy, so further simplifications are required. One approximation is the Born-Oppenheimer approximation. Electrons move much faster than nuclei under the electrostatic forces, therefore, nuclei motion ($\hat{T}_N$) is negligible and nuclear repulsion ($\hat{V}_{NN}$) can be taken as a constant. Under this approximation, electronic motion is separated from nuclear motion, and the solution for the electronic part of the wavefunction can be solved. Note that, in this study, we consider the Schrödinger equation for diatomic molecules, which reduces the nuclear coordinates to a single molecular coordinate of $\mathbf{R}$. The separation of electronic and nuclear motion (vibrational-rotational) parts allows the approximation of ψ as the product of

$$\psi \approx \psi_{el}(r_i;\mathbf{R})\chi_{\mathbf{N}}(\mathbf{R}) \tag{8}$$

where $\chi_N(\mathbf{R})$ only depends on the nuclear coordinate $\mathbf{R}$, while ψ_{el} depends upon the electronic coordinates (r_i) with parametric dependence on the nuclear coordinate $(\mathbf{R})$. This separates the Schrödinger equation into two equations

$$(\hat{H} + \hat{V}_{NN})\psi_{el}(r_i;\mathbf{R}) = \mathbf{U}(\mathbf{R})\psi_{\mathbf{el}}(\mathbf{r_i};\mathbf{R}) \tag{9}$$

and

$$(\hat{T}_N + U(\mathbf{R}))\chi_{\mathbf{N}}(\mathbf{R}) = \mathbf{E_N}\chi_{\mathbf{N}}(\mathbf{R}), \tag{10}$$

Equation 9 represents the electronic state, which has the largest share of molecular energy, and can be solved using *ab inito* methods. Equation 10 accounts for the nuclear motion (vibrational and rotational) that will be the subject of next sections.

3.3 Rotational spectroscopy

A diatomic molecule's rotation contributes less than the vibrational and electronic parts to the molecular energy. The rotation of a diatomic molecule resembles the rotation of a rigid body. The classical kinetic energy for a rotating linear molecule is

$$\begin{aligned} E_k &= \frac{1}{2}I_x\omega_x^2 + \frac{1}{2}I_y\omega_y^2 \\ &= \frac{J_x^2}{2I} + \frac{J_y^2}{2I} = \frac{J^2}{2I} \end{aligned} \tag{11}$$

since $I_x = I_y$ for a linear molecule and J represents the total angular momentum. For a rigid rotor, a rotational Hamiltonian can be defined as

$$\hat{H} = \frac{\hat{J}^2}{2I} \qquad \text{for } J = 0, 1, 2... \tag{12}$$

The corresponding quantum mechanical Hamiltonian operator is $-\frac{\hbar^2\nabla^2}{2I} = \frac{\hat{J}^2}{2I}$. Since ψ is now one of the spherical harmonics [18], $\psi_{JM} = Y_{JM}$, the specific Schrödinger equation can be solved

$$\frac{\hat{J}^2\psi}{2I} = \frac{J(J+1)\hbar^2\psi}{2I} = BJ(J+1)\psi, \tag{13}$$

where J is the rotational quantum number, B is the molecular rotational constant equal to $\hbar/2I$, and $F(J) = BJ(J+1)$ is the rotational eigenvalue.

The rotational transitions are governed by the transition dipole moment. This means only molecules with permanent dipole moment can have allowed transitions.

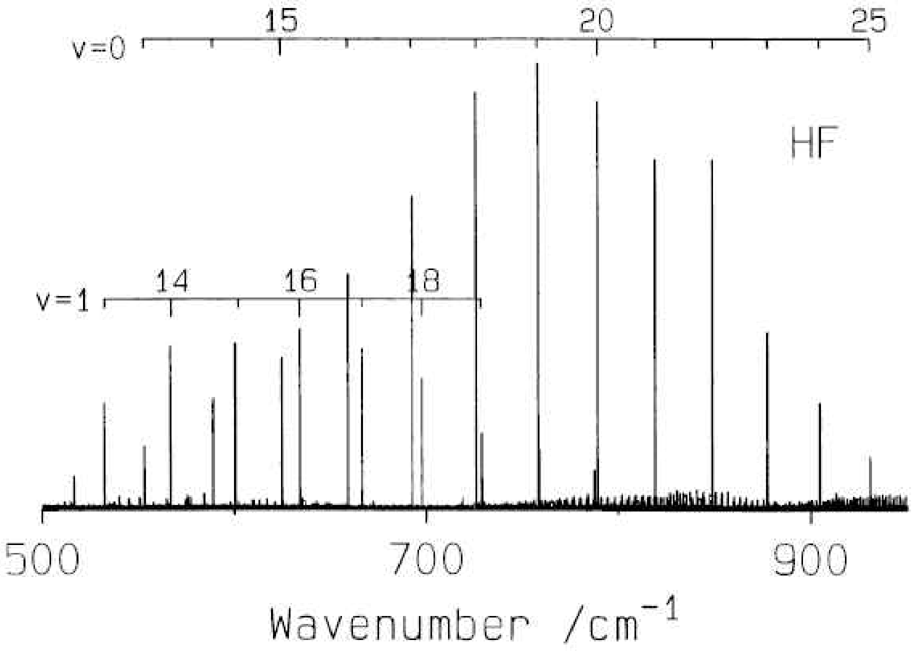

FIG. 14: Pure rotational emission of hot HF molecules [18].

$$\mathbf{M} = \int \psi_{J'M'} \boldsymbol{\mu} \psi_{JM} d\tau \tag{14}$$

These transitions for a linear molecule result in frequencies

$$\begin{aligned} \nu_{J+1 \leftarrow J} &= F(J') - F(J'') \\ &= B(J+1)(J+2) - BJ(J+1) \\ &= 2B(J+1). \end{aligned} \tag{15}$$

Equation 15 shows that all the transitions are separated by $2B$, as illustrated in Figure 14, for the example of HF rotational transitions.

In reality, molecules are not rigid rotors. As a molecule rotates, atoms undergo a centrifugal force that can be accounted for in the energy eigenvalue $F(J)$

$$F(J) = BJ(J+1) - D(J(J+1))^2 + H(J(J+1))^3 + L(J(J+1))^4 + ..., \tag{16}$$

where D is the centrifugal distortion constant and H and L are additional higher order distortion constants.

3.4 Vibrational spectroscopy

The vibrational kinetic energy has a greater effect on the total molecular energy than the rotational part but a smaller effect than the electronic part. The vibrations in a diatomic molecule can be explained by a simple harmonic motion of nuclei about an equilibrium point (r_e). The Schrödinger equation for such a quantum mechanical harmonic oscillator can be written as

$$\frac{-\hbar^2}{2\mu}\frac{d}{dr}r^2\frac{dR}{dr}+(\frac{\hbar^2 J(J+1)}{2\mu r^2}+V(r))R=ER \tag{17}$$

where μ is the reduced mass and R is the radial part of wavefunction $\psi = R(r)Y_{JM}(\theta,\phi)$. If we define

$$\frac{\hbar^2 J(J+1)}{2\mu r^2}=V_{cent} \tag{18}$$

as the centrifugal potential, a particular form of V(r) is required to obtain the vibrational energy levels. One potential form is known as Dunham potential, which can be obtained from the Taylor expansion of $V(r)$ about r_e,

$$V(r)=V(r_e)+\left.\frac{dV}{dr}\right|_{r_e}(r-r_e)+\frac{1}{2}\left.\frac{d^2V}{dr^2}\right|_{r_e}+... \tag{19}$$

Setting $V(r_e)$ and the first derivative to zero at equilibrium distance r_e and keeping only the first term gives

$$V(r)=\frac{1}{2}\left.\frac{d^2V}{dr^2}\right|_{r_e}(r-r_e)^2=\frac{1}{2}k(r-r_e)^2 \tag{20}$$

An example of $V(r)$, including the associated wave function, is shown in Figure 15 with vibrational energy

$$E_v=\hbar\omega(v+\frac{1}{2}) \tag{21}$$

where $\omega=(k/\mu)^{1/2}$ and $v=0,1,2,...$

The harmonic oscillator is only a good approximation for the lower vibrational energy levels of diatomic molecules. At higher energies, the internuclear bonds become weaker and closer to the dissociation limit, as shown in Figure 16. Another proposed potential for diatomic molecules is the Morse potential

$$V(r)=D(1-e^{-\beta(r-r_e)})^2, \tag{22}$$

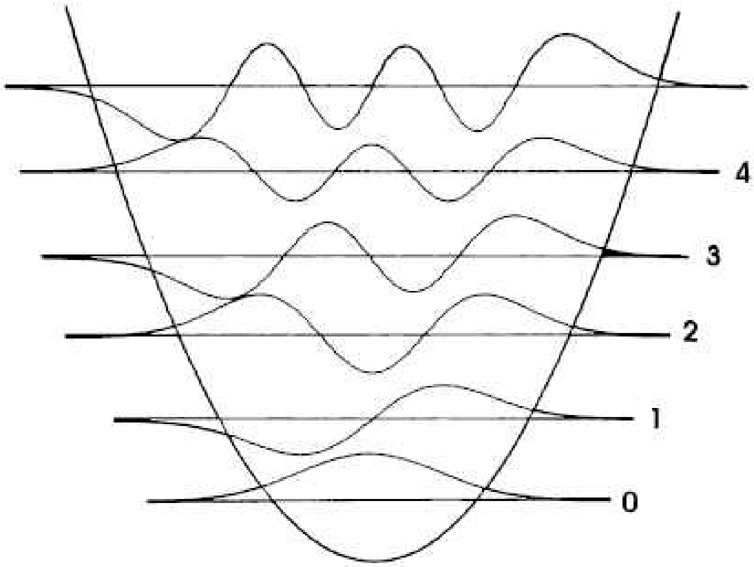

FIG. 15: Potential energy curve within the harmonic oscillator approximation. Also shown are the first five energy levels and wavefunctions [18].

which accounts for the anharmonicity of diatomic molecular potential and approaches the dissociation limit $V(r) = D$ as $r \to \infty$.

A more general analytical form of a real potential energy is known as Dunham potential

$$V(r) = a_0\xi^2(1 + a_1\xi + a_2\xi^2 + ...), \tag{23}$$

where

$$\xi = (\frac{r - r_e}{r_e}). \tag{24}$$

Dunham obtained an approximate analytical solution for the vibrational-rotational energy levels of a diatomic molecule by employing a semi-classical quantization condition from WKB (Wentzel–Kramers–Brillouin) theory, resulting

$$(\frac{2\mu}{\hbar^2})^{1/2}\int_{r_-}^{r_+}\sqrt{(E - V(r))}dr = (v + \frac{1}{2})\pi, \tag{25}$$

in which r_+, r_- are the inner and outer turning points of $V(r)$ at energy E. The vibrational-rotational energy levels derived from equation 25 can be expressed as

$$E_{vJ} = \sum_{jk} Y_{jk}(v + \frac{1}{2})^j (J(J+1))^k. \tag{26}$$

Using the Dunham potential, the customary vibrational energy levels

$$G(v)=\omega_\mathrm{e}(v+\frac{1}{2})-\omega_\mathrm{e}x_\mathrm{e}(v+\frac{1}{2})^2+\omega_\mathrm{e}y_\mathrm{e}(v+\frac{1}{2})^3+\omega_\mathrm{e}z_\mathrm{e}(v+\frac{1}{2})^4... \tag{27}$$

and rotational energy levels

$$F(J)=B_vJ(J+1)-D_v(J(J+1))^2+H(J(J+1))^3+... \tag{28}$$

can be derived, where

$$B_v=B_\mathrm{e}-\alpha_\mathrm{e}(v+\frac{1}{2})+\gamma_\mathrm{e}(v+\frac{1}{2})^2+... \tag{29}$$

$$D_v=D_\mathrm{e}-\beta_\mathrm{e}(v+\frac{1}{2})+... \tag{30}$$

B_v, D_v, H, ω_e, $\omega_e x_e$, $\omega_e y_e$, $\omega_e z_e$, B_e, α_e, γ_e, D_e, and β_e are the conventional spectroscopic constants. A diagram of elecronic, vibrational, and rotational energy levels for a diatomic molecule is shown Figure 17. The electronic energy state has the largest energy contribution, the vibrational energy levels have more contribution than rotational energy levels and less contribution compared to electronic energy level, as shown in Figure 17.

3.5 Electronic spectroscopy

Within the Born-Oppemheimer approximation, in which the motion of nuclei is negligible, the electronic Schrödinger equation for a diatomic molecule A—B is

$$\hat{H}\psi_{el}=E_{el}\psi_{el} \tag{31}$$

for which the Hamiltonian given by equation 12 and written for AB molecule is

$$\hat{H}_{el}=-\frac{\hbar^2}{2m_e}\sum_i\nabla_i^2-\sum_i\frac{z_Ae^2}{4\pi\epsilon_0r_{iA}}-\sum_{i=1}\frac{z_Be^2}{4\pi\epsilon_0r_{iB}}+\sum_i\sum_{j\geq i}\frac{z_Az_Be^2}{4\pi\epsilon_0r_{ij}} \tag{32}$$

Equation 31 can be solved by considering that ψ_{el} is made up of molecular orbitals ϕ_i in a Slater determinant

$$\psi_{el}=\left|\phi_1(1)\bar{\phi}_1(2)\phi_2(3)\ ..\right|, \tag{33}$$

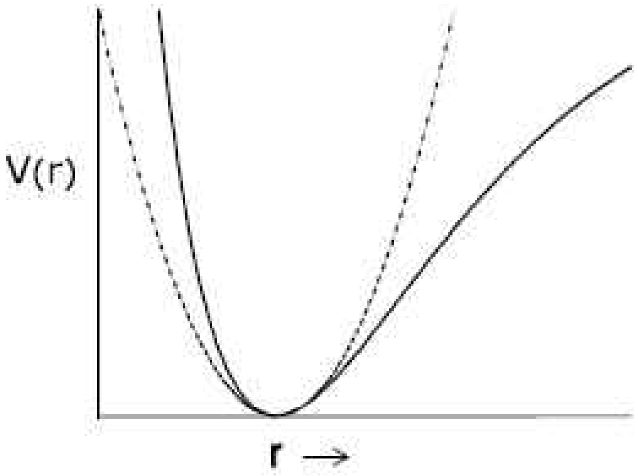

FIG. 16: Comparison of harmonic (dots) and anharmonic potential (solid) [18].

where ϕ_i is made up atomic orbitals

$$\phi_i = \sum_j (C_{iA_j}\phi_j^A + C_{iB_j}\phi_j^B), \tag{34}$$

in which ϕ_j^A and ϕ_j^B are the atomic orbitals of atoms A and B, respectively.

3.5.1 Electronic and nuclear rotational angular momentum in diatomic molecules

For a diatomic molecule, the total angular momentum, neglecting nuclear spin, is the sum of orbital ($\hat{\mathbf{L}}$), with projection of Λ on the z axis, spin ($\hat{\mathbf{S}}$), with projection of Σ on the z axis, and nuclear rotation ($\hat{\mathbf{R}}$) angular momenta (Figure 18).

$$\hat{\boldsymbol{J}} = \hat{\boldsymbol{L}} + \hat{\boldsymbol{S}} + \hat{\boldsymbol{R}} \tag{35}$$

Table 2 presents a summary of the angular momentum operators along the molecular axis, with the corresponding eigenvalues. Note that L is not a good quantum number for a diatomic molecule. The total angular momentum $\hat{J}$ has a projection of $\Omega\hbar$ along the molecular axis and a projection of $M_J\hbar$ on the space fixed z-axis (Figure 19). Knowing the angular momentum quantum numbers, the ${}^{2S+1}L_J$ notation is used for atomic orbital representation and the ${}^{2S+1}\Lambda_\Omega$ notation is the orbital representation of the diatomic molecules with $2S+1$ spin component, where $\Lambda = \sum \lambda_i$ and

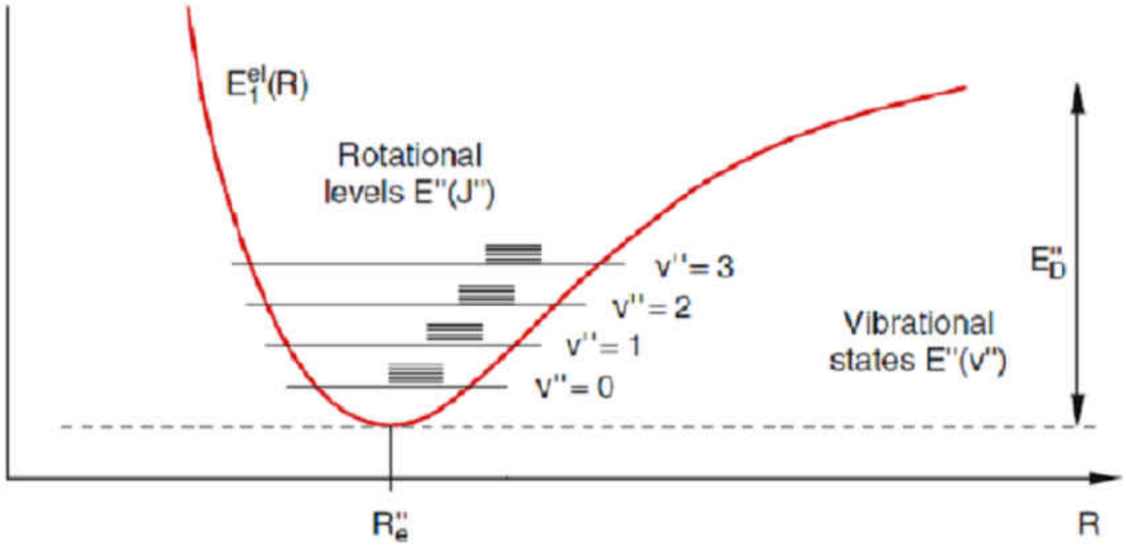

FIG. 17: A demonstration of the electronic, vibrational, and rotational levels of a diatomic molecule [17].

$\Omega = |\Lambda| + \Sigma$. The Λ value can take $0, 1, 2, ...$ values that are represented by Greek letters $\Sigma, \Pi, \Delta, ...$, in the orbital notation. For example, the orbital representations in a diatomic molecule with $S = 1/2$ and $\Lambda = 1$, that has two $\Sigma = 3/2, 1/2$ spin components, are $^2\Pi_{3/2}$ and $^2\Pi_{1/2}$. Also, the electronic states of a diatomic molecule are represented with the upper case letters X for the ground state and $A, B, C, ...$ for the excited states with the same $(2S + 1)$ spin multiplicity and with the lower case letters $a, b, c, ...$ for a different spin multiplicity.

TABLE 2: Angular momentum operators for a diatomic molecule along molecular axis and their eigenvalues.

Operator	Eigenvalue	Equation
$\hat{J}^2$	$J(J+1)\hbar^2$	$\hat{J}^2\psi = J(J+1)\hbar^2\psi$
$\hat{J}_z$	$\Omega\hbar$	$\hat{J}_z\psi = \Omega\hbar\psi$
$\hat{L}_z$	$\Lambda\hbar$	$\hat{L}_z\psi = \Lambda\hbar\psi$
$\hat{S}^2$	$S(S+1)\hbar^2$	$\hat{S}^2\psi = S(S+1)\hbar^2\psi$
$\hat{S}_z$	$\Sigma\hbar$	$\hat{S}_z\psi = \Sigma\hbar\psi$

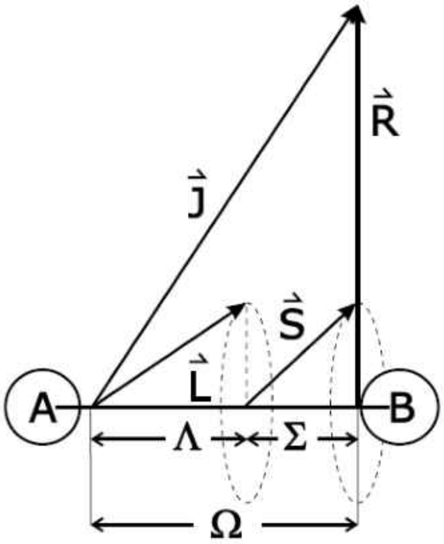

FIG. 18: Angular momenta in a diatomic molecule [18]

3.5.2 Parity

If the molecule has a certain symmetry, then it is useful to label the molecular energy and the wave function using parity operators. The symmetry considerations become important because there are certain selection rules based on parity that determine the possible transitions among the energy levels of a molecule. Here we only mention total $(+/-)$ and rotationless (e/f) parities, as the other types of parities are outside of scope of this study.

3.5.2.1 Total parity

We can label the energy states of a diatomic molecule based on their parity. Parity is the inversion of a diatomic molecule's coordinates in the laboratory frame, and it is presented by operator E^*

$$\hat{E}^*\psi(X_i, Y_i, Z_i) = \psi(-X_i, -Y_i, -Z_i) = \pm\psi(X_i, Y_i, Z_i). \tag{36}$$

3.5.2.2 Rotationless parity (e/f)

The effect of parity on the rotational part of the wavefunction results in

$$\hat{E}^* Y_{JM} = (-1)^J Y_{JM}, \tag{37}$$

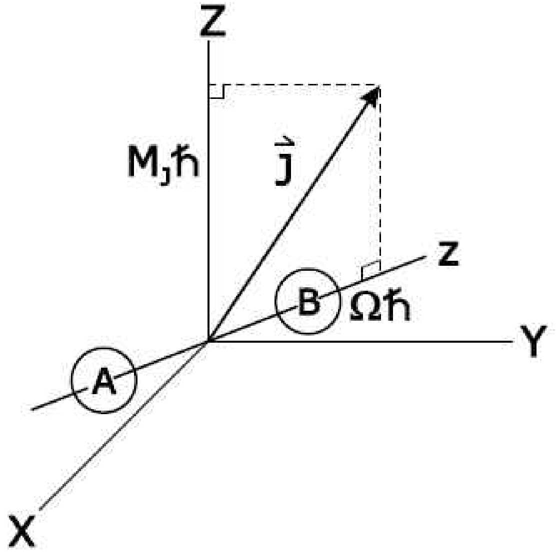

FIG. 19: Projection of total angular momentum on the laboratory and molecular coordinates [18]

where, the total parity changes sign with J because of $(-1)^J$ phase factor. To factor out this, rotationless parities e and f are defined as

$$\hat{E}^*\psi = +(-1)^J\psi, \quad \text{for } e, \tag{38}$$

and

$$\hat{E}^*\psi = -(-1)^J\psi, \quad \text{for } f. \tag{39}$$

3.5.2.3 Selection rules

For a diatomic molecule, the electronic, vibrational, and rotational transitions are restricted by whether or not the transition dipole moment, presented in equation 14, exists for the two specific states between which the transition occurs. This restriction is described by a set of *selection rules*, that result from equation 14. These selection rules, presented below, dictate which transitions are allowed and which are forbidden.

Rotational:

1) The molecule must have a permanent dipole moment.

2) $\Delta J = J' - J'' = \pm 1$,

where J' and J'' are upper and lower state rotational quantum numbers, respectively.

Vibrational:

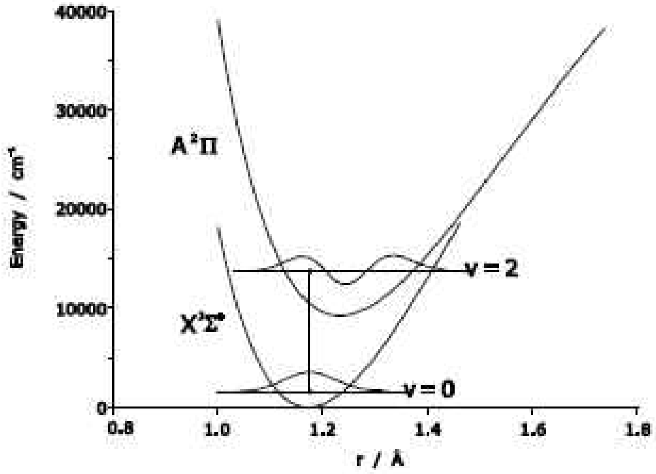

FIG. 20: v=0–2, $A^2\Pi - X^2\Sigma$ transition of CN [18]

1) The first derivative of the dipole moment as a function of nuclear motion must be non-zero.
2) $\Delta v = \pm 1, [\pm 2, ...]$.

Electronic:
The possible rotational, vibrational, and electronic transitions among energy levels, between the electronic states of a diatomic molecule, are determined by the selection rules:
1. $\Delta\Lambda = 0, \pm 1$. Then transitions such as $\Sigma - \Sigma$, $\Pi - \Pi$, $\Pi - \Sigma$, and so on, are allowed.
2. $\Delta S = 0$, with the exception of heavy atoms that undergo spin-orbit coupling in which $\Delta S \neq 0$ transitions become stronger.
3. $\Delta\Sigma = 0$.
4. $\Delta\Omega = 0, \pm 1$.
5. $\Sigma^+ - \Sigma^+$ and $\Sigma^- - \Sigma^-$ are allowed but not $\Sigma^+ - \Sigma^-$.
6. For total parity $+ \leftrightarrow -$, but $+ \not\leftrightarrow +$, $- \not\leftrightarrow -$.

One example of the electronic states of a heternuclear diatomic molecule (CN) with corresponding potential for the ground state and excited state is shown in Figure 20.

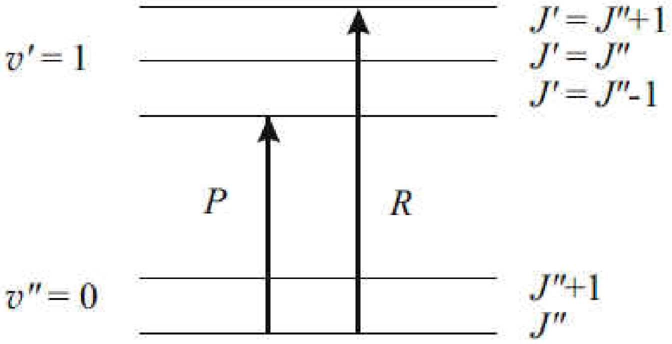

FIG. 21: Energy level diagram of a diatomic molecule, representing P and R absorption transitions from a ground vibrational state [20]

3.6 Spectral branches for diatomic molecules

According to the rotational selection rule, the rotational quantum number can either increase or decrease by one. As a result, two spectral branches emerge (Figure 21). The R branch is associated with an increase in rotational quantum number ($J'' > J'$) and the P branch is associated with a decrease in rotational quantum number ($J'' < J'$).

3.7 Fourier transform spectroscopy

Fourier Transform Spectrometers (FTSs) are the typical choice in the infrared region. For example, the FTS has become a very useful tool in molecular structure analysis, since the vibrational modes of polar bonds (e.g. C–H bond vibrations) of molecules are in the infrared region. FTSs also are common instruments used for the atmospheric molecular component studies on board satellites, aircraft or balloons. The main part of an FTS instrument is a Michelson interferometer, shown in Figure 22. In a Michelson interferometer, light from a source is collimated and divided by a beam splitter into two beams. These beams are reflected back from two mirrors, one a fixed mirror and another a moving mirror. The reflected beams recombine at the beam splitter and are collected by a detector. If the moving mirror has a $\delta/2$ path difference with the fixed mirror, an optical path difference of δ is introduced. For a

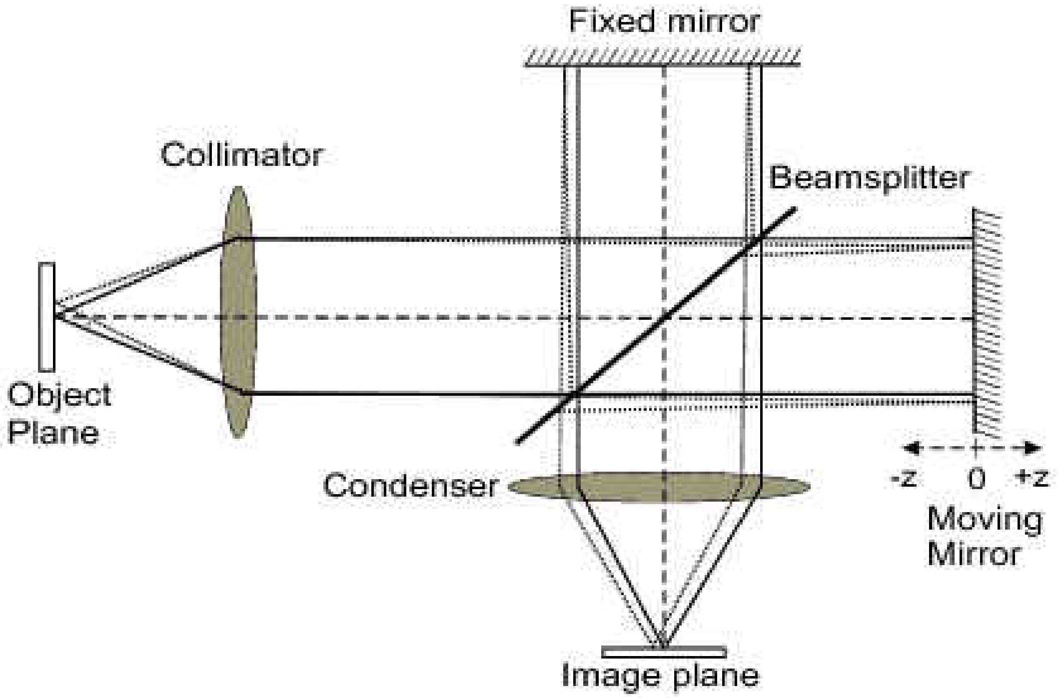

FIG. 22: Schematic of Michelson interferometer [21]

monochromatic wave the beam intensity at the detector is

$$I(\delta) = I_0 cos^2(\phi/2). \tag{40}$$

with

$$\phi = \frac{\delta}{\lambda}2\pi = \frac{\delta}{c}\nu. \tag{41}$$

If the light source emits a spectrum $B(\nu)$ we obtain

$$\begin{aligned} I(\delta) &= \int_0^\infty B(\nu)cos^2(\frac{\delta}{c}\pi\nu)d\nu \\ &= \frac{1}{2}\int_0^\infty B(\nu)[1+cos(\frac{\delta}{c}2\pi\nu)]d\nu \end{aligned} \tag{42}$$

part of above equation that depends on δ is named interferogram

$$J(\delta) = \frac{1}{2}\int_0^\infty B(\nu)cos(\frac{\delta}{c}2\pi\nu)d\nu. \tag{43}$$

The spectrum $B(\nu)$ can be calculated from the interferogram $J(\delta)$ using the Fourier

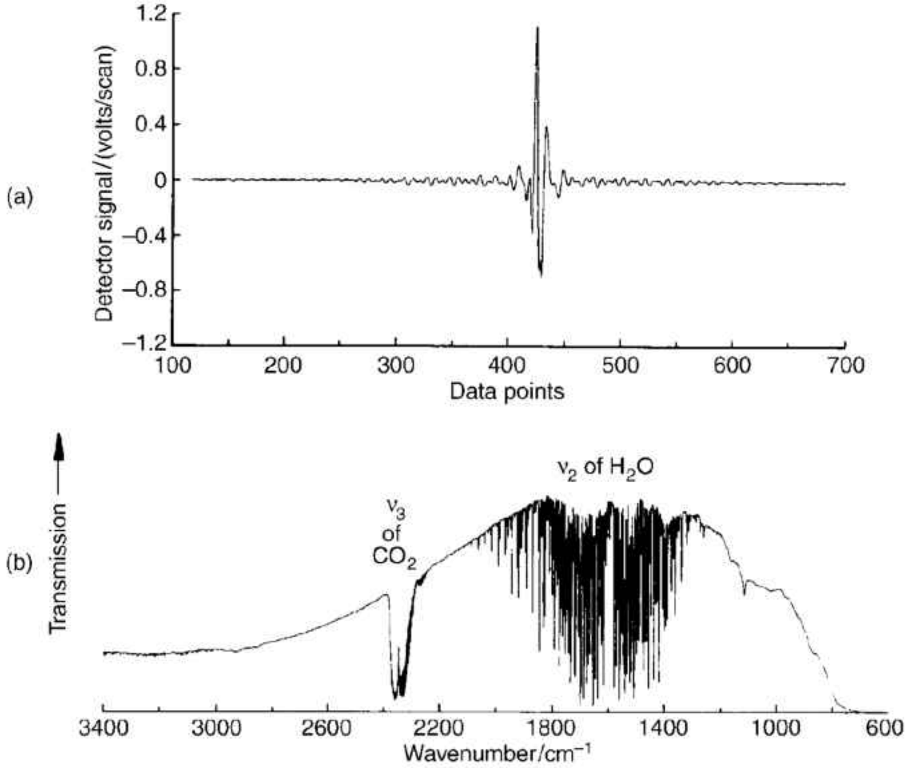

FIG. 23: (a) Infrared interferogram of the absorption spectrum of air in the 400–3400 cm^{-1} region (b) the Fourier transformed spectrum [22]

transformation. Figure 23 shows an example of interferogram and its Fourier transformed absorption spectrum of air in the 400-3400 cm^{-1}.

$$B(\nu) \propto \int_0^\infty J(\delta) cos(\frac{\delta}{c} 2\pi\nu) d\delta \tag{44}$$

3.8 Line broadening mechanisms

Broadening of an absorption feature is due to physical processes that occur within the medium that perturbs the energy levels or the way in which individual molecules interact with light. There are several broadening processes. A few of them will be mentioned in this chapter within the scope of this study.

3.8.1 Natural broadening

According to the Heisenberg uncertainty, in the absence of interaction with other atoms, there is a uncertainty in the energy levels in a transition due to the lifetime of atom in that energy level,

$$\Delta E_i \geq \frac{\hbar}{\tau_i}. \tag{45}$$

This leads to the natural lifetime broadening

$$\begin{aligned}\Delta\nu &= \frac{1}{2\pi}(\frac{1}{\tau_i} + \frac{1}{\tau_j}) \\ &= \frac{1}{2\pi}(\sum_k A_{ik} + \sum_k A_{jk}),\end{aligned} \tag{46}$$

where τ_i and τ_j are the lifetimes of E_i and E_j energy levels, and A_{ik} and A_{jk} are the Einstein coefficients for all the transitions from the energy levels.

3.8.2 Collisional line broadening

In a medium, molecules interact with each other via collisions that changes the energy state of molecules through energy transfer. As a result of collision, the average lifetime of a molecule in a state, can be reduced. According to the equation 46, reducing lifetime τ, results in a greater uncertainty in frequency and increased broadening of absorption lineshape. The collisional broadening is a hmogenous process which has a Lorentzian lineshape profile

$$g(\nu - \nu_0) = \frac{\Delta\nu_{1/2}/(2\pi)}{(\Delta\nu_{1/2}/2)^2 + (\nu - \nu_0)^2} \tag{47}$$

where $\Delta\nu_{1/2}$ is the full width at half maximum.

3.8.2.1 Doppler broadening

If a molecule has a velocity component in the same direction of light propagation, there will be a shift in the frequency which is called Doppler shift. The velocity distribution of gas molecules that move in random directions is described by a Maxwell-Boltzmann distribution function. The Maxwellian function describes the portion of molecules with the same velocity component (in the same velocity class) that have a same Doppler shift. Therefore, the distribution function results an inhomogeneous (varies with frequency) lineshape function that has a Gaussian form

$$g_D(\nu - \nu_0) = \frac{2}{\Delta\nu_D}(\frac{ln2}{\pi})^{1/2}exp(-4ln2(\frac{\nu - \nu_0}{\Delta\nu_D})^2), \tag{48}$$

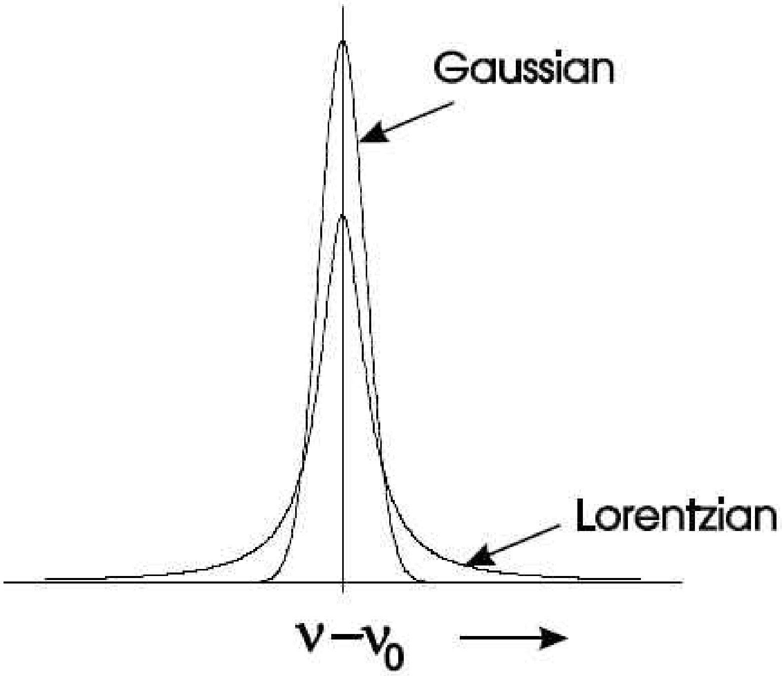

FIG. 24: Gaussian and Lorentzian lineshape functions [18]

where $\Delta\nu_D$ is the Doppler FWHM

$$\Delta\nu_D = \nu_0(\frac{8kTln2}{mc^2})^{1/2}, \tag{49}$$

or

$$\Delta\tilde{\nu}_D = 7.2\times10^{-7}\tilde{\nu}_0\sqrt{\frac{T}{M}} \tag{50}$$

where T is in K, M in atomic mass units u, $\tilde{\nu}_0$ and $\Delta\tilde{\nu}_D$ have the same frequency units (e.g., cm^{-1}). Figure 24 shows a comparison of a typical Gaussian and Lorentzian lineshapes. A Gaussian lineshape has a sharper peak while a Lorentzian lineshape has a wider tail.

3.8.2.2 Voigt lineshape

In cases where both Doppler and collisional broadening are significant, the appropriate lineshape will be a combination of both lineshapes. A Voigt lineshape is a convolution of Gaussian and Lorentzian lineshapes

$$g_V(\nu-\nu_0) = \int_{-\infty}^{+\infty} g_L(\nu-\nu_0-\nu')g_D(\nu')d\nu'. \tag{51}$$

If we define (1) Voigt "a" parameter

$$a = \frac{\sqrt{ln2}\Delta\nu_L}{\Delta\nu_D} \tag{52}$$

(2) nondimentional line position, w

$$w = \frac{2\sqrt{ln2}(\nu - \nu_0)}{\Delta\nu_D} \tag{53}$$

Doppler value at the line center ν_0,

$$g_D(\nu_0) = \frac{2}{\Delta\nu_D} \tag{54}$$

(4) and a dimensionless variable, y

$$y = \frac{2\sqrt{ln(2)}(\nu - \nu_0 + \delta)}{\Delta\nu_D} \tag{55}$$

where δ is the pressure shift of line center ν_0, equation 51 becomes

$$\begin{aligned} g_V(\nu - \nu_0) &= g_D(\nu_0)\frac{a}{\pi}\int_{-\infty}^{+\infty}\frac{exp(-y^2)dy}{a^2 + (w-y)^2} \\ &= g_D(\nu_0)V(a,w) \end{aligned} \tag{56}$$

where $V(a, w)$ is called the "Voigt function". The a parameter, shows the relative significance of collisional to Doppler broadening, which increases with the increase of collisional broadening, and the w parameter is a measure of the distance form line center ν_0. There is no analytical solution for the calculation of the Voigt lineshape; however, a large number of numerical methods have been developed for the evaluation of the Voigt lineshape.

CHAPTER 4

A NEAR GLOBAL ATMOSPHERIC DISTRIBUTION OF N_2O ISOTOPOLOGUES

The majority of results used in this chapter are published in Geophysical Research Letters ([58]). This study was supervised by Peter F.Bernath (co-author). As the second author of this paper, I was responsible for the ACE data analysis, the preparation of figures, and the supplementary data, all of which come from ACE satellite data.

4.1 Introduction

Nitrous oxide (N_2O) is a significant greenhouse gas that has two major impacts on the Earth's atmosphere. First, it is an inert potent gas in the troposphere; N_2O is the third strongest greenhouse gas after CO_2 and CH_4, and has a global warming potential (GWP) of 265 over 100 years [23]. Second, it is a reactive ozone destroying substance in the stratosphere and has been the dominant ozone depleting substance, due to the reduction of CFCs which are limited by the Montreal Protocol. N_2O has several sources in the troposphere. It is one of the several nitrogen species produced in the biological nitrification/denitrification process on land and in the ocean, which is still the main source of N_2O. In addition, anthropogenic sources of N_2O include agriculture, the use of nitrogen fertilizer, bio-fuel burning, sewage treatment, manufacturing, and other industrial processes [24]. These sources have significantly increased, leading to increased denitrification in the soil. Runoff and leaching also transport nitrogen compounds into waterways, leading to an increased denitrification in aquatic environments. Overall, anthropogenic activities lead to the

20% increase in the tropospheric Volume Mixing Ratio (VMR) from the pre-indestrial value of 270 ppb to the 2011 value of, 324 ppb [24].

N_2O is an inert gas in the troposphere with a life time of 120 years [25]. The main sinks of N_2O in the stratosphere are photolysis and reaction with singlet oxygen:

$$\mathrm{N_2O + h\nu \longrightarrow N_2 + O\,(^1D)} \tag{57}$$

$$\mathrm{N_2O + O\,(^1D) \longrightarrow N_2 + O_2} \tag{58}$$

$$\mathrm{N_2O + O\,(^1D) \longrightarrow 2\,NO} \tag{59}$$

where photolysis makes up 90% of N_2O loss in the atmosphere, chemical loss via reaction with singlet oxygen accounts for 10% of N_2O sink in the atmosphere. The main source of $O(^1D)$ in the upper atmosphere is the photolysis of ozone, and reaction 59 is responsible for NO_x production and ozone destruction in the stratosphere [26]. It has been suggested that reaction 57 is primarily responsible for the observed isotopic fractionation [27] and modern ab *initio* calculations of this fractionation [28] generally agree with laboratory and atmospheric observations.

Recently, there has been a discovery of another N_2O source in the upper atmosphere. Several reactions have been proposed as potential atmospheric sources of N_2O. The satellite based observations of the Atmospheric Chemistry Experiment-Fourier transform spectrometer (ACE-FTS) show an enhanced concentration of N_2O during winter over the polar region between 2004 and 2006 at 50-60 km. This event is associated with the transport of high levels of NO_x in the polar night region from the upper mesosphere and lower thermosphere, following sudden warming events in the middle of January [29].

Also, the more recent ACE-FTS observations show that N_2O is continuously produced via energetic particle precipitation in the lower thermosphere, where enhanced N_2O is present at all latitudes, during all seasons. The results are consistent with an N_2O production source peaking near or above 94 km via low-energy particles, as well as a polar wintertime source near 70 km via medium energy particles [30].

$$\mathrm{N_2\,(A^3\Sigma_u^+) + O_2 \longrightarrow N_2O + O} \tag{60}$$

$$\mathrm{N} + \mathrm{O_2} \longrightarrow \mathrm{N_2O} \tag{61}$$

$$\mathrm{N\,(^4S)} + \mathrm{NO_2} \longrightarrow \mathrm{N_2O} + \mathrm{NO} \tag{62}$$

$$\mathrm{O_3^*} + \mathrm{N_2} \longrightarrow \mathrm{N_2O} + \mathrm{O_2\,(b^1\Sigma_{\mathit{g}}, X^3\Sigma_{\mathit{g}}^-)} \tag{63}$$

N_2O has several isotopically-substituted (isotopologue) combinations, the most important of which are $NN^{18}O$, ^{15}NNO, and $N^{15}NO$, with the natural abundances of about 0.20%, 0.36%, 0.36%, respectively, with a parent $^{14}N^{14}N^{16}O$ abundance of 99%. Stable isotopic ratios of N_2O are linked to the sources and sinks with specific isotopic signatures, which can provide additional constraints on emissions and stratospheric sinks.

Isotopic abundances are defined by isotopic enrichment. Isotopologue enrichment is described by the delta notation, expressed in per mill (‰).

$$\delta^{15}N^i = (\frac{^{15}R^i_{sample}}{^{15}R^i_{std}} - 1) \times 1000, \qquad ^{15}R^1 = \frac{[^{15}N^{14}N^{16}O]}{[^{14}N^{14}N^{16}O]} \qquad ^{15}R^2 = \frac{[^{14}N^{15}N^{16}O]}{[^{14}N^{14}N^{16}O]} \tag{64}$$

$$\delta^{15}O = (\frac{^{18}R_{sample}}{^{18}R_{std}} - 1) \times 1000, \qquad ^{18}R = \frac{[^{14}N^{14}N^{18}O]}{[^{14}N^{14}N^{16}O]} \tag{65}$$

in which $^{15}\mathrm{R}ref$ = 0.00367666 and, $^{18}\mathrm{R}ref$=0.002005 are, respectively, the reference isotope ratio of air-N_2 for nitrogen and the Vienna Standard Mean Ocean Water (VSMOW) for oxygen isotope measurements; $^{15}N^1$ refers to ^{15}NNO, $^{18}N^2$ refers to $N^{15}NO$ and ^{18}O refers to $NN^{18}O$.

Isotopic abundances can be measured by isotope mass spectrometery [31] or infrared absorption spectroscopy [32, 33]. There is a large variability in $\delta^{15}N$ and $\delta^{18}O$ from a given source that can be attributed to the complexity of nitrogen fixing, nitrification, and denitrification which have multiple steps. Enrichment in ^{15}N and ^{18}O increases from soils and groundwater to freshwater and marine sources [34]. Long-term studies have shown that enrichment in heavy N_2O is decreasing over time due to the increased contribution of agricultural sources that are isotopically lighter [35, 36]. The existing atmospheric observations of N_2O isotopologues are sparse and global VMR distributions as a function of latitude and altitude are poorly known.

Satellite measurements can provide near global coverage, which is not possible from *in situ*, balloon, and aircraft platforms. A global isotopic measurement is essential to constrain N_2O sources. Multiple space-based instruments, including MIPAS [37], AIRS [38], and CLAES on UARS [39], have measured N_2O, but do not have isotopologue data. This chapter presents measurements made by ACE-FTS of parent N_2O and its 3 main isopologues of $NN^{18}O$, ^{15}NNO, and $N^{15}NO$ for the first time up to $\sim$ 45 km.

4.2 ACE data retrieval

The ACE-FTS is a high resolution (0.02 cm^{-1}) infrared Fourier transform spectrometer on board the Canadian satellite SCISAT [14, 15]. SCISAT was launched in 2003 and is still currently active. The satellite orbits around the Earth at a height of 650 km with 74° inclination angle to the equator. SCISAT makes measurements by solar occultation, i.e., it uses the sun as a light source in order to measure the absorption of the atmosphere during sunrise and sunset. The satellite period is 98 minutes which enables a measurement about every 49 minutes. About 30 measurement locations each day form two longitude circles (sunrise and sunset) and the latitude of those circles changes slowly, with about 2 months needed to cover the globe (Figure 25). The pressure and temperature profiles as a function of altitude are determined from the ACE-FTS spectra by analyzing selected CO_2 lines using a fixed assumed volume mixing ratio (VMR) profile for CO_2 below 60 km, since CO_2 is well mixed and has a nearly constant VMR over much of middle atmosphere [16]. The temperature is determined from the relative intensity of the CO_2 lines and the pressure from the optical depth of the lines. The pressure is converted to altitude using a weather forecast model. The VMR retrieval of molecules and related isotopologues is done by using a set of microwindows, which are small portions of spectrum (typically less than 0.5 cm^{-1}) for the molecule of interest, which contain minimal interference from other molecules. The microwindows used for these species include lines from the $2\nu_2$, ν_3, and ν_1 N_2O vibrational modes [40]. A summary of the microwindows used is given in Table 3. A more complete version of the microwindows and the interfering molecules is accessible from the `http://www.ace.uwaterloo.ca/instruments_acefts.php`.

The temperature and pressure are held fixed on a grid with 1 km spacing up to 150 km. VMRs are retrieved by comparing the observed ACE-FTS spectra with the

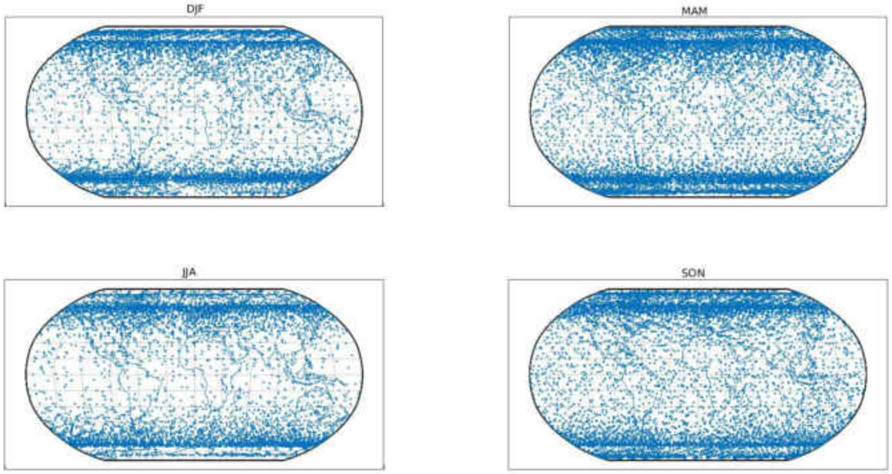

FIG. 25: Distribution of ACE measurements by season (winter: DJF, December, January, February; spring: MAM, March, April, May; summer: JJA, June, July, August; fall: SON, September, October, November)

calculated spectra from the forward model and adjusting the VMRs until residuals in the microwindows are minimized. Spectroscopic data employed in the forward model calculations in version 3.5 processing come mostly from the HITRAN 2008 database [41]. The data retrieval using version 3.5 of the ACE-FTS software is very similar to version 3.0, with some slight improvements [40, 16]. The number of interfering molecules (molecules or isotopologues other than the target molecule that have significant absorption within the set of microwindows) is increased in versions 3.0 and 3.5 for N_2O. A list of interfering molecules is presented in Table 4.

The retrieval of the isotopologues of N_2O that were added in the versions 3.0 and 3.5 includes $N^{15}NO$, ^{15}NNO, $NN^{18}O$, and $NN^{17}O$. $NN^{17}O$ was not included in this study because the quality of the retrieved data was not satisfactory.

The ACE data used in this chapter consist of more than 30000 occultations containing profiles of N_2O and the three isotopologues $NN^{18}O$, ^{15}NNO, and $N^{15}NO$. The ACE N_2O isotopic data set contains a large amount of non-physical data when compared to other molecules. Several steps were taken to remove this bad data and improve the final results. First, data flagged as outliers were removed (data flagged as 1 and 2 were kept; for flags 4-7, the entire profile was removed) [42].

TABLE 3: Microwindow summary for N_2O and its daughter isotopologues

Isotopologue	Altitude range (km)	number of microwindows	Vibrational modes and wavenumber ranges (cm^{-1})
N_2O	5-95	66	$2\nu_2$: 1134.2 – 1204.7 ν_3: 1264.7 – 1277.1 ν_1: 2201.8 – 2242.0 $2\nu_3$: 2566.2 – 2623.9
^{15}NNO	7-45	35	$2\nu_3$: 1231.4 – 1250.7 ν_1: 12160.6 – 2220.9
$N^{15}NO$	5-45	41	$2\nu_1$: 2140.2 – 2196.8
$NN^{18}O$	5-45	40	ν_3: 1223.7 – 1235.5 ν_1: 2177.9 – 2333.6

This reduced the number of occultations from 32,024 to 28,689. Next, profiles containing a negative VMR value were removed. While negative concentrations are allowed in ACE retrievals (where the value is very small and has a large absolute error), they are not valid when calculating delta values. The removal further reduced the number of occultations used to 17,183. Finally, filtering using the median absolute deviation (MAD) was performed on the data points. MAD is defined as $MAD = Median_i(|x_i - median_j(x_j)|)$, and is less sensitive than the standard deviation to extreme outliers. The data set was binned by season, 10° latitude, and each altitude level and a MAD was calculated for each bin. Values with an absolute deviation higher than the MAD multiplied by 5 were discarded. This did not remove any full profiles.

After removing non-physical data and outliers, the δ values were calculated for each isotopologue using equations 64 and 65.

The ACE δ values in the troposphere were compared to *in situ* values measured

TABLE 4: Interfering species for N_2O and its daughter isotopologue

Isotopologue	Interfering species
N_2O	^{15}NNO, $NN^{18}O$, H_2O, HDO, $H^{18}OH$, CO_2, $OC^{18}O$, $O^{13}C^{18}O$, CO, CH_4, $^{13}CH_4$, CH_3D, $N^{15}NO$, O_3, HNO_3, CHF_2Cl
^{15}NNO	N_2O, $N^{15}NO$, $NN^{18}O$, $NN^{17}O$, H_2O, HDO, CO_2,$^{13}CO_2$ $OC^{18}O$, O_3, CO, CH_4, $^{13}CH_4$, CH_3D, H_2O_2, COF_2
$N^{15}NO$	N_2O, ^{15}NNO, $NN^{18}O$, $NN^{17}O$, H_2O, CO_2, $^{13}CO_2$, $OC^{18}O$, $OC^{17}O$,O_3, CO, ^{13}CO, $C^{18}O$, $C^{17}O$, CH_4, $^{13}CH_4$, CH_3D
$NN^{18}O$	N_2O, ^{15}NNO, $N^{15}NO$, $NN^{17}O$, H_2O, HDO, $^{13}CO_2$, $OC^{18}O$, $OC^{17}O$, CH_3D, H_2O_2, COF_2

on the ground and a small calibration factor of 0.9995 was applied to the isotopologue R values, based on *in situ* tropospheric values. For further analysis, the ACE observations in this study shown in Figure 25 are binned in 10° latitude bins on a 1 km altitude grid.

As a validation of ACE data, the altitude profile of ACE δ values from the corresponding latitude bin for the 3 heavy isotopologues were compared to the balloon measurements collected by Kaiser et al. [43] (See Figure 26). The balloon measurements by Kaiser et al. [43] were made over Arctic (75° N–80° N); Arctic (80 ° N–87 ° N); Kiruna, Sweden (67.9° N, 21.10° E); Aire sur l'Adour, France (43.70° N, 0.30° E); Gap, France (44.44° N, 6.14° E); and Hyderabad, India (17.5° N, 78.6° E). In general, all profiles show increasing enrichment in all three isotopologues with a stronger increase closer to the poles. In all cases, $\delta^{15}N^1$, $\delta^{15}N^2$, and $\delta^{18}O$ from ACE observations show a good agreement with the balloon and aircraft measurements.

The global distribution of δN values from ACE for the seasons are displayed in Figure 27 for $\delta^{15}N^2$, $\delta^{15}N^1$, and $\delta^{18}O$. The general pattern is the same for all three isotopologues: the heavier molecules are enriched in the stratosphere over the poles. The Brewer-Dobson circulation transfers older air with heavier isotopologues from the tropics to the poles. Moreover, Figure 27 shows the seasonal variation for the $^{15}N^1$,$^{15}N^2$, and ^{18}O isotopologues. In Dec/Jan/Feb and Mar/Apr/May, there is more sunlight over the South Pole, which leads to the enrichment of the heavier isotopologues (Figure 27), while, during Jun/Jul/Aug and Sept/Oct/Nov, the heavier isotopologues are enriched over the North Pole, where there is more sunlight (Figure 27). It appears that the $^{15}N^2$ is slightly more enriched at lower altitudes than $^{15}N^1$; this can be explained by the ^{15}N site dependent fractionation of the $^{15}N^1$ and $^{15}N^2$ isotopologues [31].

4.3 Conclusion

For the first time, a global measurement of nitrous oxide isotopologues has become possible from the ACE-FTS observations in the upper troposphere and stratosphere. An evaluation of ACE-FTS data was made by comparing the N_2O isotopologues enrichment to the balloon observations, which shows a good agreement between the two sets of measured data.

The heavier isotopologues (^{15}NNO, $N^{15}NO$, and $NN^{18}O$) are enriched with increasing altitude and increasing latitude in the stratosphere. As the air ages and is exposed to sunlight for a longer time, a decrease in the parent N_2O VMR and an increase in the relative abundance of the heavier isotopologues occur. A seasonal variation of N_2O enrichment was observed over the poles for all isotopologues.

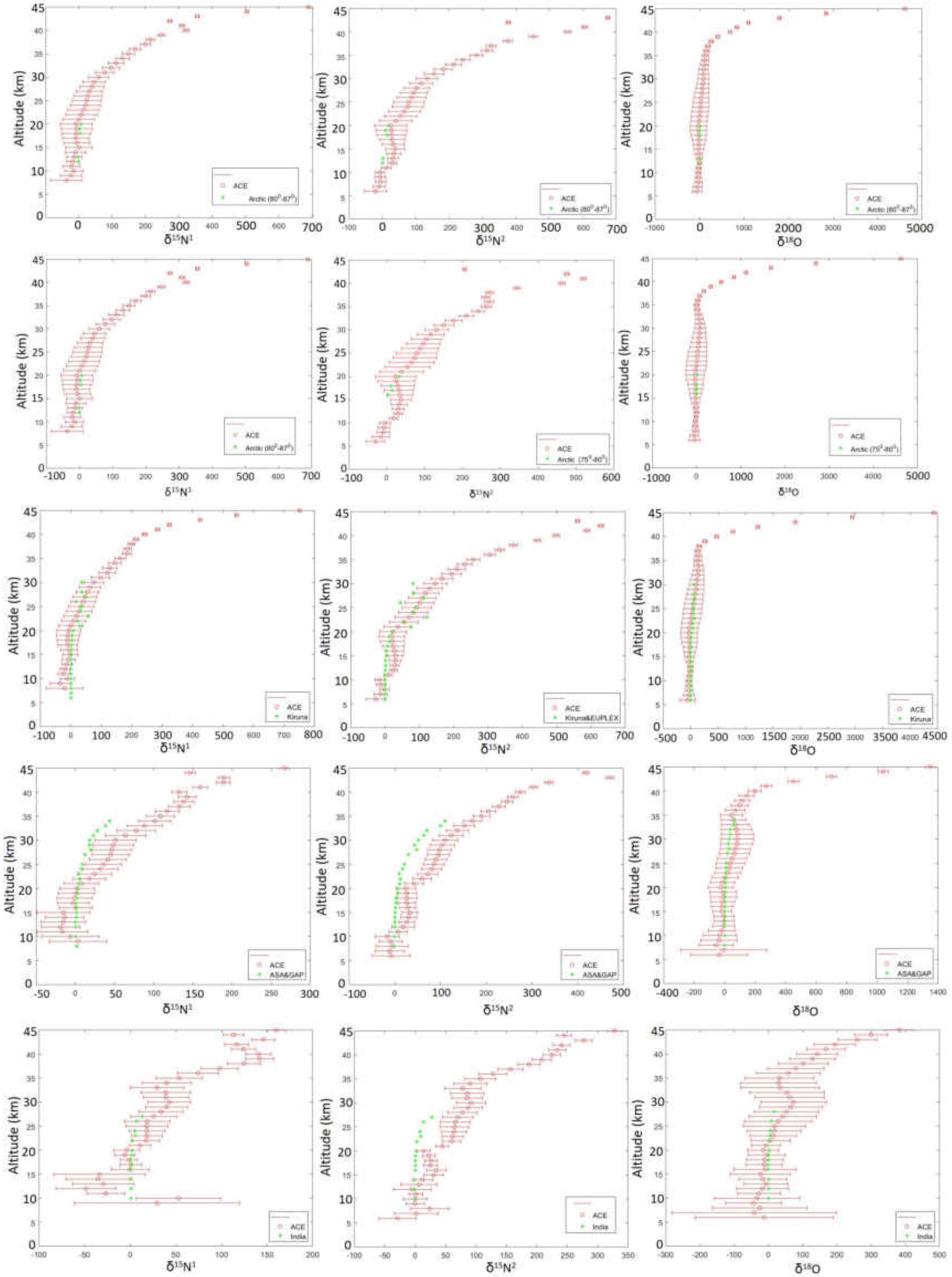

FIG. 26: Comparison of mission average ACE δ values with one standard deviation error bars for the ^{15}N^1, ^{15}N^2, and ^{18}O isotopologues in the over Arctic (75°-87°), Kiruna, Sweden (67.9° N, 21.10° E), ASA& GAP, France (43.70° N-44.44° N), Heydarabad, India (17.5° N, 78.6° E) high altitude balloon flights [43].

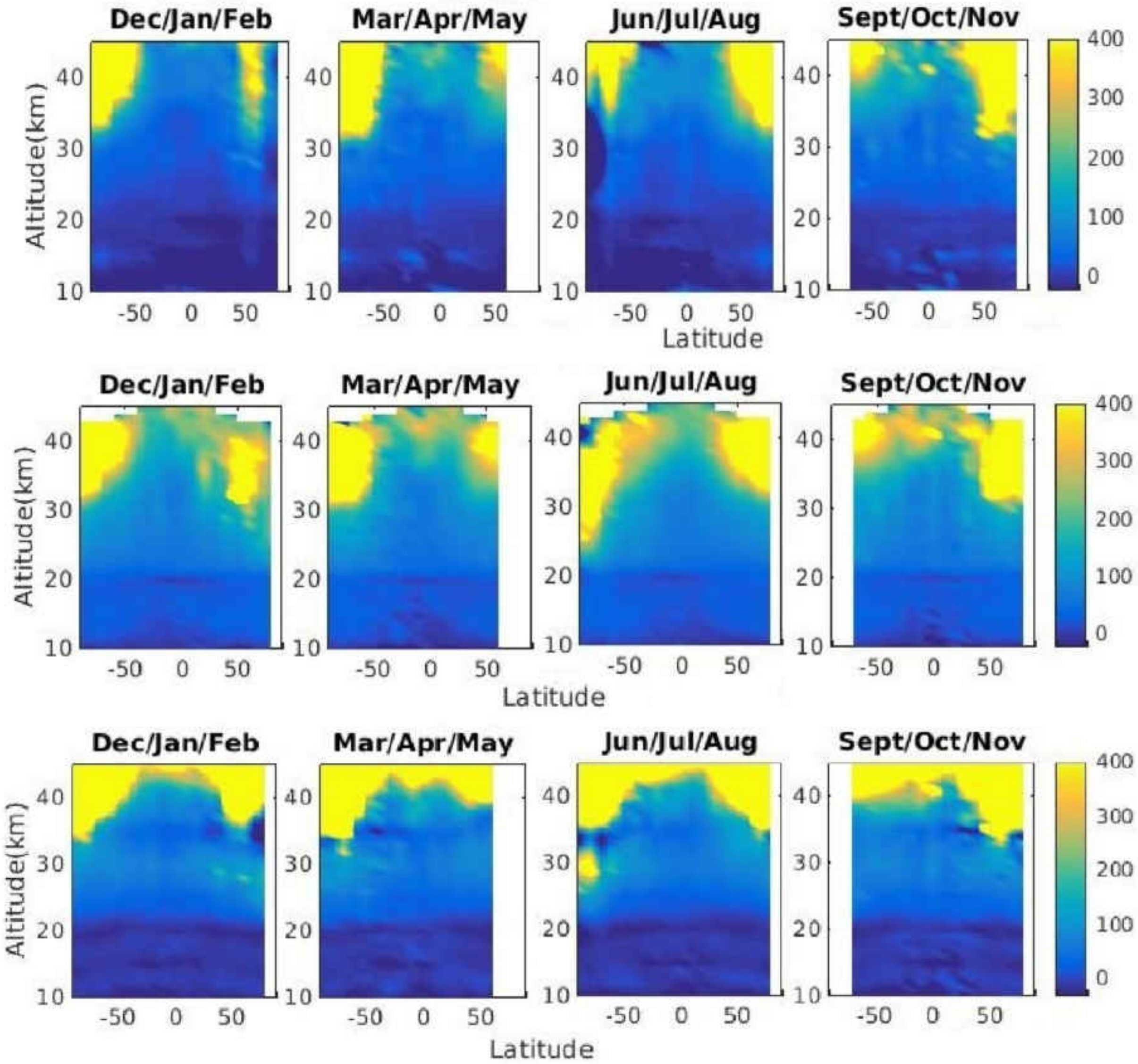

FIG. 27: Observed ACE global distributions for (a) $\delta^{15}N^1$, (b) $\delta^{15}N^2$, and (c) $\delta^{18}O$.

CHAPTER 5

GLOBAL MEASUREMENTS OF ATMOSPHERIC CARBONYL SULFIDE (OCS), $OC^{34}S$ AND $O^{13}CS$

The majority of the material and results in this paper are published in the Journal of Quantitative Spectroscopy & Radiative Transfer ([45]). Goeffrey Toon (co-author) provided the balloon measurement data for $OC^{34}S$ and $O^{13}CS$ isotopologues (36) recorded by JPL. This study was supervised by Peter F. Bernath (co-author). As the first author, the analysis of ACE satellite data, preparation of figures, and writing the paper were done by me.

5.1 Introduction

Carbonyl sulfide (OCS) is the most abundant sulfur-containing gas in the atmosphere. The OCS distribution, sources and sinks have been studied in the troposphere [44, 46, 47]. The main source of OCS is biogenic activity either from direct emission or indirectly by oxidation of CS_2 and dimethyl sulfide (DMS). Biomass burning [48], soil and wetland emissions [46] are additional biogenic sources of OCS.

OCS is also emitted by anthropogenic activities, particularly by oxidation of CS_2 that is released by industry. Uptake by vegetation and soil are the major tropospheric sinks of OCS. The destruction of OCS by plants can be used to study the carbon cycle in the troposphere [47]. OCS assimilation by plants is assumed to be similar to the photosynthetic uptake of CO_2 but is irreversible [47].

The total OCS atmospheric lifetime is estimated to be 2.5 years [49]. Due to its low reactivity and relatively long lifetime, OCS is the only sulfur containing gas that can reach the stratosphere except following major volcanic eruptions during which SO_2 is directly injected into the stratosphere. In the stratosphere, OCS is destroyed by reaction with OH or O radicals,

$$\mathrm{OCS + OH \longrightarrow CO_2 + SH} \tag{66}$$

$$\mathrm{OCS + O\,(^3P) \longrightarrow CO + SO} \cdot \tag{67}$$

However, the main sink of OCS in the stratosphere is via photolysis [50, 51, 52],

$$\mathrm{OCS + h\nu \longrightarrow CO + S\,(\lambda \leq 300\,nm\,)} \cdot \tag{68}$$

Danielache et al. [53] calculate that reaction 66 with OH dominates in the troposphere, reaction 67 with O is responsible for 20 % of OCS destruction in the stratosphere and photolysis 68 at 80 % dominates in the stratosphere. The stratospheric lifetime of OCS mainly due to photolysis is estimated to be 64 years [54].

The sulfur products produced from the above reactions (SH, SO and S) are rapidly oxidized in the stratosphere to SO_2. SO_2 is converted to sulfate aerosol by reaction with OH, so OCS is a precursor to stratospheric sulfate aerosol (SSA) [51]. SSA is an optically thin layer of sulfuric acid droplets that extends from the tropopause upwards into the stratosphere, also called the Junge layer. SSA reportedly has an average negative radiative forcing of -0.40 ± 0.2 W m^{-2} and cools the climate by increasing the Earth's albedo [3].

OCS is known to be one of the major long term contributors to the SSA. Large volcanic eruptions are another contributor to the SSA by direct injection of SO_2 into the stratosphere, but their effects are temporary [55]. It is difficult to assess the OCS contribution to SSA because of the large uncertainty in its sources and sinks [51, 56, 57]. For example, Watts estimates OCS global sources and sinks of 1.31 ± 0.25 and 1.66 ± 0.79, respectively [56].

Trace gas isotopologues can give additional information about atmospheric chemistry and dynamics [58, 59]. Isotopes have been used to determine the contribution of OCS to SSA. Castleman et al. [60] found a $\delta_{sulfate} \sim 2.6$ ‰ for ^{34}S for the background SSA and concluded that tropical upwelling of OCS is a major contributor [60].

Chin and Davis [51] used a one dimensional photochemical model and, based on an OCS stratospheric lifetime of 10 years, concluded that the production rate of SSA from OCS oxidation is 2 to 5 times less than the amount of sulfur required to maintain the SSA. In contrast, Barkley et al. [54] found a more realistic stratospheric OCS lifetime of 64 ± 21 years using the measurements obtained by Atmospheric Chemistry Experiment (ACE) satellite corresponding to a stratospheric sink of 63–124 Gg yr^{-1} (34–66 GgS yr^{-1}) which is in the range of sulfur mass estimated by Chin and Davis [51] that is needed to sustain the SSA. Subsequently, Krysztofiak et al. [61] found a stratospheric OCS sink of 54 ± 14 GgS yr^{-1} using SPIRALE and SWIR balloon borne measurements in agreement with the conclusion of Barkley et al. [54].

Leung et al. [62] tried a different approach to estimate the contribution of OCS to the SSA by measuring the OCS isotopic fractionation. Leung et al. [62] found a fractionation factor of the $\epsilon \sim 73 \pm 8.6$ ‰ for OC^{34}S with the MkIV balloon-borne FTS, implying that the SSA should be enriched in ^{34}S. Leung et al. [62] cited the study of Miller and Yung [63] that suggested a faster photolysis of OC^{34}S compared to OC^{32}S. Collusi et al. [64] also measured the absorption cross sections of OC^{32}S and OC^{34}S and concluded that the OC^{34}S absorption cross section is larger than that of OC^{32}S between $200 < \lambda(\mathrm{nm}) < 260$ at 298 K near the absorption maximum.

Later, Hattori et al. [65] reported on extensive measurements of UV absorption cross sections of OCS isotopologues between 190 to 260 nm that are inconsistent with the results of Collusi et al. [64]. They found similar absorption cross section for OC^{32}S and OC^{34}S and estimated a small fractionation factor of $^{34}\epsilon \sim 1.1 \pm 4.2$ ‰. Lin et al. [66] reported on laboratory experiments on the photolysis of OCS. They found the fractionation factor $^{34}\epsilon$ to be between -10.5 to 5.3 ‰.

In another study, Hattori et al. [67] analyzed the sulfur isotopic compositions of OCS using gas chromatography and mass spectrometry (GC-IRMS) of air collected at Kawasaki, Japan and reported a tropospheric value of $\delta^{34}\mathrm{S}_0$ of 4.9 ± 0.3 ‰. Hattori et al. [67] used a similar analysis to Leung et al. [62] and estimated the stratospheric ^{34}S enrichment value to be -3.4 to 2.7 ‰ which is in agreement with the SSA enrichment value measured by Castleman et al. [60]. Hattori et al. [67] concluded that OCS is an important source of SSA.

Despite widespread tropospheric OCS observations [47, 48], stratospheric OCS observations are more limited (e.g., [68, 69, 70]). More studies with wider geographical coverage will help determine the contribution of OCS to the SSA.

In this study we use ACE-FTS data to study OCS, $O^{34}CS$ and the $OC^{13}S$ isotopologues in the stratosphere. Similar data from the balloon-borne MkIV FTS are also used. The main objectives are to investigate the global zonal and seasonal distributions of OCS, $O^{13}CS$ and $OC^{34}S$; and to study the isotopic composition of OCS in the stratospheric to assess its contribution to background SSA.

5.2 ACE satellite data

SCISAT, also known as the Atmospheric Chemistry Experiment (ACE), is a satellite developed by the Canadian Space Agency (CSA) for infrared remote sensing of the Earth's atmospheric composition [15, 71]. It was launched by NASA into a circular orbit at 650 km altitude with a high 74° inclination to the equator in August 2003. Routine measurements began in late February 2004. The main instrument on board SCISAT is a high resolution Fourier transform spectrometer (ACE-FTS). ACE-FTS has a spectral resolution of 0.02 cm^{-1} covering the spectral range of 750 to 4400 cm^{-1} (2.2 to 13.3 μm). ACE-FTS uses the solar occultation technique which records atmospheric transmission spectra during sunrise and sunset in the limb geometry using the Sun as an infrared source.

Profiles of 35 trace gases, as well as 20 isotopologues are retrieved from ACE-FTS spectra using version 3.5/3.6 of the ACE-FTS data processing [72] with a vertical resolution of about 3 km [71]. ACE-FTS retrieves $^{16}O^{12}C^{32}S$, $^{16}O^{12}C^{34}S$ and $^{16}O^{13}C^{32}S$ isotopologues of carbonyl sulfide, which have natural abundances of about 95 %, 4 % and 1 % [73]. The pressure and temperature profiles as a function of altitude are first determined using selected CO_2 lines. Temperature profiles are determined by the relative intensity of selected CO_2 lines and the pressure profiles from the optical depth of the lines. Altitude registration is performed using information from the Canadian weather service model and the error in the final retrieved tangent height is about 50 m.

The OCS VMRs are retrieved in a second step, holding the temperature and pressure constant. To speed up processing, a set of microwindows (less than 0.5 cm^{-1} wide) is chosen for the retrieval. For each molecule these microwindows are chosen to minimize the interference with other molecules. The microwindow sets for the retrieval of $OC^{32}S$, $OC^{34}S$ and $O^{13}CS$ are presented in tables S1–S3 [45], respectively. The VMRs are adjusted by comparing the observed spectrum and the calculated spectrum from the forward model and minimizing the residuals. The atmospheric model consists of 150 spherical layers, each 1 km thick. A ray tracing program is used to determine the path for each tangent height and the Beer-Lambert law is used to calculate the spectrum. In this study version 3.5/3.6 of the ACE-FTS processing is used with most of the spectroscopic constants taken from the HITRAN 2004 database. The constants for OCS however were taken from an update that appeared in the HITRAN 2008 database [73]

5.3 Data Analysis

More than 60,000 occultations are available for the 2004–2017 period in version 3.5/3.6 of ACE data. The ACE OCS data set contains profiles with unphysical spikes or oscillations, which need to be removed for optimal use of the results. These artifacts are due to missing data and low signal-to-noise ratio particularly for the minor isotopologues [72]. In the troposphere, clouds and aerosols also cause problems with the retrievals. The statistical retrieval error for the main OCS isotopologue is less than 2 % up to 19 km and increases to $\sim$ 4 % at higher altitudes. The statistical error for $OC^{34}S$ varies from 9 to 12 % up to 17 km and increases to 15 to 50 % at higher altitudes. The statistical error for $O^{13}CS$ is $\sim$ 20–33 % from 7–18 km and increases to 45–100 % at higher altitudes. Several steps were taken to filter these bad data and improve the data quality. In the first step, negative VMR values were removed; while negative concentrations are allowed in ACE retrievals, they are not valid when calculating delta values. Secondly, the OCS VMRs with an uncertainty greater than 73 ppt were discarded. Also the VMRs for all isotopologues that are not determined within their uncertainty were discarded. In addition, the median absolute deviation (MAD) was calculated at each altitude to filter outliers. MAD is defined as MAD=$\text{median}_i(\mid x_i - median_j(x_j) \mid)$ and is less sensitive than the standard deviation to extreme outliers. Values with an absolute deviation greater than 3 × MAD were discarded.

The ACE-FTS OCS retrieval also suffers from systematic errors that we estimate by comparison with an independent measurement made with the MkIV instrument at Ft. Sumner, New Mexico (35° N) and Esrange, Sweden and Fairbanks, Alaska (65° N). We found a percentage difference of 0.3–1 % for 35° N and 0.16–4 % for 65° N between the two independent measurements.

After filtering nonphysical data and outliers, the delta values and the corresponding fractionation uncertainties for each isotopologue were calculated,

$$\delta^{13}C = (\frac{^{13}R_{sample}}{^{13}R_{std}} - 1) \times 1000 \qquad ^{13}R = \frac{[O^{13}CS]}{OCS} \tag{69}$$

$$\delta^{34}S = (\frac{^{34}R_{sample}}{^{34}R_{std}} - 1) \times 1000 \qquad ^{34}R = \frac{[OC^{34}S]}{OCS} \tag{70}$$

in which the ^{13}R$_{std}$=0.041583 and ^{34}R$_{std}$=0.010531 values are from HITRAN 2016 database [73]. Finally, the δ^{34}S values with fractionation uncertainties larger than 800 ‰ and δ^{13}C values with uncertainties larger than 1000 ‰ were discarded.

5.4 Results and discussion

5.4.1 OCS Global distribution

The global distribution of OCS using ACE-FTS data was studied by Barkley et al. [54]. They found an enhanced OCS concentration at 10–15 km between 0° and 30° N attributed to tropical biomass burning [48]. Barkley et al.'s results did not support previous model studies that suggested a large oceanic source at high SH latitudes [46]. In this study, we used ACE-FTS data to obtain a global distribution of OCS from the mission average. The ACE-FTS mission average VMRs from 2004 to 2017 are binned in 10° latitude bins on a 1 km altitude grid. Figure 28 shows the OCS mission average global distribution from 2004 to 2017. A high OCS abundance is seen in the upper troposphere (UT) and lower stratosphere characteristic of upwelling in the tropics. This high OCS abundance over the tropics extends up to 20–25 km and decreases with increasing altitude and latitude. An enhancement of OCS is also observed in the NH between 0°–30° N up to 15 km, in agreement with Barkley et al. [54].

5.4.2 OCS vertical profile

The ACE-FTS OCS observations were sorted into 6 latitude bins covering the equator and mid-latitudes in the Northern Hemisphere (NH) and southern Hemisphere (SH). Figure 29 shows the vertical profiles of ACE mission average OCS

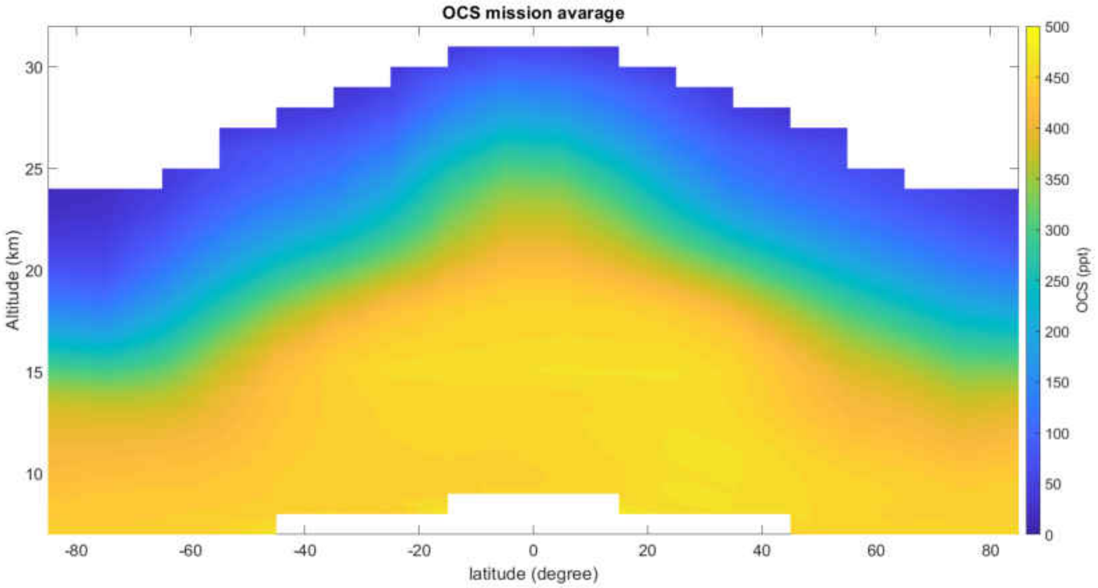

FIG. 28: Global atmospheric distribution of OCS from the ACE mission average. The OCS VMR values have been grouped together in 10° latitude bins.

VMRs binned for 6 different latitude bins 85° S – 60° S, 60° S – 30° S, 30° S – 0° S, 0°– 30° N, 30° N – 60° N and 60° N – 85° N on a 1 km altitude grid. As the altitude increases, OCS VMRs decrease as a result of photolysis and chemical reactions. The OCS VMRs remain constant within error over the tropics up to 15 km.

The NH and SH OCS VMRs were compared by computing tropospheric and stratospheric average values for the 6 latitude bins for the corresponding latitude bins in the NH and SH. Overall OCS tropospheric VMRs are about 10 ppt greater in the NH than SH for all latitude bins. In the stratosphere, in the mid-latitude and in the poles these differences are ∼ 10 ppt and ∼ 40 ppt. In addition, the ACE OCS altitude profiles were compared to the MkIV OCS measurements at 35° N and 65° N latitude. Data points from MkIV OCS measurements with the errors larger than 73 $\times 10^{-12}$ (73 ppt) were also discarded. This reduced the total number of data points from 756 to 572. Velazco et al. [74] performed a ACE-MkIV OCS comparison that used potential temperatures and equivalent latitudes from analyzed meteorological fields to find comparable ACE and MkIV profiles, despite the lack of spatio-temporal coincidence. This study found reasonable agreement, but with MkIV OCS somewhat larger.

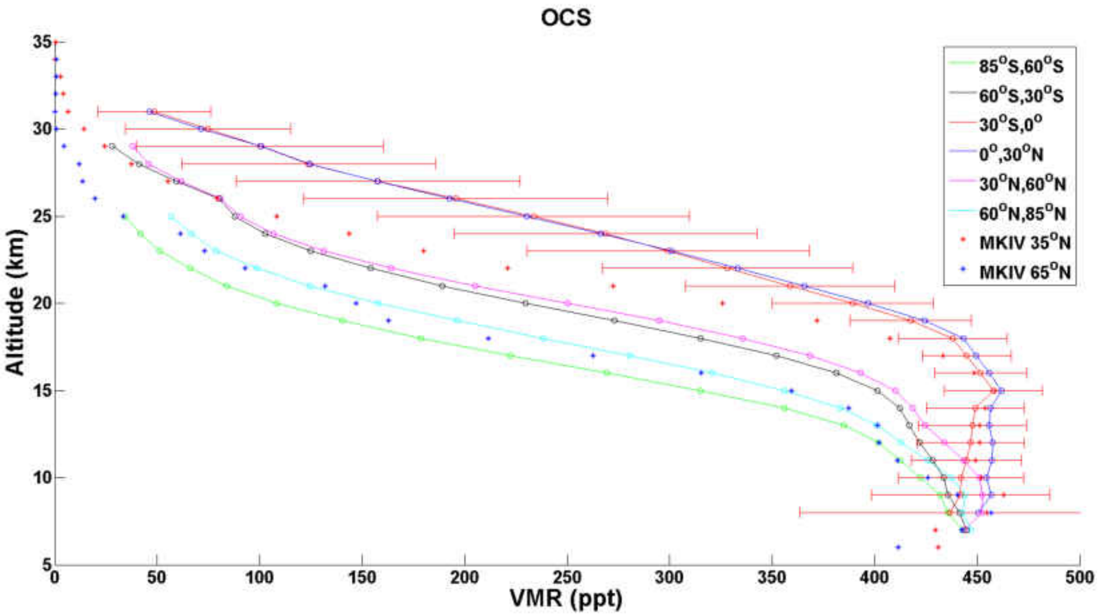

FIG. 29: Mean latitudinal OCS profiles measured by ACE on a 1 km vertical grid and averaged from February 2004 to December 2017 for the 6 latitude bins for 85° S – 60° S, 60° S – 30° S, 30° S – 0° S, 0° – 30° N, 30° N – 60° N and 60° N – 85° N, compared to the MkIV OCS measurements in the 35° N (red asterisks) and 65° N (blue asterisks). Because of similar error bars for all latitude bins, only error bars for one latitude bins are presented.

5.4.3 OC^{34}S isotopologue global fractionation

The global distributions of OCS isotopologues provide information on the role of OCS in climate change [75]. As outlined in the introduction, there are contradictory views on the contribution of OCS to the background SSA. ACE-FTS data are used to obtain seasonal and zonal distributions of OC^{34}S fractionation. The δ^{34}S values were binned in 10° latitude bins and the global distribution of $\delta^{34}S$ during winter (DJF), spring (MAM), summer (JJA) and fall (SON) are presented in Figure 30. Overall Figure 30 shows an almost constant enrichment of OC^{34}S in the troposphere. As OC^{34}S penetrates into the stratosphere, there is a small fractionation of OC^{34}S that varies by season.

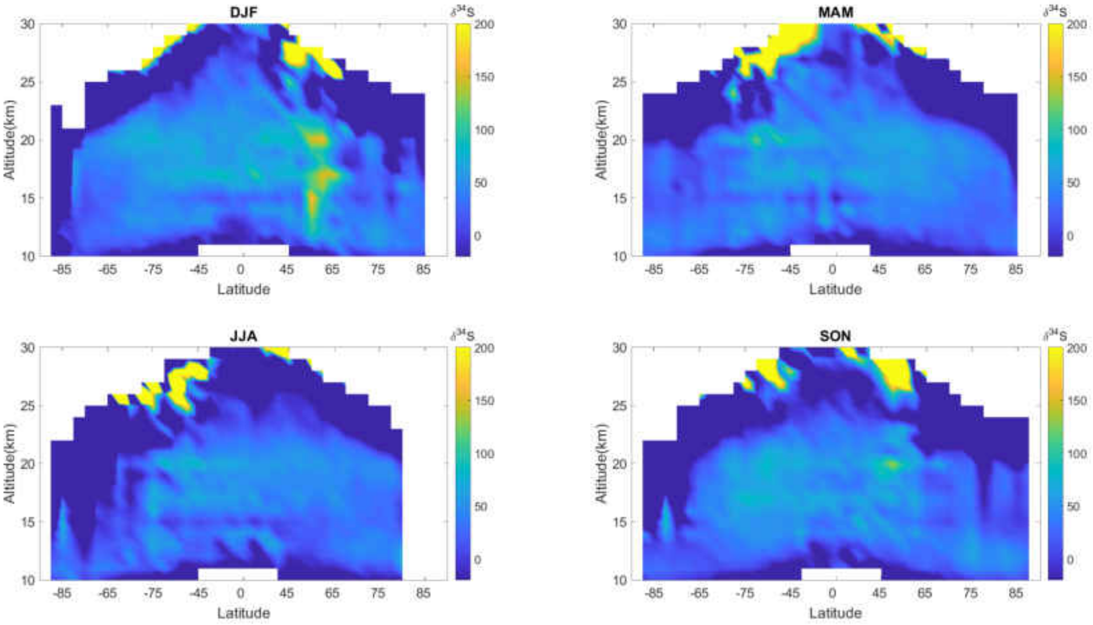

FIG. 30: Seasonal zonal distributions of δ^{34}S observed by ACE from 2004 to 2017. The δ^{34}S values have been grouped together in 10° latitude bins.

5.4.4 $\delta^{34}S$ altitude profile

The altitude profile of OC^{34}S fractionation obtained from ACE-FTS mission average between 2004 to 2017 for the latitude bins of 85° S – 60° S, 60° S – 30° S, 30° S – 0° S, 0° – 30° N, 30° N – 60° N and 60° N – 85° N were investigated. Figure 31 shows that despite some fluctuations in the δ^{34}S values with altitude, these changes in ^{34}S enrichment are insignificant and lie within the error bars; therefore no major enrichment of ^{34}S is observed for all latitude bins. The sharp increase in the OC^{34}S enrichment above 25 km, particularly in the tropics, is an artifact, related to the larger measurement errors.

5.4.5 O^{13}CS isotopologue global fractionation

The δ^{13}C values were binned in 10° latitude bins on a 1 km altitude grid with the data sorted into DJF, MAM, JJA and SON. The global distribution of δ^{13}C is presented in Figure 32. An increasing enrichment in ^{13}C with altitude is observed in the stratosphere. Again a very sharp increase at the top of the altitude range may

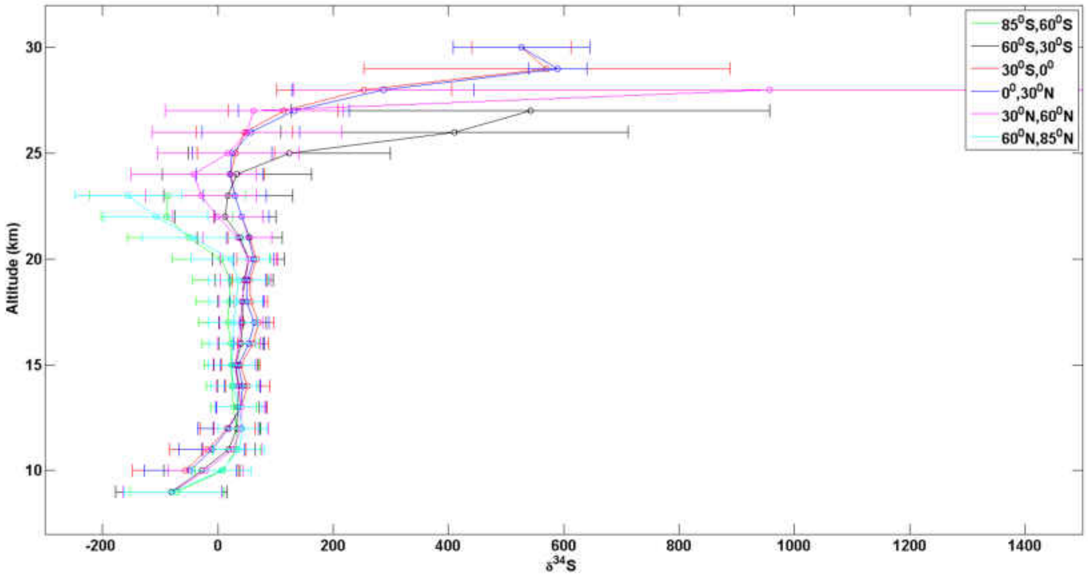

FIG. 31: Latitudinal δ^{34}S profiles measured by ACE on a 1 km vertical grid and averaged from February 2004 to December 2017. Latitudinal δ^{34}S profiles have been plotted for 6 bins for 85° S – 60° S, 60° S – 30° S, 30° S – 0° S, 0° – 30° N, 30° N – 60° N and 60° N – 85° N.

be an artifact.

As the stratospheric air increases in altitude, it becomes older and has been exposed to more UV light. The $O^{13}CS$ enrichment with altitude results from the different absorption cross sections for $O^{13}CS$ and OCS. $O^{13}CS$ cross sections from 190 to 260 nm are less than the main OCS cross sections [65, 76] and therefore $O^{13}CS$ is photolyzed less. This causes the increase in δ^{13}C with increasing altitude as $O^{12}CS$ is more fractionated by photolysis. The seasonal variation of δ^{13}C (Figure 32 (a–d)) shows more enrichment of $O^{13}CS$ during DJF in the SH (Figure 32 (a)) and during JJA in the NH (Figure 32 (c)) at mid-latitudes due to the increased sunlight that leads to the more fractionation of OCS while the cold polar air in the NH (DJF) and in the SH (JJA) that is older and more enriched in $O^{13}CS$ descends to the lower stratosphere (Figure. 32 (a & c)). We observe the formation of the Arctic and Antarctic polar vortices during DJF in the NH (Figure 32 (a)) and during JJA in the SH (Figure. 32 (c)) that contain older air enriched in $O^{13}CS$. During MAM the enrichment begins to increase in the NH (Figure 32 (b)) and during the SON, the enrichment begins to increase in the SH (Figure 32 (d)).

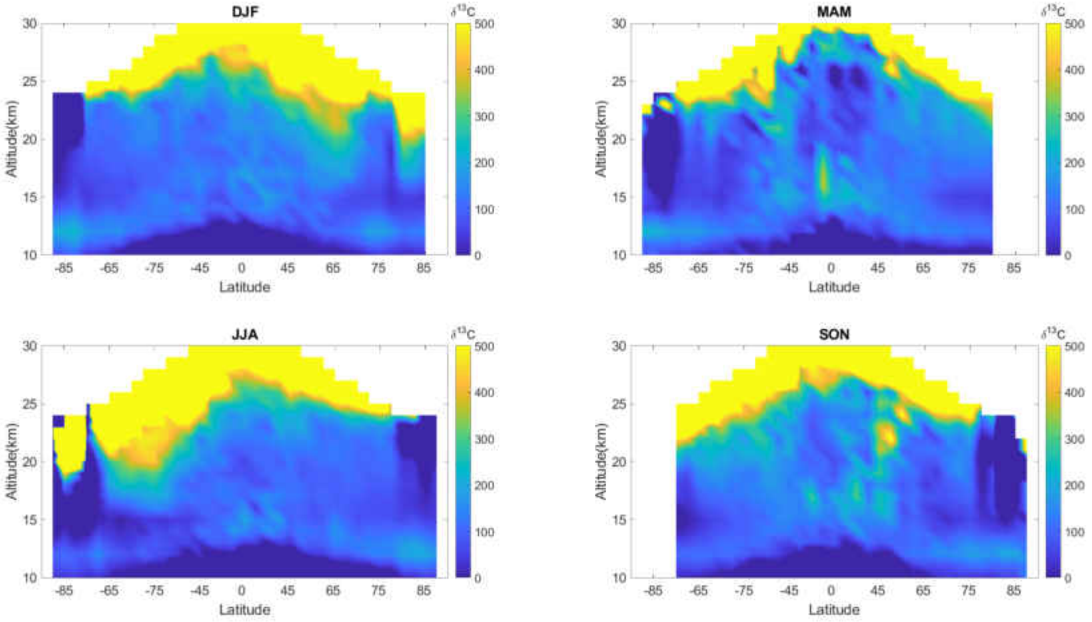

FIG. 32: Seasonal zonal distribution of δ^{13}C observed by ACE from 2004 to 2017. The enrichment values have been grouped together in 10° latitude bins.

5.4.6 $\delta^{13}C$ altitude profile

As for to $OC^{34}S$, the altitude profile of the average $O^{13}CS$ enrichment was sorted into 6 different latitude bins covering the poles, mid-latitudes and tropics. Figure 33 shows the change of the average δ^{13}C values as a function of altitude in the troposphere and stratosphere. The enrichment of $O^{13}CS$ increases with increasing altitude for all latitude bins.

5.4.7 Rayleigh distillation and isotopologue fractionation

The photolysis rate for different OCS isotopologues differs due to different cross sections in the 190–260 nm region which leads to the fractionation of OCS isotopologues,

$$\mathrm{OCS} + \mathrm{h}\nu \xrightarrow{\mathrm{k}} \mathrm{CO} + \mathrm{S}\,(\lambda \leq 300\,\mathrm{nm}\,) \tag{71}$$

$$\mathrm{OC^{34}S} + \mathrm{h}\nu \xrightarrow{\mathrm{k_1}} \mathrm{CO} + {}^{34}\mathrm{S}\,(\lambda \leq 300\,\mathrm{nm}\,) \tag{72}$$

$$\mathrm{O^{13}CS} + \mathrm{h}\nu \xrightarrow{\mathrm{k_2}} {}^{13}\mathrm{CO} + \mathrm{S}\,(\lambda \leq 300\,\mathrm{nm}\,)\cdot \tag{73}$$

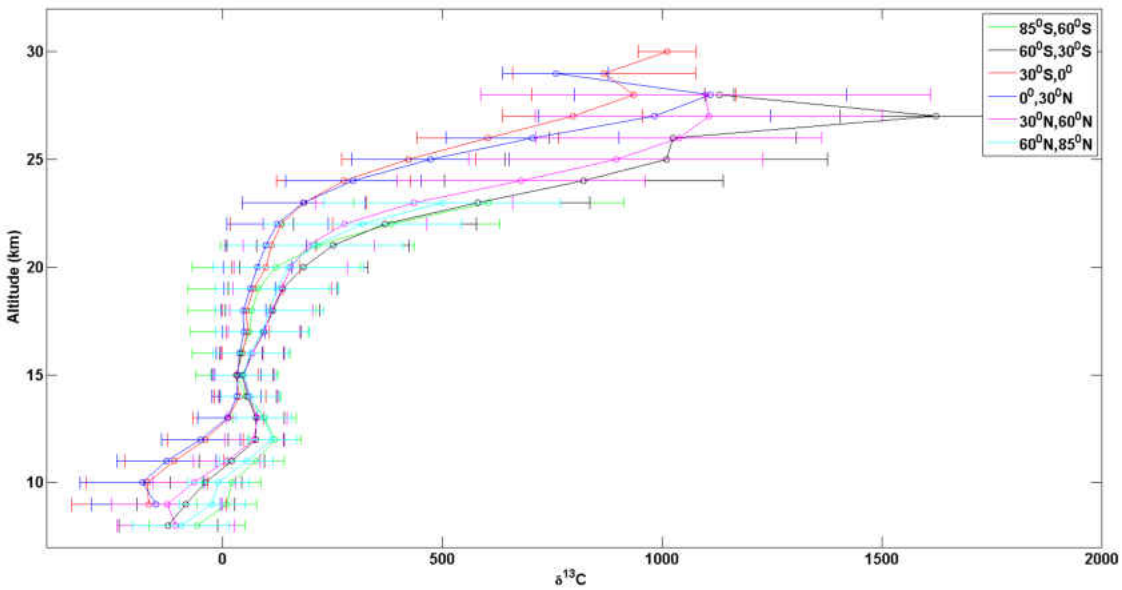

FIG. 33: Latitudinal δ^{13}C profiles measured by ACE on a 1 km vertical grid and averaged from February 2004 to December 2017. Latitudinal δ^{13}C profiles have been plotted for 6 latitude bins for 85° S – 60° S, 60° S – 30° S, 30° S – 0° S, 0° – 30° N, 30° N – 60° N and 60° N – 85° N.

If the rate constants for reactions 71, 72 and 73 are independent of altitude, one can apply a Rayleigh distillation model in which the isotopic ratio at any given altitude z is related to the tropospheric isotopic ratio by [62],

$$R_z = R_0 f^{\alpha - 1} \tag{74}$$

where $R_z = [O^xC^yS/OCS]_z$ (x=13, y=34) is the isotopic ratio for a given altitude, R_{trop} is the tropospheric isotopic ratio, $f=[OCS]_z/[OCS]_{trop}$ is the non-fractionated OCS for a given altitude z and $\alpha_i = k_i/k$ (i=1,2) is the photolysis rate ratio for the two isotopologues. To a good approximation, equation 9 leads to the expression,

$$\delta_z = \delta_0 + \epsilon \ln(\mathrm{f}) \tag{75}$$

where δ_z is the enrichment of the isotopologue of interest at a given altitude z, δ_0 is the tropospheric enrichment at the tropopause and $\epsilon = 1000 \times (\alpha - 1)$ is the enrichment factor of the isotopologue of interest in per mil.

5.4.7.1 Rayleigh distillation of OC^{34}S

We applied the Rayleigh distillation model to the ACE data for OC^{34}S isotopologue fractionation in the stratosphere. The δ^{34}S values were calculated for each individual ACE measurement and are plotted against ln(f). Non-physical data and outliers were discarded using the method described in section 3. Tropospheric OCS VMRs ($[\text{OCS}]_{trop}$) required to calculate the f values are obtained by averaging the ACE-FTS OCS abundances in the troposphere. These values for the 3 latitude bins 60° S – 30° S, 30° S – 30° N and 30° N – 60° N are 435 ppt, 443 ppt and 448 ppt, respectively. Figure 34 (a,b,c) shows the Rayleigh plot of δ^{34}S for the 3 latitude bins. The linear trend of δ^{34}S values shows that the Rayleigh model is applicable for the OC^{34}S isotopologue [62]. The fractionation ($^{34}\epsilon$) can be determined from the slope of Rayleigh plots. A linear fit gives the $^{34}\epsilon$ values of 3.64 ± 0.57, 5.91 ± 0.63 and 8.91 ± 0.47 ‰ for the latitude bins of 60° S – 30° S, 30° S – 30° N and 30° N – 60° N, respectively. These fractionation factors generally agree with the previous values of -1.9 to 1.6 ‰ calculated by Schmidt et al. [76] based on the theoretical calculation of OCS photolysis, the 1.1 ± 4.2 ‰ at 20 km from Hattori et al. [65] obtained from cross section measurements of OCS photolysis. The $^{34}\epsilon$ value for reaction (1) with OH is calculated to be -2.6 ‰ [53] and -14.8 ‰ (or -21.6 ‰ using measured rate constants) for reaction (2) with O atoms [77]. Including these values, Schmidt et al. [78] estimate total $^{34}\epsilon$ values of -5 to 0 ‰ in the stratosphere. Considering the systematic errors in our $^{34}\epsilon$ values from assuming a Rayleigh distillation model, it is not possible to separate the different sink mechanisms in the stratosphere.

The linear regression of ACE-FTS data for the fractionation of ^{34}S isotopologue for the 3 latitude bins in the tropics and mid-latitudes, also gives the δ_0^{34}S values 33.60 ± 0.57, 44.92 ± 0.63 and 32.23 ± 0.47 ‰ respectively, at the tropopause, where OCS begins to fractionate.

The Rayleigh model of ^{34}S isotopologue shows a small fractionation for the equatoral and mid-latitude bins (Figure 35). Considering the error bars, the estimated stratospheric ^{34}S fractionation from ACE-FTS in the tropics and mid-latitudes agrees with the observation of Castleman et al. [60] for SSA and Hattori et al. [65, 67]. Our study, as the first global observation of stratospheric OC^{34}S enrichment, concludes that OCS is a major contributor to the background SSA.

5.4.7.2 Rayleigh distillation of $O^{13}CS$

Similar to the analysis of $OC^{34}S$, we use the Rayleigh distillation model in order to obtain the fractionation factor ($^{13}\epsilon$) for the same latitude bins used in section 4.7.1. The $\delta^{13}C$ values for each individual ACE measurement were calculated and plotted against ln(f), after discarding the non-physical values and outliers. Figure 35 (a,b and c) shows the Rayleigh distillation plots for $\delta^{13}C$ for the 60° S – 30° S, 30° S – 30° N and 30° N – 60° N latitude bins. A linear regression of ^{13}C Rayleigh fractionation plot gives the fractionation factors $^{13}\epsilon$ of -90 ± 1.4, -88 ± 1.92 and -65 ± 1.16 ‰ for the aforementioned latitude bins, respectively. This also gives the $\delta_0^{13}C$ values of 127.13 ± 1.4, 126.82 ± 1.92 and 118.52 ± 1.16 ‰ at the tropopause, for the 3 latitude bins, respectively. Note that the negative sign in the slopes shows the increase of $\delta^{13}C$ with ln(f). Overall, the Rayleigh distillation model for $O^{13}CS$ shows an increasing enrichment with altitude. This increasing enrichment of $O^{13}CS$ with altitude generally agrees with Hattori et al. [65] who estimate a $^{13}\epsilon$ value of -26.8 ± 4.3 ‰ at 20 km for photolysis from the absorption spectra. Schmidt et al.'s stratospheric photolysis values based on ab initio calculations are -3 to -14 ‰ and -5 to -15 ‰ for all three removal reactions [78].

5.4.8 MkIV measurements of $OC^{34}S$ and $O^{13}CS$ fractionation

OCS fractionation has also been measured by the JPL MkIV FTIR spectrometer which covers the 650 to 5650 cm^{-1} range at 0.01 cm^{-1} resolution (60 cm OPD). From 24 high-altitude balloon flights, the MkIV has observed solar occultations allowing the retrieval of profiles of many gases and isotopologues from the clouds tops ($\sim$ 7 km) up to the balloon-float altitude ($\sim$ 40 km). Pre-2001 MkIV measurements of ^{34}S fractionation profiles of OCS were reported by Leung et al. [62]. For the present work, nine more balloon flights were included. Additionally, all spectra, including the pre-2001 ones, were re-analyzed using the latest spectroscopic linelists of OCS and interfering gases, and the latest spectral fitting and retrieval software. Five OCS windows covering 860 to 4120 cm^{-1} were fitted and averaged to determine $OC^{32}S$. One contiguous window covering 2039 to 2076 cm^{-1}, centered on the ν_3 asymmetric OCS stretch band, was fitted for $OC^{34}S$.

Figure 36 shows data obtained from MkIV measurements of OCS, $OC^{34}S$ and $O^{13}CS$ isotopologues. The top panel shows the $\delta^{34}S$ plotted versus ln(f) (f=$[\mathrm{OCS}]_z/[475\ \mathrm{ppt}]$). Data points with fractionation uncertainty of 800 ‰ in δ^{34}S were discarded, reducing the number of data points to 314. The MkIV data give fractionation factors of $^{34}\epsilon$ =4.9 ± 5.31 ‰ and ^{34}S fractionation of 41.72 ± 5.31 ‰ at the tropopause. Overall ^{34}S fractionation obtained from MkIV data shows a good agreement with ACE-FTS data, within the error bars. (Figure 34).

The bottom panel in Figure 36 shows the O^{13}CS fractionation. Data points with fractionation uncertainty larger than 1000 ‰ were discarded, reducing the number of data points to 295. The MkIV data shows a O^{13}CS enrichment factor of $^{13}\epsilon$= -95.3 ± 12.7 ‰ and δ_0^{13}C value of 87.6 ± 12.68 ‰ at the tropopause. The MkIV data also show an increasing enrichment for O^{13}CS isotopologue, which is in agreement with ACE-FTS observation of O^{13}CS (Figure 35).

5.5 Summary and conclusions

We used ACE-FTS measurements of OCS, OC^{34}S and O^{13}CS to study the zonal and seasonal profiles of stratospheric OCS. The ACE global distribution shows an uplift of OCS-rich air from the tropics into the stratosphere. In the stratosphere as OCS is destroyed it moves poleward and then downward due to the Brewer-Dobson circulation.

The atmospheric fractionation of OCS isotopologues was studied. ACE and MkIV data show an almost constant relative abundance of OC^{34}S with a small fractionation in the stratosphere. This confirms that OCS is a major contributor to the background SSA because the observed OCS fractionation is simillar to that measured in SSA. ACE and MkIV data also show an increasing enrichment of O^{13}CS with increasing altitude consistent with absorption cross sections measured in the laboratory. MkIV measurements show a reasonable agreement with ACE data within error bars.

Data availability

The ACE-FTS freely available at `https://ace.uwaterloo.ca` after registration.

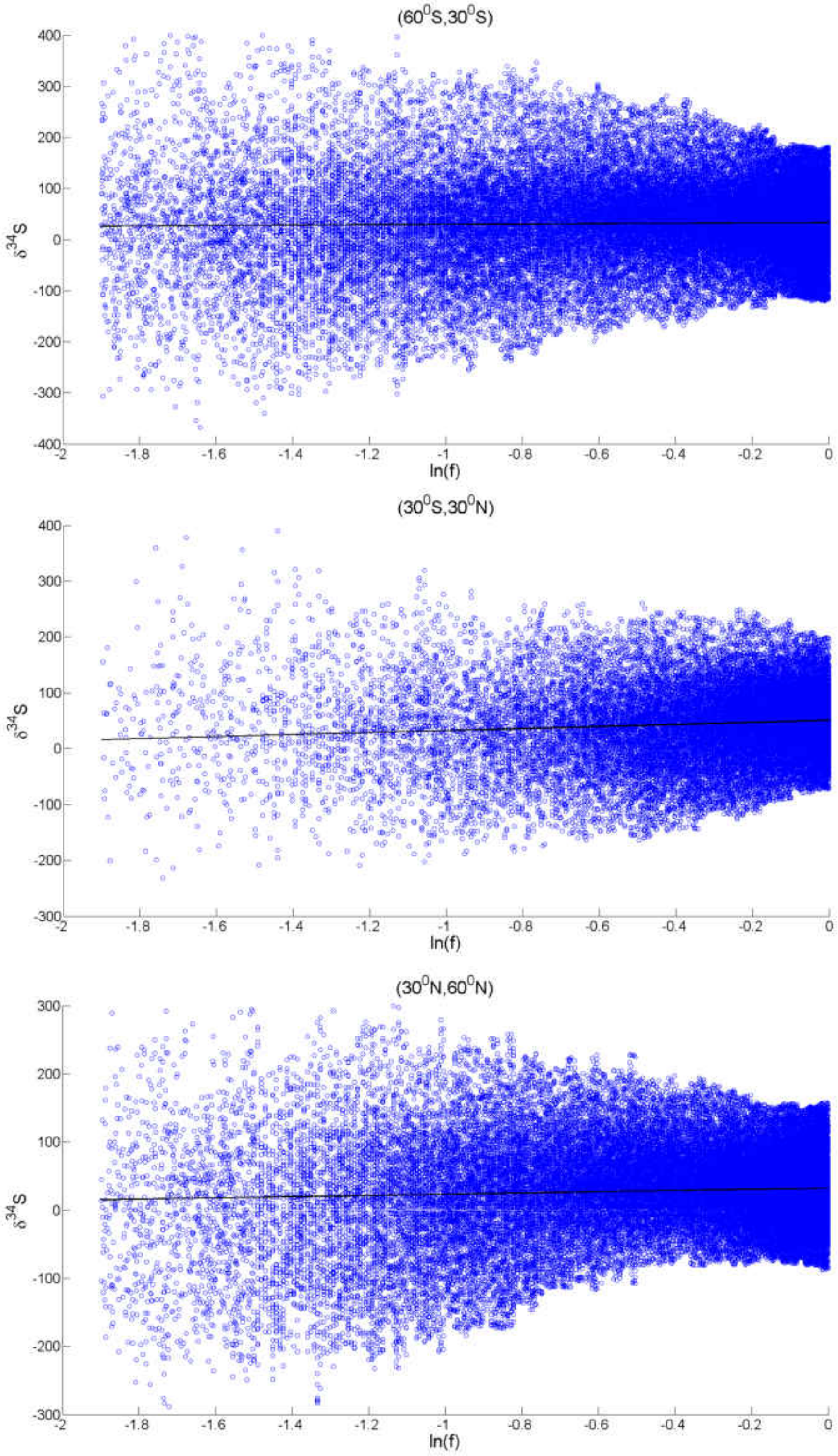

FIG. 34: ^{34}S abundance for stratospheric OCS as function of the unreacted fraction grouped in 3 latitude bins of 60° S – 30° S, 30° S – 30° N, 30° N – 60° N.

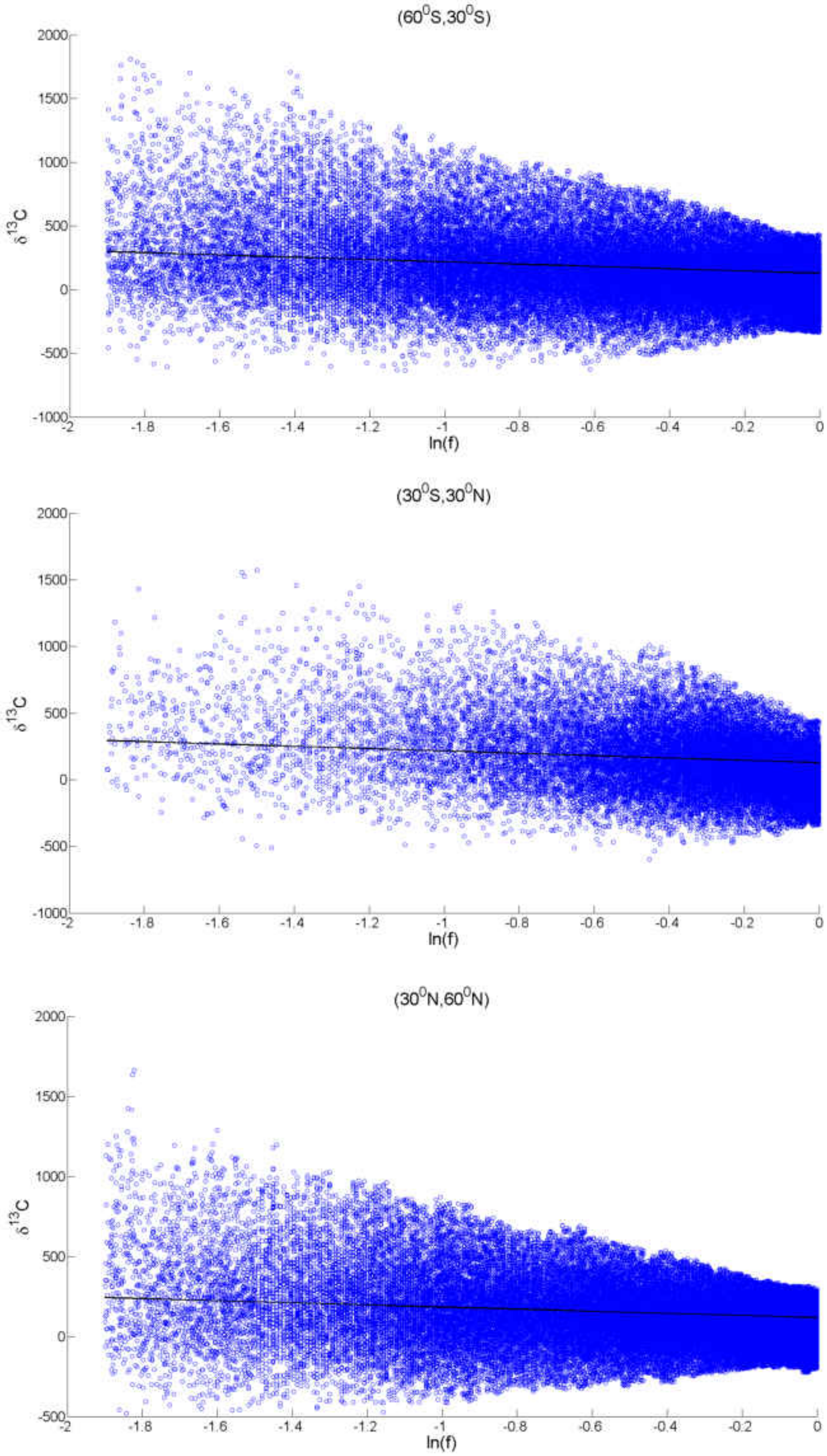

FIG. 35: ^{13}C abundance in stratospheric OCS as function of the unreacted fraction grouped in 3 latitude bins of 60° S – 30° S, 30° S – 30° N, 30° N – 60° N.

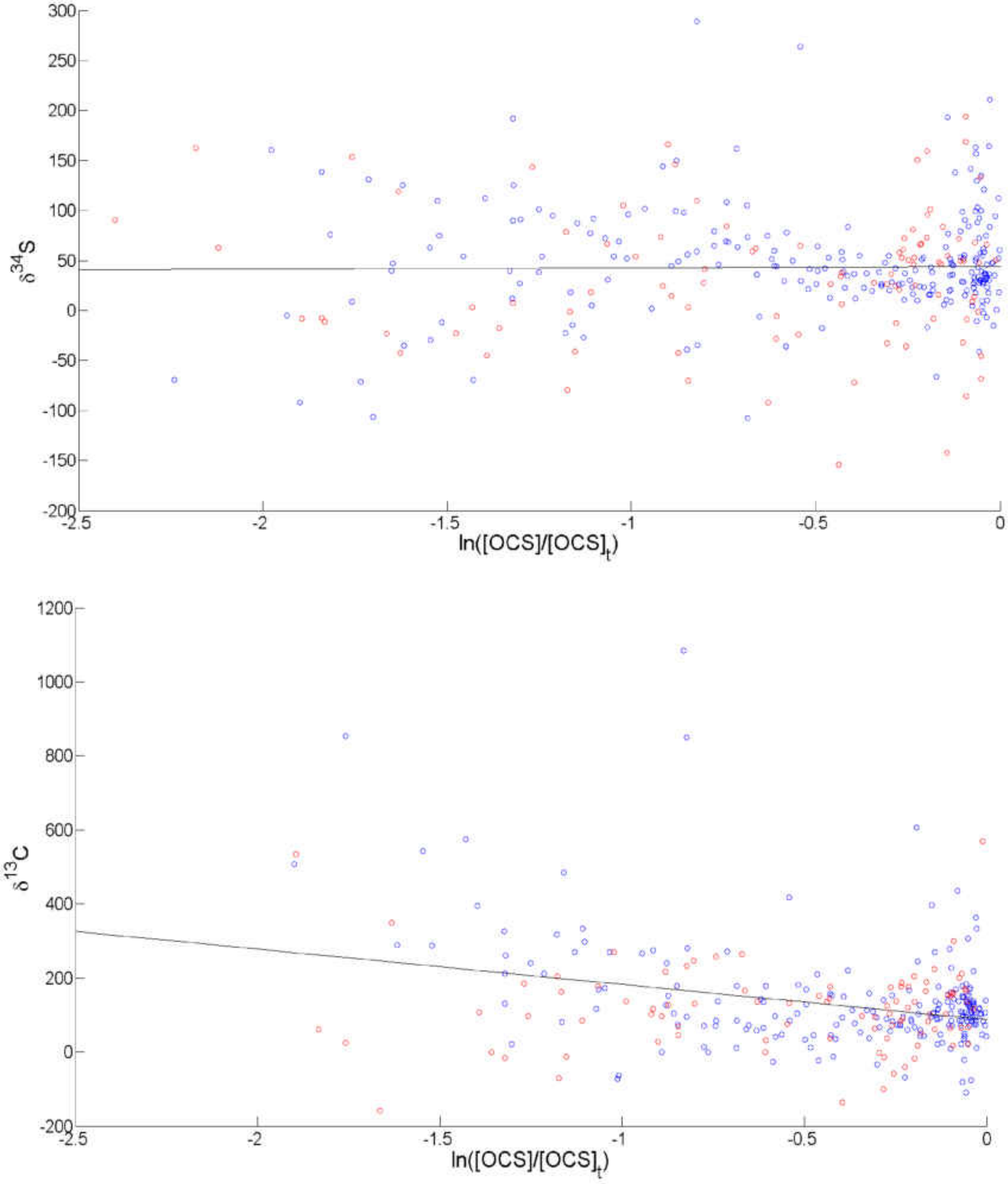

FIG. 36: OC^{34}S fractionation versus ln(f) (top) and O^{13}CS fractionation versus ln(f) (bottom) plotted using MkIV data, obtained in the 35° N (blue) and 65° N (red).

CHAPTER 6

LINE LISTS FOR AlF AND AlCl IN THE $X^1\Sigma^+$ GROUND STATE

The majority of the material and results in this paper are published in the Astrophysical Journal Supplement Series ([79]). This study was supervised by Peter F.Bernath (co-author). As the first author, all the computational calculations, preparing the figures, tables, and writing the paper were done by me.

Introduction

AlF and AlCl are members of the aluminum monohalide family AlX (X=F,Cl,Br,I) and can be produced in the gas phase by heating $AlCl_3$ or AlF_3 mixed with Al to high temperatures [80]. AlCl also has been detected in a fast flow reactor from the reaction of Al with Cl_2 [81]. The $A^1\Pi$-$X^1\Sigma^+$ ultraviolet transition of AlCl has been observed in plumes produced by solid-fuel rockets [82].

AlF and AlCl have astronomical importance. The rotational lines of AlF and AlCl have been detected in the circumstellar envelopes of carbon-rich stars such as IRC+10216 [83, 84, 85]. The major source of heavy elements in the interstellar medium is mass loss from stellar winds associated with circumstellar shells of evolved stars. Understanding the physical and chemical process in circumstellar envelopes helps our understanding of chemical abundances in the interstellar medium [86].

The existence of AlF and AlCl was predicted in C-rich and O-rich stellar atmospheres in thermal equilibrium calculations by Tsuji [87]. Although Tsuji [87] did not consider condensation to form solids, he suggested that the lower temperature (∼1000 K) calculations might apply to circumstellar envelopes. Detection of AlF and AlCl transitions by IRAM 30 m radio telescope [83] and the CSO telescope [84] supported Tsuji's suggestion [83]. In a detailed study, Agúndez et al. [85] measured the molecular abundance of AlF and AlCl in the inner circumstellar layers of IRC+10216 and reported 1×10^{-8} and 7×10^{-8} relative abundances with respect to H_2 for AlF and AlCl, respectively. Agúndez et al. [85] also found surprisingly high abundances in the cold outer shell of IRC+10216. Highberger et al. [88] detected rotational transitions of AlF in the circumstellar envelope of CRL 2688, which is in a proto-planetary nebulae phase.

AlCl has also been observed in O-rich asymptotic giant branch (AGB) stars. Decin et al. [89] reported the observation of AlCl in the circumstellar envelope of the red AGB stars R Dor and IK Tau in an attempt to identify Al-bearing species using the ALMA sub-millimeter telescope array.

There is also a possibility of detecting AlF and AlCl in the Sun's photosphere. Asplund et al. [90] estimated the solar abundance of the elements and reported the abundances of 1.73×10^{-6}, 3.16×10^{-7} and 3.63×10^{-8}, respectively, for Al, Cl and F relative to H that makes the detection of AlF and AlCl possible in the Sun. Lodders et al. [91] predicted the formation of AlF and AlCl in L and T type brown dwarfs below 2500 K.

Quantitative laboratory data are required to simulate the spectral energy distributions of astronomical objects [92]. A reliable line list to calculate molecular opacities can be obtained through a combination of laboratory data and *ab initio* calculations. Mahieu et al. [93] measured a high resolution electronic spectrum of the $A^1\Pi$-$X^1\Sigma^+$ transition of AlCl. Hedderich et al. [80] reported on a high resolution spectra of $Al^{35}Cl$ and $Al^{37}Cl$ up to v=8 and J=167. Wyse et al. [94] measured rotational transitions of $Al^{35}Cl$ and $Al^{37}Cl$ in the millimeter region, and Hensel et al. [95] measured microwave lines in a jet expansion.

Hedderich et al. [96] provided a high resolution infrared spectrum of AlF with more than 500 ro-vibrational lines from bands with v=1→ 0 to v=5→ 4. Later Zhang et al. [97] extended the AlF ro-vibrational lines to higher J and v in order to obtain improved Dunham coefficients and an internuclear potential. Horiai et al. [98] measured a ro-vibrational spectrum of the overtone band (Δv=2) transitions of AlF between 1490 and 1586 cm^{-1} at high temperature with a diode laser spectrometer. Hoeft et al. [99] used rotational transitions of AlF in the microwave region to determine Dunham coefficients.

Some other theoretical and experimental studies have been conducted in order to obtain dipole moments and dipole moment functions. Lide1 et al. [100] studied the microwave transitions of gaseous AlF and AlCl at high temperature using a Stark spectrometer and determined the vibrationally averaged dipole moment for v=0 of AlF to be 1.53± 0.1 debye (D); however he did not report an AlCl dipole moment. Klein et al. [19] calculated a dipole of μ = 1.56 D in the v=0 vibrational level of AlF using the SCEP/CEPA method. Finally Wan et al. [101] computed the value of μ_e=1.3087 D as the permanent dipole moment for the $X^1\Sigma^+$ electronic state of AlCl at the equilibrium internuclear separation.

In this study we provide line lists for the ro-vibrational transitions of AlF and AlCl in their ground electronic states up to v=11 and J_{max}=200. Additionally, new *ab initio* dipole moment functions (DMFs) are computed for the $X^1\Sigma^+$ states of AlF and AlCl to provide line intensities.

Methods

Experimental data

1100 high resolution ro-vibrational and rotational lines of AlF from Zhang et al. [97] and 1544 lines of $Al^{35}Cl$ and $Al^{37}Cl$ in the microwave and infrared regions from Hedderich et al. [80] were used for the Ptential Energy Surface(PES) fitting. The observed lines of AlF are from v= 0 to v= 9, and J up to 101. The observed lines of $Al^{35}Cl$ are from v=0 to v=8 with a maximum J of 167 and v=0 to v=5, J_{max}=127 for $Al^{37}Cl$.

Dipole moment function calculations

Ab initio calculation have been performed using the Molpro 2012 package [102]. The aug-cc-pwCV5Z basis set was used for DMF calculations. The active space includes (6 a_1, $3b_1$, $3b_2$ and 0 a_2) orbitals in the C_{2v} point group symmetry for both AlF and AlCl *ab initio* calculations. The calculations were performed using the average coupled-pair functional (ACPF) [103, 104] method. The wavefunction utilized for ACPF calculations were obtained by state-averaged CASSCF calculations. The dipole moment was calculated from 1.27 Å to 2.11 Å for AlF and from 1.77 Å to 2.61 Å for AlCl in 0.02 Å increments. The dipole moment points were calculated as an expectation value $< \psi|\mu(r)|\psi >$ at a particular internuclear separation r.

Potential energy surface (PES) and ro-vibrational energy levels

Potential energy surfaces of AlF and AlCl were obtained by direct fitting of, respectively, 1100 and 1544 observed rotational and ro-vibrational frequencies of AlF and AlCl [105]. Initially, Le Roy's RKR program [106] provided semi-classical turning points of the potential energy functions based on the Rydberg-Klein-Rees (RKR) procedure using experimentally determined rotational B_v and vibrational G_v constants. The RKR program generated turning points up to v=10. Figures of the RKR potential energy surfaces for the ground states of AlF and AlCl, including the *ab initio* potential surfaces and dipole moment points, for the $X^1\Sigma^+$ electronic state of AlF and AlCl are presented in Figure 37 and Figure 38, respectively. The RKR potentials have been used in Le Roy's Betafit program [107] to generate trial values of β_i for the Expanded Morse Oscillator (EMO) potential function using equations 76-78.

$$V_{\mathrm{EMO}}(r) = D_e[1 - e^{-\beta(r)(r-r_e)}]^2 \tag{76}$$

$$\beta(r) = \beta_{\mathrm{EMO}}(y_q^{ref}(r)) = \sum_{i=0}^{N_\beta} \beta_i y_q^{ref}(r)^i \tag{77}$$

$$y_q^{ref}(r) = \frac{r^q - r_{ref}^q}{r^q + r_{ref}^q} \tag{78}$$

The EMO potential was chosen for the fit because it requires a small number of adjustable parameters and extrapolates well [108]. The dissociation energies of D_e=55564 cm^{-1} and D_e=41653 cm^{-1}, respectively, for AlF and AlCl are taken from the literature [80] and are fixed in the fitting process. Le Roy's DPotfit program [105] was used to determine the empirical EMO potentials by least squares fitting of the lines. Additionally, Born-Openheimer breakdown (BOB) corrections were included in the fit for AlCl to account for mass dependent corrections for AlCl isotopologues. A detailed description of the Schrödinger equation including the BOB adiabatic and non-adiabatic terms is available in Le Roy [109] and Le Roy [110]. The resulting parameters determined from DPotfit are r_e, β_i and BOB correction terms (u_i) with the corresponding fitting uncertainty for AlF and AlCl (Table 5).

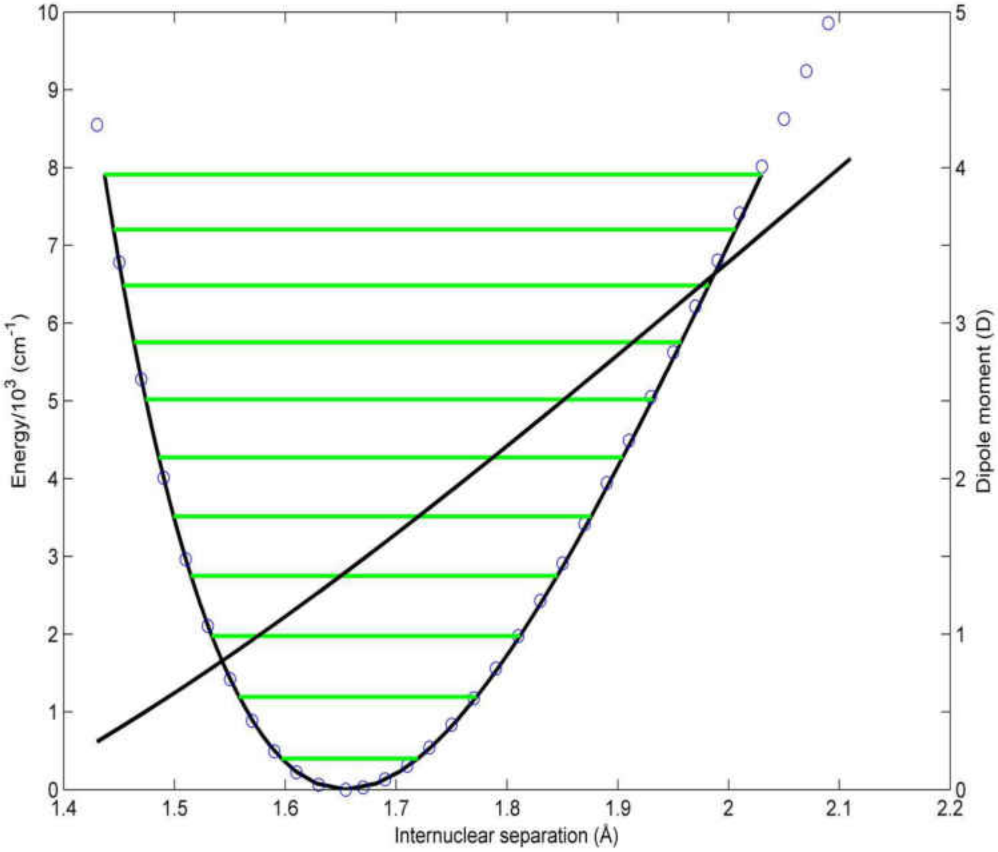

FIG. 37: Potential energy surface of AlF calculated by RKR (—), PES from *ab initio* calculation (∘) and DMF (—)

TABLE 5: Fitting parameters of the empirical EMO potentials for AlF and AlCl

Constants	AlF	AlCl
β_0	1.2998170(34)	1.121878(31)
β_1	-0.591067(47)	-0.439891(88)
β_2	0.16823(43)	0.090230(54)
β_3	0.1256(48)	0.2068(75)
β_4	0.236(18)	-0.1030(36)
u_0^{Cl}	-	**[0.00]**

Continued on next page

TABLE 5 – continued from previous page

Constants	AlF	AlCl
u_1^{Cl}	-	11.00(45)
u_2^{Cl}	-	-43(7.5)
u_∞^{Cl}	-	**[0.00]** [a]
r_e / Å	1.654368(10)	2.1301672(50)
$D_e\times10^{-4}$ / cm^{-1}	[5.556402471] [a]	[4.1653105] [a]
$\sigma_{r.m.s.}$	0.719382	0.710634

[a] Values in squared brackets have been fixed during fitting.

TABLE 6: Dipole moment functions for the $X^1\Sigma^+$ states of AlF and AlCl in debye

r / Å	AlF	AlCl
1.61	-1.171865525	—
1.65	-1.406679365	—
1.75	-1.93753402	—
1.85	-2.52118433	0.12302058
1.95	-3.125333165	-0.46020142
2.05	-3.742664015	-1.07884535
2.09	-3.991691835	-1.3341922
2.13	—	-1.59415822
2.17	—	-1.85543219
2.21	—	-2.12031688

Dipole moment function evaluation

The point-wise *ab initio* DMFs were calculated for AlF and AlCl using the ACPF method as described in section 6. The DMF points are provided in Table 6 for AlF and AlCl. The calculated equilibrium dipole moment values at bond lengths r_e=1.6543682 and r_e=2.130143 are μ_e=1.406679 and μ_e=1.59415 D ,respectively, for AlF and AlCl.

To evaluate our DMF values, comparisons are made with values in the literature obtained from theory and experiment. Lidel et al. [100] measured the microwave

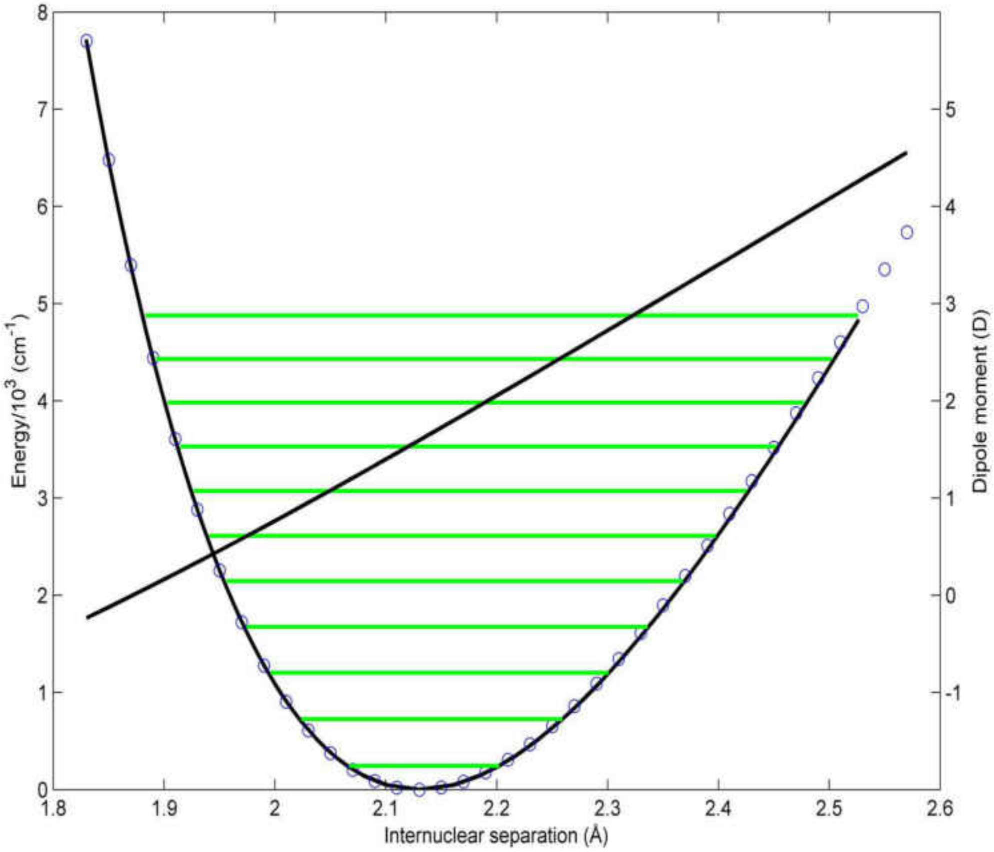

FIG. 38: Potential energy surface of AlCl calculated by RKR (—), PES from *ab initio* calculation (○) and DMF (—)

transitions of AlF and AlCl and obtained the value of μ_0=1.53± 0.1 D for the dipole moment of AlF. Later Klein et al. [19] reported μ_0=1.65 D as the vibrationally averaged dipole moment for the v=0 of AlF using the coupled electron pair approximation (CEPA) and self consistent electron pair approach (SCEP) methods. Wan et al. [101] reported μ_0=1.3087 D at equilibrium for the $X^1\Sigma^+$ state of AlCl.

Some of the vibrational transition dipole moment matrix elements (TDMMEs) for AlF from our calculation ($R_{v''}^{v'}$) are listed in Table 7. From this study (Table 7) the dipole moment for v=0 is 1.44 D that agrees with the value of μ_0=1.53± 0.1 D derived by Lidel et al. [100]. As for AlF, we list some of the vibrational TDMMEs of $Al^{35}Cl$ and $Al^{37}Cl$ in Table 8 and Table 9 respectively. The near linear form of the AlF and AlCl DMFs and the large first derivative (Figures 37 and 38) lead to the noticeable decrease in TDMMEs from fundamental transitions to the overtone transitions (see Tables 7, 8 and 9).

TABLE 7: Calculated band transition dipole matrix elements $\mathrm{R}_{v''}^{v'}$ for the $X^1\Sigma^+$ state of AlF in D

v''	R_v^v	R_v^{v+1}	R_v^{v+2}	R_v^{v+3}	R_v^{v+4}	R_v^{v+5}
0	-1.43973	-0.235256	0.00898308	-0.0004441	3.31139E-05	-3.41133E-06
1	-1.50612	-0.335131	0.015849	-0.000905842	4.11727E-05	1.17658E-05
2	-1.57317	-0.413355	0.0227721	-0.00145677	6.67869E-05	9.75234E-06
3	-1.64089	-0.480586	0.0298703	-0.00212859	0.000111178	1.96783E-05
4	-1.70926	-0.540946	0.0371621	-0.00289252	0.000160964	0.000028645
5	-1.77826	-0.596479	0.0446437	-0.00376267	0.000228425	2.33072E-05
6	-1.84789	-0.648419	0.0523238	-0.00475932	0.000301221	2.76505E-05
7	-1.91812	-0.697573	0.0601758	-0.00586917	0.000401331	-
8	-1.98898	-0.744474	0.0682134	-0.00708091	-	-
9	-2.06044	-0.789498	0.0764442	-	-	-
10	-2.13247	-0.832954	-	-	-	-

TABLE 8: Calculated band transition dipole matrix elements $\mathrm{R}_{v''}^{v'}$ for the $X^1\Sigma^+$ state of $Al^{35}Cl$ in D

v''	R_v^v	R_v^{v+1}	R_v^{v+2}	R_v^{v+3}	R_v^{v+4}	R_v^{v+5}
0	-1.63011	-0.313273	0.0127291	-0.00066763	0.000027866	2.19962E-06
1	-1.7019	-0.444323	0.022221	-0.00135854	0.0000653217	4.94029E-06
2	-1.77398	-0.545726	0.0316667	-0.00218464	0.000119029	8.15688E-06
3	-1.84635	-0.631896	0.0411892	-0.00314095	0.000190878	1.12346E-05
4	-1.91901	-0.708389	0.050818	-0.00422295	0.000282796	1.41833E-05
5	-1.99193	-0.778046	0.0605625	-0.0054265	0.000396645	1.63401E-05
6	-2.06513	-0.842545	0.0704256	-0.00674889	0.000534418	1.70656E-05
7	-2.1386	-0.902974	0.0804076	-0.00818799	0.000697583	-
8	-2.21232	-0.960085	0.0905075	-0.00974247	-	-
9	-2.2863	-1.01442	0.100723	-	-	-
10	-2.36053	-1.0664	-	-	-	-

TABLE 9: Calculated band transition dipole matrix elements $R_{v''}^{v'}$ for the $X^1\Sigma^+$ state of $Al^{37}Cl$ in D

v''	R_v^v	R_v^{v+1}	R_v^{v+2}	R_v^{v+3}	R_v^{v+4}	R_v^{v+5}
0	-1.62967	-0.311403	0.0125765	-0.000655516	2.71686E-05	2.14306E-06
1	-1.70061	-0.441656	0.0219525	-0.00133363	6.36417E-05	4.82234E-06
2	-1.77183	-0.542434	0.0312815	-0.00214419	0.000115906	7.99155E-06
3	-1.84333	-0.628064	0.0406849	-0.00308225	0.000185795	1.10357E-05
4	-1.91511	-0.704074	0.0501919	-0.00414334	0.00027515	0.000013986
5	-1.98716	-0.773287	0.0598119	-0.00532338	0.000385779	1.62065E-05
6	-2.05947	-0.83737	0.0695477	-0.00661968	0.000519618	1.71048E-05
7	-2.13205	-0.897406	0.0794	-0.00803011	0.000678101	-
8	-2.20488	-0.954143	0.0893676	-0.00955335	-	-
9	-2.27795	-1.00812	0.0994486	-	-	-
10	-2.35128	-1.05975	-	-	-	-

The equilibrium spectroscopic constants for AlF and AlCl were calculated using the potential energy surfaces obtained from *ab initio* calculations. The calculated constants from this study along with available constants in the literature obtained from experiment and theory are presented in Table 10 for AlF and AlCl. By comparison with the experimentally derived equilibrium constants of AlF, the relative error of calculated constants $\delta X/X$ with X=(r_e, ω_e, B_e, $\omega_e x_e$ and α_e) are respectively 0.04 %, 0.50 %, 0.09 %, 2.60 % and 0.98 % with respect to the experimentally measured equilibrium constants. The relative errors with respect to the experiment for the same constants for AlCl are 0.08 %, 0.08 %, 0.62 %, 1.52 % and 0.84 %. Overall there is a good agreement between calculated constant from this study, those listed in Table 10 and experimental values. In general there is an improvement in the calculated equilibrium constants compared to other theoretical studies.

TABLE 10: Spectroscopic parameters for the $X^1\Sigma^+$ states of AlF and AlCl molecules

Molecule		r_e /Å	B_e /cm^{-1}	α_e /cm^{-1}	ω_e /cm^{-1}	$\omega_e x_e$ /cm^{-1}	μ_e /D
AlF	This work	1.6536	0.552987	0.004935353	806.3542	4.72365	1.40668
	Reference (calc) [19]	1.664	0.546	0.005	805	4.3	1.543
	Expt. [96]	1.6543682	0.552480208	0.0049842	802.32	4.849	-
AlCl	This work	2.1283	0.2441156	0.0015974	484.8065	2.06968	1.59415
	Reference (calc) [101]	2.1374	0.2408	-	478.13	-	1.30866
	Reference (calc) [112]	2.146	-	-	467	-	-
	Reference (calc) [113]	2.140	0.2418	-	484.5	-	-
	Expt. [80]	2.13014336	0.24390066	0.001611082	481.7765	2.10181	-

Line list

The PES from Le Roy's DPotfit program with the *ab initio* DMFs have been used in Le Roy's LEVEL program [111]. LEVEL generates ro-vibrational energy levels by solving a one dimensional Schrödinger equation and provides vibrational transition matrix elements $<\psi_{v'J'}|\mu(r)|\psi_{v''J''}>$ that depend on J and therefore account for the Herman-Wallis effect [114]. Additionally LEVEL calculates Einstein A coefficients in s^{-1} units by [18]:

$$A_{J'\to J''} = \frac{16\pi^2\nu^3 S^{\Delta J}_{J''}}{3\varepsilon_0 hc^3(J'+1)}|\langle\psi_{v',J'}|\mu(r)|\psi_{v'',J''}\rangle|^2 \tag{79}$$

where ν is the frequency, $S^{\Delta J}_{J''}$ is the Hönl-London factor and $\mu(r)$ is the DMF. The oscillator strengths $f_{J'\leftarrow J''}$, have been calculated from Einstein A coefficients by [18]:

$$f_{J'\leftarrow J''} = 1.4991938\frac{1}{\tilde{\nu}^2}\frac{(2J'+1)}{(2J''+1)}A_{J'\to J''} \tag{80}$$

where $\tilde{\nu}$ is the transition wavenumber in cm^{-1}.

We present a line list of AlF, Al^{35}Cl and Al^{37}Cl in their ground states. The line lists for AlF, Al^{35}Cl and Al^{37}Cl are calculated up to v=11 and J=200 and a sample is provided in Table 11. The line list calculations with transitions up to Δv=5 were included for AlF and AlCl. We note that for Δv>5 the calculated band intensities no longer decrease as expected [115] and are therefore excluded.

A summary of entire computational method, starting from Dunham coefficients for calculation of PEC to the production of linelist and the intermediate processes which are discussed in this chapter, is presented in the Figure 39.

TABLE 11: A sample of the line lists of AlF, $Al^{35}Cl$ and $Al^{37}Cl$ in the $X^1\Sigma^+$ state

Isotopologue	Branch(J'')	v'	v''	$E_{v'',J''}$ / cm^{-1}	$\tilde{\nu}$ / cm^{-1}	$A_{J'\rightarrow J''}$ / s^{-1}	$f_{J'\leftarrow J''}$	TDMMEs/D
AlF	R(30)	0	0	910.72614	33.9747	0.0128331	1.72143E-05	-1.4562
AlF	R(30)	1	0	910.72614	821.75425	4.65744	1.0679E-05	-0.233211
AlF	P(35)	1	0	1091.46653	748.48055	3.86434	1.00499E-05	-0.240689
AlF	R(30)	1	1	1698.81235	33.66805	0.0136604	1.86593E-05	-1.52298
AlF	R(30)	2	1	1698.81235	811.95803	9.10694	2.13882E-05	-0.332028
AlF	P(35)	2	1	1877.92073	739.34407	7.56665	2.01678E-05	-0.343061
AlF	R(30)	3	2	2477.40681	802.27935	13.3499	3.21141E-05	-0.409297
AlF	P(35)	3	2	2654.89475	730.32055	11.1077	3.03421E-05	-0.423381
$Al^{35}Cl$	R(30)	0	0	466.34315	15.044	0.00141992	9.71417E-06	-1.6439
$Al^{35}Cl$	R(30)	1	0	466.34315	491.04991	1.77495	1.13973E-05	-0.311668
$Al^{35}Cl$	P(35)	1	0	546.39396	458.71304	1.54233	1.06793E-05	-0.316932
$Al^{35}Cl$	R(30)	1	1	942.4483	14.94475	0.00151654	1.05134E-05	-1.71586
$Al^{35}Cl$	R(30)	2	1	942.4483	486.8156	3.47679	2.27153E-05	-0.441907
$Al^{35}Cl$	P(35)	2	1	1021.9708	454.69188	3.02373	2.13087E-05	-0.449661
$Al^{35}Cl$	R(30)	3	2	1414.41783	482.62055	5.10716	3.39497E-05	-0.542587
$Al^{35}Cl$	P(35)	3	2	1493.41525	450.70873	4.4455	3.18843E-05	-0.552466
$Al^{37}Cl$	R(30)	0	0	458.2026	14.69132	0.00132114	9.47754E-06	-1.64313
$Al^{37}Cl$	R(30)	1	0	458.2026	485.15124	1.69151	1.11273E-05	-0.30982
$Al^{37}Cl$	P(35)	1	0	536.37728	453.5759	1.47282	1.04303E-05	-0.314984
$Al^{37}Cl$	R(30)	1	1	928.7583	14.59555	0.00141002	1.02483E-05	-1.71423
$Al^{37}Cl$	R(30)	2	1	928.7583	481.0168	3.3142	2.21782E-05	-0.439276
$Al^{37}Cl$	P(35)	2	1	1006.42323	449.64712	2.88814	2.08124E-05	-0.44688
$Al^{37}Cl$	R(30)	3	2	1395.27478	476.92024	4.86958	3.31489E-05	-0.539343
$Al^{37}Cl$	P(35)	3	2	1472.4329	445.75504	4.24716	3.11426E-05	-0.549028

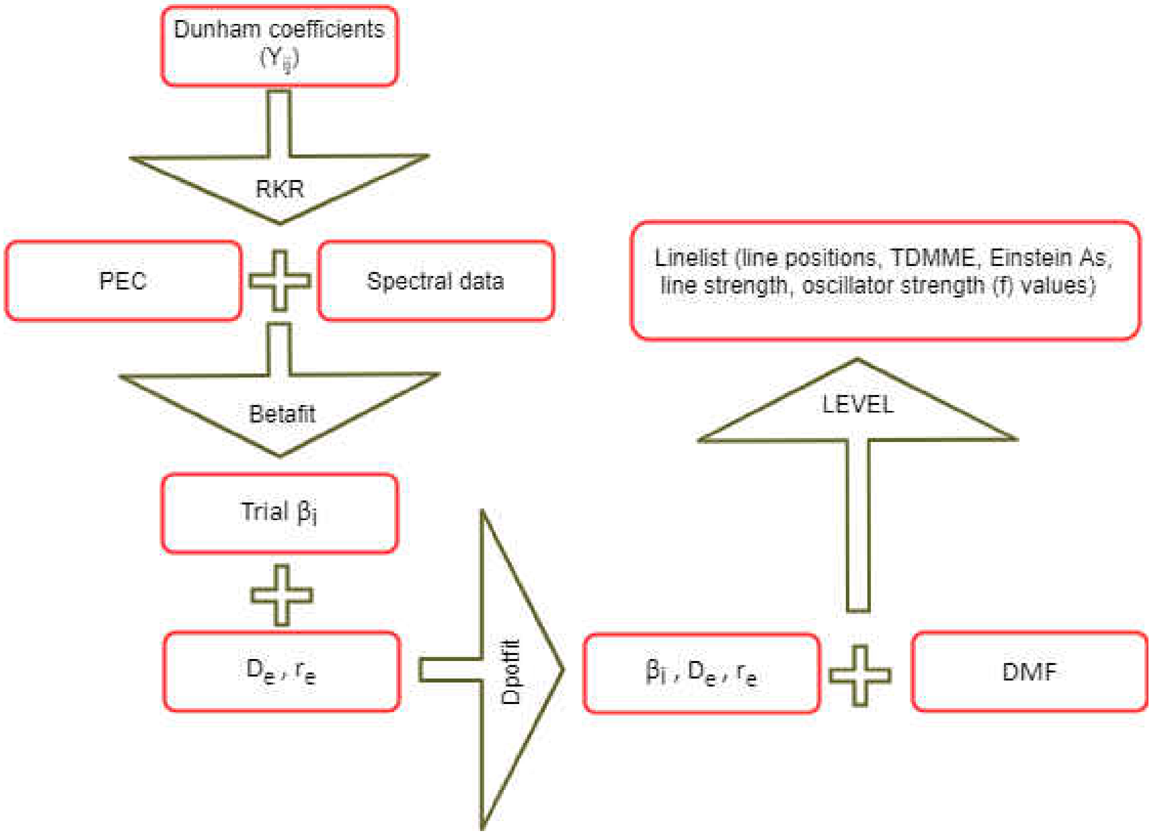

FIG. 39: Overall method for the production of the linelist for AlF and AlCl

Partition function

The partition functions have been calculated for AlF, $Al^{35}Cl$ and $Al^{37}Cl$ with vibrational levels up to the dissociation limit including **quasibound** levels by

$$Q = \sum_{v=0}^{v_{max}} \left(\sum_{J=0}^{J_{max}} (2J+1) e^{-E_{v,J}/kT} \right). \tag{81}$$

The partition functions have been calculated for temperatures up to T=3000 K with 75 K increments up to 1000 K and increasing by 250 K increments up to 3000 K, including temperatures available in the JPL database [116]. As a check, the partition functions for v=0 were calculated and included for comparison purposes with the available partition functions in the JPL database. Partition functions including those from the JPL database are presented in Table 12 for AlF, $Al^{37}Cl$ and $Al^{35}Cl$. The calculated partition functions from our study agree well with those in the JPL database. Polynomial fits of the partition functions of AlF, $Al^{37}Cl$ and $Al^{35}Cl$ have been performed using the following expression and the determined a_n coefficients are provided in Table 13 :

$$\log_{10} Q = \sum_{n=0}^{n_{max}} a_n (\log_{10} T)^n \tag{82}$$

TABLE 12: Partition functions for AlF and AlCl isotopologues in the $X^1\Sigma^+$ state

T(K)	AlF	AlF	AlF	$Al^{35}Cl$	$Al^{35}Cl$	$Al^{35}Cl$	$Al^{37}Cl$	$Al^{37}Cl$	$Al^{37}Cl$
9.375	73.121[a]	73.121[b]	73.121[c]	651.305[a]	651.313[b]	651.312[c]	666.782[a]	666.7812[b]	666.784[c]
18.75	144.197	144.197	144.197	1294.595	1294.603	1294.605	1325.547	1325.547	1325.553
37.5	286.394	286.394	286.395	2581.433	2581.441	2581.450	2643.340	2643.340	2643.353
75	570.878	570.878	570.881	5156.529	5155.992	5156.014	5280.443	5279.821	5279.848
150	1140.736	1140.162	1140.167	10415.973	10308.525	10308.574	10672.472	10556.298	10556.350
225	1720.786	1709.861	1709.868	16237.658	15465.635	15465.709	16658.336	15837.462	15837.536
300	2341.067	2279.975	2279.982	22973.382	20627.343	20627.220	23598.714	21123.334	21123.137
375	2995.161	-	-	30765.028	-	-	31636.892	-	-
425	3470.974	-	-	36576.162	-	-	37635.798	-	-
500	4241.029	-	-	46240.958	-	-	47617.523	-	-
575	5082.399	-	-	57060.518	-	-	58796.526	-	-
650	5997.727	-	-	69048.751	-	-	71186.951	-	-
725	6988.727	-	-	82216.802	-	-	84800.200	-	-
800	8056.609	-	-	96574.498	-	-	99646.370	-	-
875	9202.296	-	-	112131.018	-	-	115734.917	-	-
925	10009.692	-	-	123172.426	-	-	127155.347	-	-
1000	11286.688	-	-	140746.595	-	-	145334.771	-	-
1250	16121.530	-	-	208202.814	-	-	215130.344	-	-
1500	21860.979	-	-	289563.110	-	-	299333.846	-	-
1750	28523.818	-	-	385161.775	-	-	398291.300	-	-
2000	36128.794	-	-	495347.356	-	-	512363.320	-	-
2250	44695.105	-	-	620483.981	-	-	641926.102	-	-
2500	54242.599	-	-	760950.631	-	-	787370.039	-	-
2750	64791.894	-	-	917138.157	-	-	949095.786	-	-
3000	76364.465	-	-	1089444.116	-	-	1127507.992	-	-

[a] Calculated partition function including quasibound levels

[b] Calculated partition function for v=0 vibrational level

[c] Calculated partition function from JPL database

TABLE 13: Polynomial coefficients determined from regression of equation 82

Polynomial coefficient	AlF	$Al^{35}Cl$	$Al^{37}Cl$
a_0	0.4854277	4.1929305	4.2530758
a_1	2.9113006	-6.4086498	-6.5837492
a_2	-3.3592917	9.1230438	9.3668437
a_3	2.8840883	-5.5849132	-5.7569906
a_4	-1.2934446	1.7766208	1.8414362
a_5	0.2877944	-0.2764733	-0.2888155
a_6	-0.0246505	0.016656	0.0175889

Conclusions

EMO empirical potentials for AlF, $\mathrm{Al^{35}Cl}$ and $\mathrm{Al^{37}Cl}$ have been determined by direct potential fitting using observed vibrational and rotational transitions. Additionally, *ab initio* DMF calculations were performed for AlF and AlCl. Line lists of AlF, $\mathrm{Al^{35}Cl}$ and $\mathrm{Al^{37}Cl}$ in their $\mathrm{X}^1\Sigma^+$ ground state have been calculated using *ab initio* DMF and the fitted potential. The line lists can be used to compute molecular opacities for AlF and AlCl.

CHAPTER 7

A NEW LINE LIST FOR THE $A^2\Sigma^+-X^2\Pi$ ELECTRONIC TRANSITION OF OH

The majority of material and results used in this chapter is published in the Journal of Quantitative Spectroscopy & Radiative Transfer ([117]). Thomas Masseron (co-author) calculated the synthetic solar spectrum and stellar spectrum (HD196944) using the linelist provided by us (Figures 44 and 45). The software program for the conversion of transition dipole moment matrix elements from Hund's case (a) to Hund's case (b) is written by James Hodges (co-author). This study was supervised by Peter F. Bernath (co-author). As the first author, the computational calculations to prepare a linelist, preparation of figures and tables, and writing the paper were done by me.

Introduction

The hydroxyl radical (OH) plays an important role in atmospheric science, astronomy and combustion. OH is one of the major oxidizers in atmosphere [118] and removes toxic organic compounds in the troposphere due to its high reactivity [119, 120]. It is also present in stellar atmospheres [121] including the Sun [122], in interstellar clouds [123] and in planetary atmospheres [124]. OH $X^2\Pi$ vibration-rotation transitions are a source of nighttime airglow and are known as the Meinel bands [125, 126]. Meinel bands and pure rotational lines can be used to determine the oxygen abundance in the Sun [127, 128] and other stars. OH is also seen in flames [129] and in other combustion-related processes.

There is extensive literature on OH spectroscopy. Here we summarize some of the more relevant papers but do not provide an exhaustive survey. Coxon [130] used OH A−X line positions measured with grating spectrographs by Engleman [131], Dieke and Crosswhite [132] and others in his least-squares fit of 1618 $A^2\Sigma^+ - X^2\Pi$, 774 $X^2\Pi$ ro-vibrational [133] and 125 microwave frequencies to determine the spectroscopic constants for the $A^2\Sigma^+$ (v=$0-3$) and $X^2\Pi$ (v=$0-5$) states of OH. Later, Coxon et al. [134] obtained additional molecular constants for the $X^2\Pi$ (v$=8, 12$), $A^2\Sigma^+$ (v$=4-9$), $B^2\Sigma^+$ (v$=0, 1$) and $C^2\Sigma^+$ (v$=0, 1$) states from the X−X, A−X, B−X, C−A and B−A systems measured with a grating spectrograph [135], a grating spectrometer [136] and laser spectroscopy [137, 138]. It should be noted that most of the lines used by Coxon have a precision of 0.03 cm^{-1} and accuracy of perhaps 0.05 cm^{-1}.

Stark et al. [139] measured a near-UV emission spectrum of the A−X transition of OH with a Fourier transform spectrometer using hollow-cathode discharge of 10 mTorr H_2O in 2.2 Torr of helium. Stark et al. [139] provided line positions for the $A^2\Sigma^+ - X^2\Pi$ (0,0), (1,1), (2,2) bands and derived a set of molecular constants. The majority of the line positions had an accuracy of about 0.002 cm^{-1} or better.

The OH A−X line positions in HITRAN 2016 database [140] are based on the analysis by Gillis et al. [141]. Gillis et al. [141] used (0,0), (1,1) and (2,2) bands from Stark et al. [139] but the line positions for the (3,2), (2,1) and (1,0) bands are based on Coxon [130] with an accuracy of 0.05 cm^{-1}. The line strengths and Einstein A values are based on work of Luque and Crosley as incorporated in the LIFBASE program [142].

LIFBASE line intensities are calculated using the transition dipole moment and transition probabilities of Luque and Crosley [143]. Although it is not stated in the LIFBASE program notes, the main source of the line positions seems to be the work of Coxon and co-workers. [130, 134, 136]

There have been extensive studies on the $X^2\Pi - X^2\Pi$ ground state transition (Meinel bands) of OH. Again, we only mention a few key publications on this topic. Abrams et al. [144] recorded the infrared emission spectrum of the Meinel bands (v=0−10) by Fourier transform spectroscopy of an O_3+H flame. Mélen et al. [145] analyzed microwave and infrared lines from the solar spectrum and laboratory measurements to obtain an improved set of molecular constants for the $X^2\Pi$ ground state. Goldman et al. [146] updated the line parameters for the $X^2\Pi - X^2\Pi$ (v′,v″) bands with $v' = 0 - 10$ and Δv$= 0 - 6$ up to $J_{max} = 49.5$. Bernath and Colin [147] used previously published laboratory data and additional lines taken from infrared solar spectra measured by the ACE FTS instrument on orbit [15] to update the molecular constants for the $X^2\Pi$ (v$=0-13$) and $B^2\Sigma^+$ (v$=0,1$) states of OH. The Meinel bands in HITRAN 2016 are based on Goldman et al. [128] for line intensities, and Bernath and Colin [147] for line positions. Brooke et al. [148] refitted the $X^2\Pi$ ground state of OH using the data of Bernath and Colin [147] and derived line intensities from a new *ab* initio DMF.

There have also been many studies on the line strengths of OH transition in addition to the publications cited above and again we cite only a few. Crosley and Lengel [149] measured relative transition probabilities in the A$-$X system of OH by using branching ratios from the emission of vibrational levels v$' = 0,1$ and 2 in the $A^2\Sigma^+$ state. Wang and Killinger [150] measured a band oscillator strength of f=1.13± 0.01× 10^{-3} for the (0,0) band by laser absorption spectroscopy. Later, Bauschlicher and Langoff [151] calculated the radiative lifetime of the $A^2\Sigma^+$ state by a very extensive *ab* initio calculation of the A$-$X transition dipole moment. Bittencourt et al. [152] used a back-propagation neural network to fit potential energy curves and *ab* initio transition dipole moment (TDM) points from the work of Bauschlicher and Langoff [151] and computed the A$-$X transition probabilities and radiation lifetimes for the $A^2\Sigma^+-X^2\Pi$ transition.

The currently accepted line positions and line intensities for the OH A$-$X transition in HITRAN and LIFBASE are dated. More accurate line position are now available and the methodology of Brooke et al. [148] can be applied to improve the line intensity calculations. Our goal is to provide a new A$-$X line list covering a broad range of vibrational and rotational levels for astronomical, atmospheric and combustion applications.

Method

Experimental data and spectral line fitting

The available observed spectral lines for the $A^2\Sigma^+-X^2\Pi$ transition of OH have been collected from various sources in the literature including (v$'$,v$''$) = $(0,0),(1,1),(2,2)$ bands from Stark et al. [139], the (3,2), (3,3), (4,2) bands from Coxon [130, 134] and the $(4,2)$ overtone transition in the excited $A^2\Sigma^+$ electronic state from Derro et al. [153]. The A state is predissociated [154], which limits the A−X observations. A summary of observed spectral lines including maximum rotational quantum numbers for each band is presented in Table 15. The last column in Table 15 is the maximum rotational level we calculate for the bands. The molecular constants for the X state of OH were taken from Brooke et al. [148]. The excited $A^2\Sigma^+$ state constants were determined using PGOPHER [156], but the ground $X^2\Pi$ state constants were already well determined and were kept fixed at the values of Brooke et al. [148]. To determine the molecular constants for the A state, we performed a weighted least-squares fit using PGOPHER, with some of the lines reweighted according to their uncertainty. The weighted standard deviation for the fit was 1.0008. The updated molecular constants for the A state are reported in Table 14. In this study, we used these constants for the A state up to v$'$=4 (Table 14) and for the X state for v$''$=0 − 9 from Brooke et al. [148] for our A−X line list.

TABLE 14: Molecular constants for the OH $A^2\Sigma^+$ state (in cm^{-1}).

	v=0	v=1	v=2	v=3	v=4
T_0	32420.914388(14)[a]	35409.51299(57)	38202.5785(17)	40796.1079(53)	43181.741(23)
B_v	16.9651348(23)	16.129520(23)	15.28676(18)	14.4223(10)	13.5165(10)
D_v	0.002064145(18)	0.00204754(23)	0.00205566(44)	0.00206463(36)	0.0021427(82)
H_v	1.26853(43)×10^{-7}	1.1239(79)×10^{-7}	1.48(26)×10^{-7}	...	...
L_v	-1.95182(30)×10^{-11}	-2.603(86)×10^{-11}	...	...	...
γ_v	0.2261003(94)	0.216934(91)	0.21296(72)	0.195955(59)	0.1864(47)
γ_D	-4.758(14)×10^{-5}	-4.464(33)×10^{-5}	-0.000179(13)	...	...
γ_H	4.30(20)×10^{-9}	...	...	...	...

[a] One standard deviation in the last digits quoted is given in parenthesis.

TABLE 15: Observed A−X lines of OH used in this study adopted from literature. The second column shows the existing bands. The third and fourth column are the maximum J value for the observed lines and in this study.

Observed lines	(v$'$,v$''$)	J_{max}	J_{max} (This study)
Stark et al. (1994) [139]	(0,0), (1,1), (2,2)	30.5, 22.5, 11.5	35.5, 27.5,18.5
Coxon (1980) and (1991) [130, 134]	(3,2), (3,3), (4,2)	19.5, 13.5, 12.5	25.5, 25.5,18.5
Derro et al. (2005) [153]	(4,2)[a]	7.5	12.5

[a] Overtone transition in the excited $A^2\Sigma^+$ state.

Transition dipole moment calculation

Molpro 2012 [155] was used to calculate the *ab initio* Transition Dipole Moment Function (TDMF) for the $A^2\Sigma^+ - X^2\Pi$ transition. The transition dipole moment points were calculated from 0.69 Å to 3.00 Å in increments of 0.02 Å. The long range part of the calculation is needed to obtain reliable line intensities for high vibrational levels and the close point spacing gives a more reliable interpolation in the LEVEL program (see below). The Multi-Reference Configuration Interaction (MRCI) method has been used with aug-cc-pwv5z basis functions [157], and core correlation was included. The active space includes $5a_1$, $2b_1$, $2b_2$, $1a_2$ orbitals in the C_{2v} point symmetry group used by Molpro. The wave functions utilized for MRCI calculations were obtained by a complete active space self-consistent field (CASSCF) calculation. The TDMF values were calculated as expectation values and the pointwise TDMF is presented in Table 16.

TABLE 16: Calculated transition dipole moment function (TDMF) for the A–X transition of OH.

Bond length (Å)	TDMF (Debye)	Bond length (Å)	TDMF (Debye)
0.69	0.551406575	2.58	-0.029737643
0.72	0.525323361	2.61	-0.027487391
0.75	0.499047585	2.64	-0.025386358
0.78	0.472659338	2.67	-0.023427991
0.81	0.446221839	2.7	-0.021605185
0.84	0.419806051	2.73	-0.01991077
0.87	0.393476072	2.76	-0.01833759
0.9	0.367294698	2.79	-0.016878728
0.93	0.341323238	2.82	-0.015527105
0.96	0.31562118	2.85	-0.014276058
0.99	0.290246098	2.88	-0.013119229
1.02	0.265253926	2.91	-0.01205029
1.05	0.240697412	2.94	-0.011063388
1.08	0.216628272	2.97	-0.010152831
1.11	0.193091217	3	-0.009313312
1.14	0.170132632	3.03	-0.008539753
1.17	0.147794716	3.06	-0.007827461

Table 16 (Continued)

1.2	0.126118017	3.09	-0.007171936
1.23	0.105138831	3.12	-0.006569158
1.26	0.08489381	3.15	-0.006014851
1.29	0.065418352	3.18	-0.005505522
1.32	0.046747654	3.21	-0.005037746
1.35	0.028917865	3.24	-0.004608321
1.38	0.011967015	3.27	-0.004214252
1.41	-0.004066264	3.3	-0.003852227
1.44	-0.019138303	3.33	-0.003520839
1.47	-0.033206721	3.36	-0.003217226
1.5	-0.046227397	3.39	-0.00293903
1.53	-0.058156425	3.42	-0.002684221
1.56	-0.068951789	3.45	-0.002450916
1.59	-0.078575907	3.48	-0.002237393
1.62	-0.08699085	3.51	-0.002042035
1.65	-0.094188153	3.54	-0.001863353
1.68	-0.100156612	3.57	-0.00169997
1.71	-0.104903714	3.6	-0.001550619
1.74	-0.108459124	3.63	-0.001414132
1.77	-0.110869662	3.66	-0.001289435
1.8	-0.112201856	3.69	-0.001175537
1.83	-0.112536105	3.72	-0.001071531
1.86	-0.111963979	3.75	-0.000976579
1.89	-0.110586262	3.78	-0.000889914
1.92	-0.108507527	3.81	-0.000810832
1.95	-0.105832904	3.84	-0.000738684
1.98	-0.102665113	3.87	-0.000672878
2.01	-0.099101219	3.9	-0.000612866
2.04	-0.095232282	3.93	-0.000558152
2.07	-0.091141048	3.96	-0.000508275
2.1	-0.086901483	3.99	-0.000462791
2.13	-0.082579166	4.02	-0.00042137
2.16	-0.078229518	4.05	-0.000383633

Table 16 (Continued)

2.19	-0.073900685	4.08	-0.000349255
2.22	-0.069632397	4.11	-0.000317944
2.25	-0.065457119	4.14	-0.00028943
2.28	-0.061400682	4.17	-0.00026347
2.31	-0.057482994	4.2	-0.000239833
2.34	-0.05371884	4.23	-0.000218316
2.37	-0.050118611	4.26	-0.000198731
2.4	-0.046688982	4.29	-0.000180907
2.43	-0.043433514	4.32	-0.000164688
2.46	-0.040353181	4.35	-0.000149931
2.49	-0.037446852	4.38	-0.000136506
2.52	-0.034711702	4.41	-0.000124294
2.55	-0.032143807	4.44	-0.000113187

Potential energy functions

The potential energy functions for the $A^2\Sigma^+$ and $X^2\Pi$ electronic states are calculated using Dunham constants with LeRoy's RKR program [158]. The RKR program uses vibrational G_v and rotational B_v polynomial coefficients and produces potential turning points by employing a first order semi-classical Rydberg-Klein-Rees (RKR) procedure. The G_v and B_v constants were taken from Brooke et al. [148] for $X^2\Pi$ state and from Luque and Crosley [143] for the $A^2\Sigma^+$ state. The potential energy curves for the $A^2\Sigma^+$ and $X^2\Pi$ electronic states with the TDMF are presented in Figure 40.

Transition Dipole Moment Matrix Element (TDMME) calculation

The calculated potential energy curves along with the TDMF points were used as input to LeRoy's LEVEL program [159]. LEVEL generates vibrational wave functions and energy levels by solving 1-D Schrödinger equation and subsequently

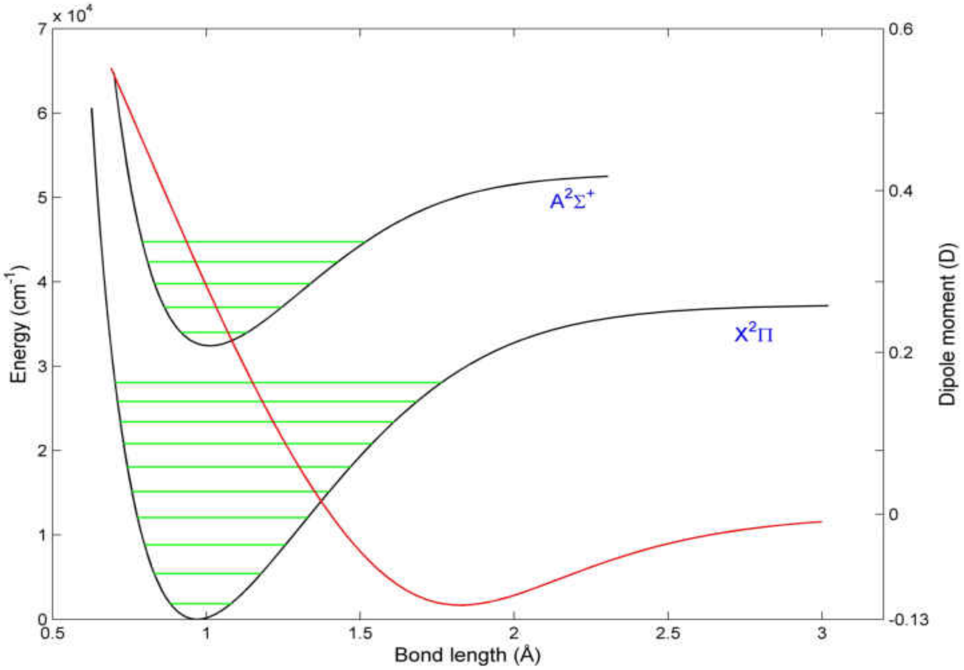

FIG. 40: RKR potential curves for $A^2\Sigma^+$ and $X^2\Pi$ electronic states of OH (in black) with TDMF (in red, with scale on right) for the A−X transition.

calculates TDMMEs. The radial range of integration was 0.5-3.0 Å with a radial step size of 0.0006 Å using cubic splines to interpolate the potential function and transition dipole moment points. LEVEL does not include electron spin in its calculation, which we refer to as Hund's case (b); therefore, these matrix elements (MEs) are in terms of the rotational quantum number (N) and not (J). However, it is necessary to transfer these MEs from Hund's case (b) to the case (a) in order to utilize them for intensity calculations using Western's PGOPHER program.

Including electron spin in the TDMMEs

The method of Brooke et al. [148] was used to transform TDMMEs from Hund's case (b) defined in terms of N to Hund's case (a) defined in terms of J by the following equation:

$$< \eta'\Lambda' \mid T^k_q(J'\Omega'J\Omega) \mid \eta\Lambda >= (-1)^{J'-\Omega'} \begin{pmatrix} J' & k & J \\ \Omega' & q & \Omega \end{pmatrix}^{-1} \times \sum_{N,N'} (-1)^{N-N'+S+J+k+\Lambda}$$
$$(2N'+1) \times (2N+1) \times \begin{pmatrix} J' & S & N' \\ \Omega' & -\Sigma & -\Lambda' \end{pmatrix} \begin{pmatrix} J & S & N \\ \Omega & -\Sigma & -\Lambda \end{pmatrix}$$
$$\times \begin{Bmatrix} N' & J' & S \\ J & N & k \end{Bmatrix} \begin{pmatrix} N' & k & N \\ -\Lambda' & q & \Lambda \end{pmatrix} \times < \eta'\Lambda' \mid T^k_q(N'N) \mid \eta\Lambda > \tag{83}$$

where $< \eta'\Lambda' \mid T^k_q(J'\Omega'J\Omega) \mid \eta\Lambda >$ are the case (a) MEs, $< \eta'\Lambda' \mid T^k_q(N'N) \mid \eta\Lambda >$ are the case (b) MEs, k is the rank of the transition moment and is equal to 1 for a single photon electric dipole transition; the component q is 0 for parallel and ±1 for perpendicular transitions and $\Omega = \Lambda + \Sigma$. The transformation is expressed using Wigner 3j and 6j symbols.

J-dependence of line intensities

TDMMEs are a function of the transition dipole moment and rotation-vibration wave functions. The rotation of diatomic molecules leads to an increase in the internuclear distance as a result of centrifugal distortion [160]. The rotational term in the effective diatomic potential means that the vibrational wave functions depend on J. This leads to ro-vibrational coupling and consequently affects the intensity of individual rotational lines for vibrational transitions, which is referred to as the Herman-Wallis (H-W) effect [161] for vibration-rotation transitions. The rotational part of the line intensities is no longer given by just the Hönl-London factor and a Herman-Wallis correction factor is needed [18]. For most heavy molecules, the rotation-vibration interaction is small and the overall wave function can be written as a product of a vibrational part and a rotational part. However, since OH is relatively a light molecule because of the H atom, J-dependent TDMMEs for each rotational transition have been included in the line intensity calculations. PGOPHER (version 10.0.505) [156] is now able to accept individual J-dependent matrix elements.

Line list calculations

To provide a line list with accurate line intensities, the J-dependent TDMMEs (see section 7.) were input into Western's PGOPHER. A line list for the $A^2\Sigma^+ - X^2\Pi$ electronic transition of OH has been provided in the online Supplementary Material [117]. PGOPHER provides an extensive line list that includes: J quantum numbers, parity (f, e), eigenvalue numbers, line position, rotational line strength, Einstein coefficients (A), branches and bands [156]. The oscillator strengths $(f_{J' \leftarrow J''})$ are also calculated by PGOPHER.

A summary of entire computational method, starting from Dunham coefficients for calculation of PEC to the production of a linelist OH and the intermediate processes which are discussed in the chapter, is presented in the Figure 42.

Results and discussion

Transition Dipole Moment Function (TDMF)

Line intensities are sensitive to a small variation in the TDMF, and therefore the accuracy of the TDMF is crucial. As a check, the calculated TDMF in this study was compared those in the literature. For example Figure 41. compares our TDMF with that of Bauschlicher and Langhoff, [151] and Luque and Crosley [143]. In general, the agreement is good between the TDMF calculated by us and those from the literature.

Einstein A coefficients and lifetimes

The Einstein coefficients $(A_{v'v''})$ were calculated for all possible bands of the A$-$X transition by summing all possible transitions from J'=2.5 in the F_1 spin component. We obtained the value of f=1.055×10^{-3} for the oscillator strength of (0,0) band compared to Wang and Killinger's value of 1.13×10^{-3} [150]. Transitions with up to Δv=5 were included in the calculations. We note that for Δv>5 the calculated band intensities no longer decrease as expected and they were therefore excluded. This problem in the calculated TDMMEs occurs because of various numerical issues such as "noise" in the calculated TDMF [162].

Our band Einstein A values are also compared to the results from the work of

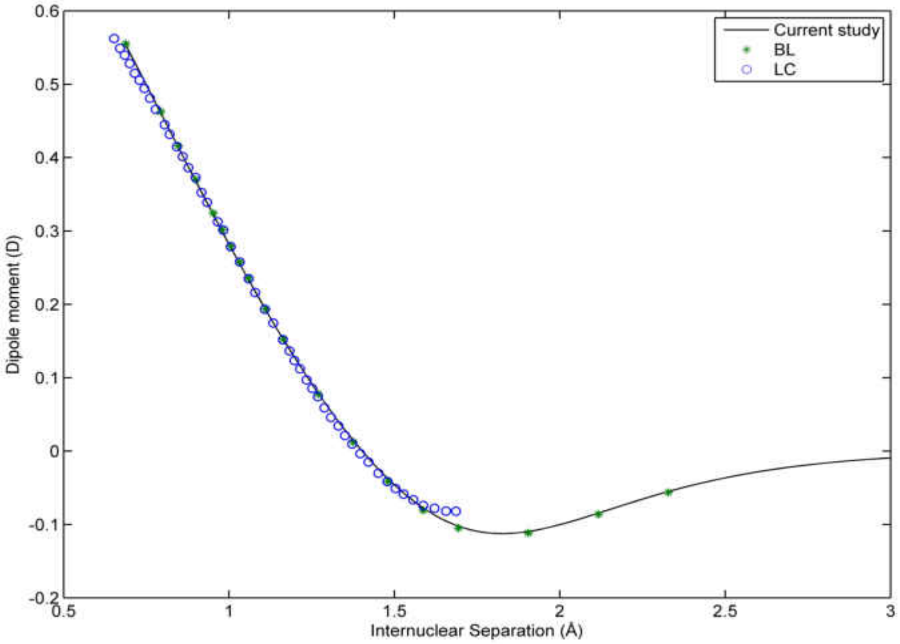

FIG. 41: TDMFs: This study (–), Bauschlicher and Langhoff (BL) (*) and Luque and Crosley (LC) (○).

Luque and Crosley [143]. Table 17 shows Einstein A coefficients for all bands (v$'$=0−4 & v$''$=0−9) in the A−X system compared to the same values from Luque and Crosley [143]. Overall the results of our study agree well with Luque and Crosley [143]. The discrepancy for Einstein A coefficients for some bands presumably is the result of slight differences in the TDMFs. From Table 17, using the Einstein (A$_{v'v''}$) values, the radiative lifetimes were calculated by

$$\tau_{v'} = \frac{1}{\sum_{v''} A_{v'v''}} \tag{84}$$

Our calculated values of $\tau_{v'}$ were compared to the experimental values of German [163], Copeland et al. [164] and theoretical calculations from Yarkony [154], Bauschlicher and Langhoff [151], Luque and Crosley [143] and Billoux et al. [165]. As shown in Table 18 there is a good agreement between the radiative lifetimes from this study and those of the mentioned experimental and theoretical calculations within error.

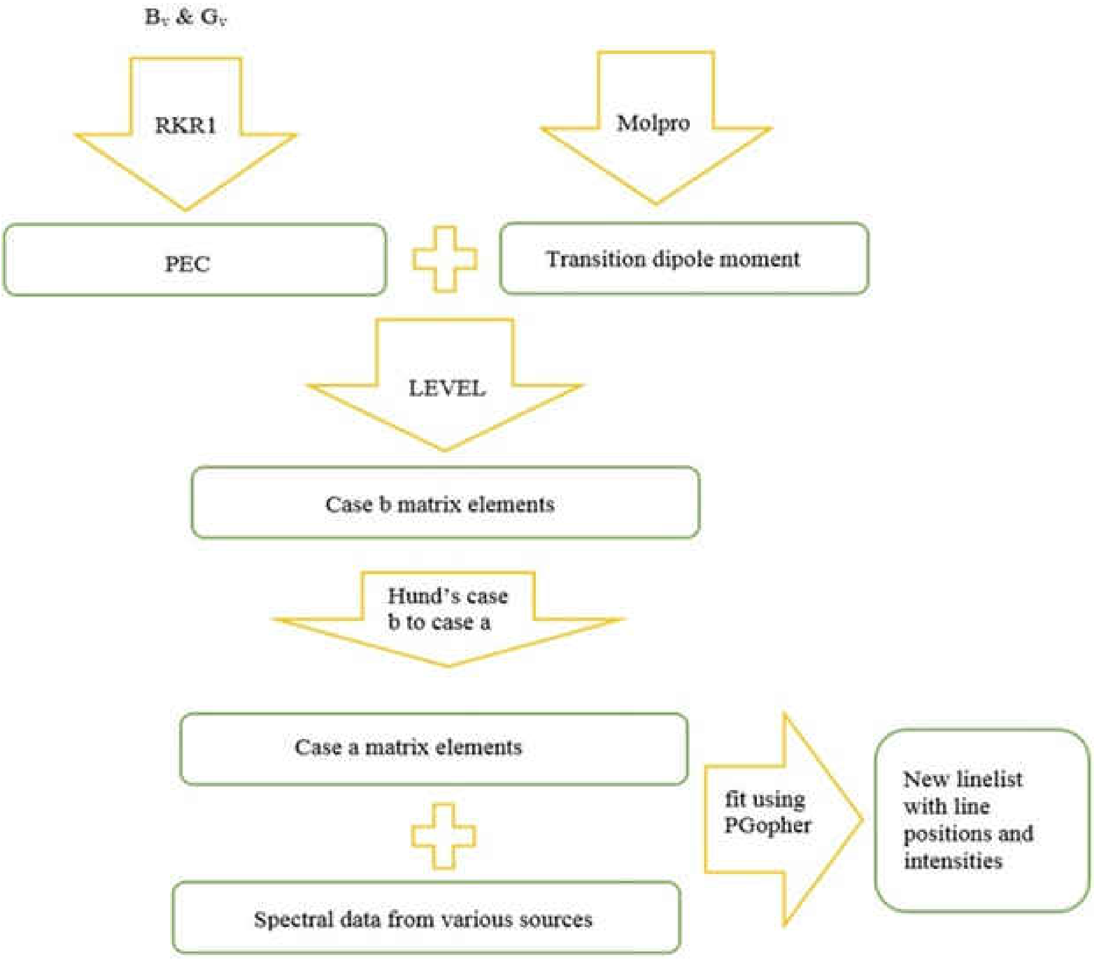

FIG. 42: Overall method for the production of the linelist for OH

TABLE 17: Band Einstein coefficients ($A_{v'v''}$) from this study and Luque and Crosley [143].

v′,v″	$A_{v'v''}$ (s^{-1})	$A_{v'v''}$ $(s^{-1})^{a}$
0,0	1.467×10^{6}	1.451×10^{6}
0,1	5.901×10^{3}	6.921×10^{3}
0,2	1.252×10^{2}	1.986×10^{2}
0,3	9.466×10^{0}	1.009×10^{1}
0,4	3.880×10^{-2}	4.828×10^{-2}
0,5	1.351×10^{-4}	...

Continued on next page

TABLE 17 – continued from previous page

v′,v″	$A_{v'v''}$ (s^{-1})	$A_{v'v''}$ (s^{-1})[a]
1,0	4.750×10^{5}	4.643×10^{5}
1,1	8.834×10^{5}	8.595×10^{5}
1,2	7.284×10^{3}	8.207×10^{3}
1,3	5.903×10^{2}	8.598×10^{2}
1,4	5.699×10^{1}	6.022×10^{1}
1,5	3.411×10^{-1}	3.336×10^{-1}
1,6	3.054×10^{-3}	...
2,0	9.705×10^{4}	9.202×10^{4}
2,1	7.024×10^{5}	6.852×10^{5}
2,2	4.700×10^{5}	4.472×10^{5}
2,3	5.296×10^{3}	5.698×10^{3}
2,4	1.757×10^{3}	2.379×10^{3}
2,5	2.137×10^{2}	2.201×10^{2}
2,6	2.151×10^{0}	...
2,7	1.928×10^{-2}	...
3,0	1.773×10^{4}	1.551×10^{4}
3,1	2.484×10^{5}	2.374×10^{5}
3,2	7.144×10^{5}	6.928×10^{5}
3,3	2.094×10^{5}	1.931×10^{5}
3,4	2.141×10^{3}	2.169×10^{3}
3,5	4.179×10^{3}	5.274×10^{3}
3,6	7.106×10^{2}	6.347×10^{2}
3,7	1.061×10^{1}	...
3,8	8.647×10^{-2}	...
4,0	3.300×10^{3}	2.850×10^{3}
4,1	6.827×10^{4}	6.310×10^{4}
4,2	3.933×10^{5}	3.777×10^{5}
4,3	5.728×10^{5}	5.495×10^{5}
4,4	7.097×10^{4}	6.247×10^{4}
4,5	1.524×10^{2}	1.318×10^{2}

Continued on next page

TABLE 17 – continued from previous page

v′,v″	$A_{v'v''}$ (s^{-1})	$A_{v'v''}$ $(s^{-1})^{a}$
4,6	8.494×10^{3}	9.968×10^{3}
4,7	1.680×10^{3}	1.568×10^{3}
4,8	4.459×10^{1}	...
4,9	3.857×10^{-1}	...

[a] values taken from Luque and Crosely [143]

TABLE 18: Radiative lifetimes of the A state

v'	$\tau_{v'}$ (ns)	Ref
0	679	This study
	688 ± 21	[163] (Exp)
	693 ± 20	[164] (Exp)
	673	[151] (Calc)
	686	[143] (Calc)
	672	[154] (Calc)
	679	[165] (Calc)
1	732	This study
	736 ± 22	[164] (Exp)
	750	[143] (Calc)
	718	[154] (Calc)
	733	[165] (Calc)
2	783	This study
	811	[143] (Calc)
	762	[154] (Calc)
	785	[165] (Calc)
3	835	This study
	872	[143] (Calc)
	803	[154] (Calc)
	838	[165] (Calc)
4	894	This study
	937	[143] (Calc)

Table 18 (Continued)

v'	$\tau_{v'}$ (ns)	Ref
	844	[154] (Calc)
	898	[165] (Calc)

For a more complete investigation, relative band Einstein A coefficients ($A_{v'v''}/A_{00}$), assuming $A_{00} = 1000$, were calculated and compared to the experimental values of Crosley and Lengel [149] (from Table 19 of Bauschlicher and Langhoff [151]), Luque and Crosley [143] and the theoretical ($A_{v'v''}/A_{00}$) values of Bauschlicher and Langhoff [151], and are listed in Table 19. Note that the selected bands are based on available relative band Einstein A coefficients from Bauschlicher and Langhoff [151] plus some additional bands with v'=4.

The experimental papers [149, 143] used relative emission intensities (branching ratios) for transition moment calculations. Crosley and Lengel [149] represented the transition moment as $R_e = c(1-\rho r)$ with $\rho = 0.75$ Å^{-1} and Luque and Crosley [143] represented transition moments as a polynomial $R_e(r) = a_0 + a_1 r + a_2 r^2 + a_3 r^3$ with polynomial coefficients derived from the experimental intensity ratios. The relative Einstein A values (Table 19) from the current study agree well with these studies. However, our theoretical relative Einstein A values agree better with the values derived from experimental measurements [149, 143], compared to the Bauschlicher and Langhoff values [151].

TABLE 19: Einstein coefficients ($A_{v'v''}$) relative to $A_{00} = 1000$

v′,v″	Luque [143]	This study	Bauschlicher [151] [a]
0,0	1000	1000	1000
0,1	4.8	4	5.6
1,0	320	322.5	339.5
1,1	592.3	601.2	599.9
1,2	5.7	4.95	6.2
2,0	63.4	65.7	71.4
2,1	472.2	477	487.3
2,2	308.2	317.1	323.2
2,3	3.9	3.6	6.3
3,0	10.7	12	12.9
3,1	163.6	169	177.9
3,2	417.4	485.6	475.8
4,0	1.96	2.22	...
4,1	43.5	46.2	...
4,2	260.30	266.80	...
4,3	378.70	389.81	...
4,4	43.05	48.58	...
4,5	0.09	0.10	...
4,6	6.87	5.74	...
4,7	1.08	1.13	...

The Einstein A coefficients ($A_{J'J''}$) for all the main and satellite transitions in the (0,0) band of A−X system were compared to the Einstein A's for the same transition from HITRAN [140] and also LIFBASE [142] and the results are presented as the percentage difference (ΔA) as a function of J″ in Figure 43. It should be noted that the highest rotational level in the HITRAN database [140] is 15.5; therefore only the rotational levels up to J″=15.5 were included (Figure 43 a,b). With regard to HITRAN, the difference is in the range of 0-2 % for the main and 0-10 % for the satellite transitions (See Figure 43 a,b). In the case of LIFBASE (See Figure 43 c,d),

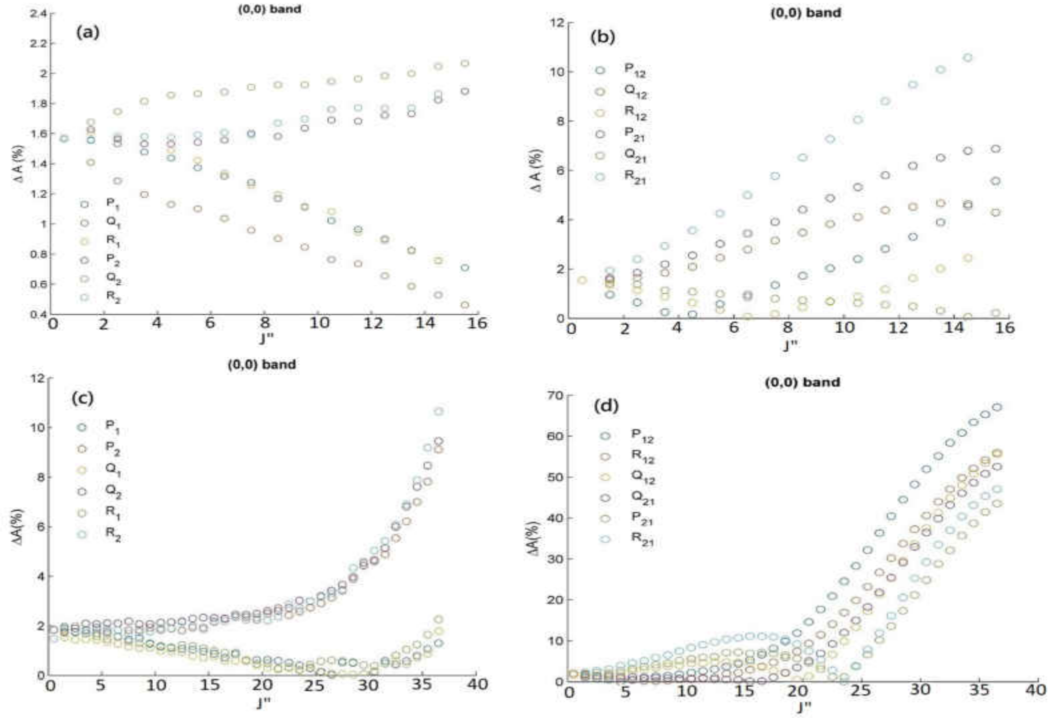

FIG. 43: Comparison differences of Einstein A coefficients (ΔA) in percent versus J'' with HITRAN database ((a) main , (b) satellite) and LIFBASE ((c) main , (d) satellite) in the (0,0) band for the A−X system of OH

this difference remains nearly the same up to $\sim J'' \leq 25$. For the $25 < J'' \leq 30$, the difference is in the range of 0-4 % for the main and 0-40 % for the satellite transitions. For $J'' > 35$, this difference increases up to ∼ 10% for the main and ∼ 60% for the satellite transitions. Here in Figure 43 we only present a comparison of Einstein A coefficients for the (0,0) band; however for the other bands we observed a similar trend.

Relative intensities

Another way to evaluate the transition moments is by using line intensities from experiment. It is useful to make a limited comparison between calculated line intensities in this work and experiment by comparing the peak intensity of a number of lines from the simulated and observed spectra [139]. However, it is difficult to do such a comparison because the observed emission spectrum of Stark et al. [139] recorded at the National Solar Observatory at Kitt Peak from a helium plasma cannot be described by a single, well-defined temperature. The spectrum was obtained from McMath-Pierce facility FTS spectral archives (`https://nsokp.nso.edu/archives`). In order to make a better comparison, line strength ratios $S_{X_y}(J'' \pm 1)/S_{Q_y}(J'')$; $(X = R, P, \& y = 1, 2)$ were calculated for lines with same upper state J value to remove the excited state population factor from the line intensities. The line strength ratios for the $(0, 0)$ vibrational band with randomly selected J'' were calculated and compared to the observed line strength ratios as listed in Table 20 including the relative errors. The calculated relative intensities are within $\sim 1\%$ of the observed ratios, indicating very good agreement between the calculated and observed line intensities.

TABLE 20: Relative line intensities for the (0,0) band of OH A−X transition

Intensity ratio	This Study	Observed[a]	Percentage error
$S_{P1(3.5)}/S_{Q1(2.5)}$	0.972	0.984	1.21
$S_{P1(6.5)}/S_{Q1(5.5)}$	0.680	0.675	0.74
$S_{P1(8.5)}/S_{Q1(7.5)}$	0.626	0.629	0.47
$S_{P1(11.5)}/S_{Q1(10.5)}$	0.585	0.59	0.8
$S_{P1(13.5)}/S_{Q1(12.5)}$	0.57	0.58	1.72
$S_{P1(17.5)}/S_{Q1(16.5)}$	0.556	0.557	0.17
$S_{P1(20.5)}/S_{Q1(19.5)}$	0.545	0.555	1.80
$S_{P1(22.5)}/S_{Q1(21.5)}$	0.541	0.547	1.09
$S_{P1(25.5)}/S_{Q1(24.5)}$	0.536	0.542	1.10
$S_{R1(2.5)}/S_{Q1(2.5)}$	0.243	0.239	1.67
$S_{R1(6.5)}/S_{Q1(7.5)}$	0.384	0.392	2.04
$S_{R1(9.5)}/S_{Q1(10.5)}$	0.420	0.422	0.47
$S_{R1(11.5)}/S_{Q1(12.5)}$	0.433	0.43	0.69
$S_{R1(12.5)}/S_{Q1(13.5)}$	0.439	0.44	0.22
$S_{R1(14.5)}/S_{Q1(15.5)}$	0.447	0.45	0.66
$S_{R1(17.5)}/S_{Q1(18.5)}$	0.455	0.45	1.11
$S_{R1(23.5)}/S_{Q1(24.5)}$	0.465	0.471	1.27
$S_{P2(2.5)}/S_{Q2(1.5)}$	0.782	0.799	2.12
$S_{P2(5.5)}/S_{Q2(4.5)}$	0.634	0.635	0.15
$S_{P2(8.5)}/S_{Q2(7.5)}$	0.585	0.59	0.84
$S_{P2(10.5)}/S_{Q2(9.5)}$	0.569	0.58	1.89
$S_{P2(21.5)}/S_{Q2(20.5)}$	0.535	0.55	2.72
$S_{P2(24.5)}/S_{Q2(23.5)}$	0.531	0.525	1.14
$S_{R2(3.5)}/S_{Q2(4.5)}$	0.374	0.381	1.83
$S_{R2(6.5)}/S_{Q2(7.5)}$	0.4157	0.416	0.057
$S_{R2(8.5)}/S_{Q2(9.5)}$	0.430	0.4253	1.10
$S_{R2(11.5)}/S_{Q2(12.5)}$	0.445	0.434	2.53

Astronomical comparisons

As a further check, we compared our calculated line list to some observed astronomical spectra. We present the observed spectrum of the solar photosphere (Figure 44), and of the metal-poor carbon and nitrogen-rich star HD196944 (Figure 45) compared to synthetic spectra in which the OH lines are based on our new line list. The data are from a high resolution and high signal-to-noise solar spectrum observed by Kurucz et al. [166] and the stellar spectrum recorded with the blue arm of the UVES spectrograph [167] mounted on the Unit 2 of the Very Large Telescope (Mount Paranal, Chile).

The spectral syntheses are computed via a one−dimensional radiative transfer algorithm under the assumption of local thermodynamic equilibrium (see, for example, [168]). The parameters for the metal-poor star have been adopted from Masseron et al. [169]. In addition to a specific model atmosphere that corresponds to the stellar parameters, the syntheses in Figure. 44 and 45 involve other molecular and atomic species. These include atomic transitions from the VALD3 database [170] and NH transitions [171]. While the syntheses without the OH line list highlight missing transitions in the simulated spectra compared to the observations, the inclusion of the OH line list as computed in this work greatly improves the fit and thus confirms that the current line list is of high quality. The agreement between the observations and the models is excellent.

Summary and conclusion

The observed OH A−X lines were collected from various sources. A new transition dipole moment function was calculated out to 3.0 Å and it gives good agreement with experimental lifetime values. A new extensive ($v^{'} = 0-4$, $v^{''} = 0-9$, $J_{max} = 35.5$) line list was calculated for the A−X transition of OH that includes the J dependence of the TDMMEs to improve the accuracy of the line intensities. This line list is available as online supplementary [117] material and is suitable for updating HITRAN [140].

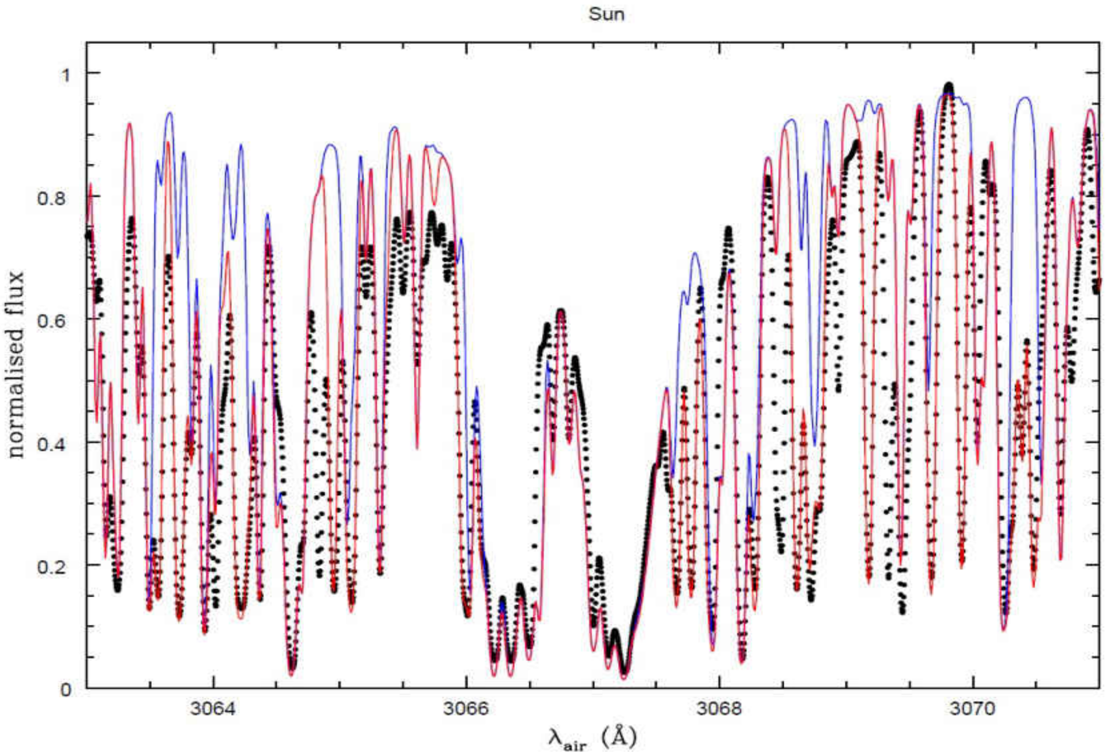

FIG. 44: Comparison between observed solar spectrum (black dotted line) and their respective synthesis with (red) and without (blue) the line list presented in this work.

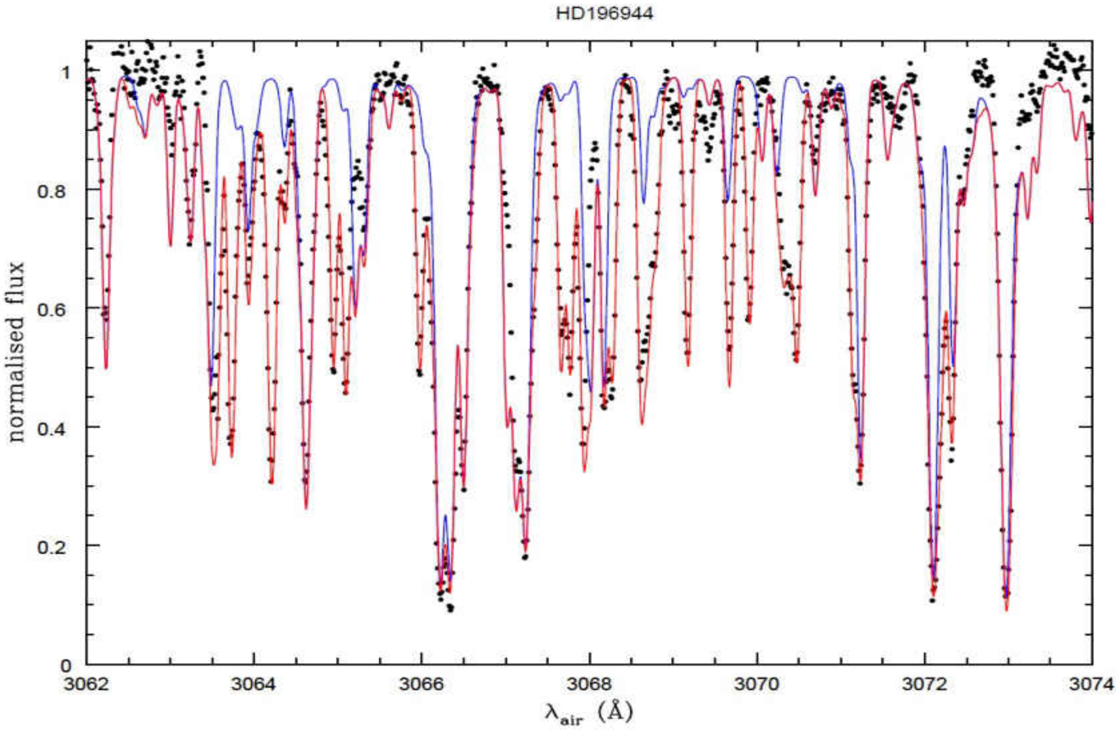

FIG. 45: Comparison between observed stellar spectrum (HD196944) (black dotted line) and their respective synthesis with (red) and without (blue) the line list presented in this work.

CHAPTER 8

LINE PARAMETERS FOR HOT METHANE ν_3 BAND BROADENED BY H_2 FROM 296 K TO 1100 K.

The spectral measurements for this study were taken at the molecular spectroscopy group by me and Mike Dulick. A non-linear multi-spectrum list square fit developed at the German Space Agency (DLR) was used for fitting the spectra. The fitting of the measured spectra, and preparing figures and tables were done by me. This study was supervised by Dr. Peter Bernath. The results of this study are expected to be submitted to the 'Journal of Quantitative Spectroscopy and Radiative Transfer' for publication.

Introduction

Recently, there has been great interest in cool methane-containing astronomical objects outside of the Solar System, such as exoplanets including hot Jupiters [172, 173], hot Neptunes [174, 175] and super-Earths [176, 177]. Methane has also been detected in the atmospheres of brown dwarfs, which are cool sub-stellar objects unable to fuse hydrogen in their cores [178]. Understanding the atmospheric composition of exoplanets and brown dwarfs gives valuable information on the history of planetary evolution [179], their appearance [173], the temperature profile [180], the chemical composition of the planet's core, the C/O ratio and so forth [174, 178]. For example, an accurate measurement of CH_4 abundance can constrain the C/O ratio, which is an important factor in the chemical composition of the atmosphere as well as classifying the exoplanet [173, 174, 175, 181]. The atmospheres of these giant planets and brown dwarfs are complex and have opacities that vary with wavelength [178].

Ground and space-based near-infrared spectroscopic observations have been essential for studying the atmospheres of exoplanets and brown dwarfs [172, 180]. Methane (CH_4) has been observed in the atmosphere of hot Jupiters [182], hot Neptunes [175, 183] and brown dwarfs [178]. CH_4 is expected to be the main carbon-bearing molecule in the atmospheres of Jovian planets and brown dwarfs at temperatures about ~ 1000 K [184, 185].

Atmospheres of hot Jupiters and brown dwarfs are dominated by H_2. The main carbon-containing molecules are CO and CH_4 and their relative abundance depends on temperature and pressure [186]. In addition to observations, photochemical radiative transfer models are used to predict the atmospheric composition [174, 184, 187]. These models require reliable opacities in order to correctly model the atmosphere of exoplanets [92]. Methane is the main contributor to the atmospheric opacity of hot Jupiters and brown dwarfs [172, 188].

There have been many detections of H_2-dominated hot exoplanets (hot Jupiters) that contain significant amounts of CH_4. To calculate atmospheric opacity of exoplanets and brown dwarfs, an accurate linelist for methane is required [189]. In case of H_2-dominated giant planets, the collisional interactions with H_2 result in broadened CH_4 lines at high temperatures [190, 191, 192, 193, 194].

The line parameters needed include line position, strength, pressure-induced broadening and shift, speed dependent parameters, as well as their temperature-dependence. Pine measured the pressure-induced broadening and shift of methane Q branch lines in the ν_3 band using various broadening gases at room temperature [191]. In another study, Pine and Gabard measured additional line mixing and Dicke narrowing parameters as well as pressure-induced broadening and shift parameters for the Q branch in the ν_3 band of methane using a multi-spectrum fitting method [195]. Smith et al. measured the temperature-dependence of broadening and shifting of CH_4 spectral lines in the ν_4 band using air and N_2 at low temperatures and found a significant rotational dependence [196]. Varanasi and Chudmani also measured the temperature-dependence of broadening of methane in the ν_4 band at low temperatures [190].

In addition to measurements, there have also been theoretical studies predicting methane line parameters. Anderson used perturbation theory and related the pressure-induced broadening by a foreign agent to electrostatic intermolecular collisions [197]. Neshyba et al. [198] used complex Robert-Bonamy theory to describe line broadening and shifting in the CH_4-N_2 system. They found that repulsive intermolecular Lennard-Jones atom-atom interactions are the main contributor to linewidth broadening and that the broadening decreases with increasing J quantum number. Gabard [199] developed a semiclassical method for the broadening of methane lines perturbed by diatomic molecules using a symmetrized version of Robert-Bonamy theory. In addition, Smith and Secrest [200] developed a new interaction potential for the Ar-CH_4 collision system and calculated a total collision cross-section for different A, E and F rotational symmetry levels. They concluded that the total collisional cross-section for the E component is smaller than for the A and F components. This was in agreement with Smith et al.'s [196] conclusion about the symmetry dependence of line broadening from the Fourier transform infrared measurements of the ν_4 mode.

The Voigt profile is the standard lineshape model used in high-resolution spectroscopy because of its relative simplicity. However, increasing sensitivity and accuracy of spectroscopic techniques enables the use of new lineshapes such as the Hartmann–Tran (H–T) line model [201, 202], also called the partially Correlated quadratic-Speed-Dependent Hard Collision Profile (pCqSD-HCP) model, in which additional effects such as speed-dependence of the broadening, shifting and collisional narrowing are taken into account.

The temperature-dependence of spectral line parameters are often expressed as a single power law $\chi(T) = \chi(T_0) * (T_0/T)^n$, where T_0 is a reference temperature and $\chi(T_0)$ is the parameter at T_0. However, a single power law does not always explain temperature-dependence of line parameters such as pressure broadening [196, 202]. Gamache and Vispoel [203] developed a double power law expression that predicts temperature-dependence of the broadening parameter over a large temperature range. Also, a linear temperature-dependence has been observed for the pressure-induced line shift [196, 202].

While there have been extensive studies of methane line parameters, most studies have focused on the conditions for Earth's atmosphere at relatively low temperatures

[191, 192, 195, 196] and cover a limited spectral region [204]. Only one high temperature study of $CH_4.H_2$ system has been published for a limited range of temperatures and pressures [193]. In my study, I aimed to measure methane line parameters as well as their temperature-dependence in the ν_3 band for both P and R branches in the presence of H_2. The goal was to measure methane pressure-induced line parameters for a large temperature range from room temperature to $\sim$ 1100 K. In this study, in addition to the Voigt profile, the Hartmann–Tran model was used in order to determine speed dependence. First order Rosenkranz line mixing was added to acount for line mixing. This study will contribute to a better understanding of hydrogen-dominated hot exoplanets and brown dwarfs.

Experimental set up

Instrumentation

All of the spectra were recorded using a Bruker 120 /125 HR Fourier transform spectrometer (120 HR bench with 125 HR upgraded electronics) at Old Dominion University at a spectral resolution of 0.01 cm^{-1} (MOPD=90 cm). A schematic of the experimental arrangement is shown in Figure 46. H_2 and CH_4 pressures were separately measured using two MKS Baratron pressure gauges (MKS 220 C model with 1000 Torr and MKS 626 B with 10 Torr maximum pressure) with 0.5 and 0.05 Torr accuracy, respectively. The desired H_2 and CH_4 gas partial pressures in the cell for each temperature were calculated using the ideal gas law. These pressures of CH_4 and H_2 were stored in two separate tanks from the gas cylinders at room temperature. The cell was heat up to the desired temperature with a CM Rapid Temp furnace tube. Subsequently, first CH_4 and then H_2 were led in to the cell from their storage tanks. The nominal temperature measurements were made using a thermocouple sensor provided by the furnace manufacturer. In a separate experiment, more accurate temperature measurements were carried out inside the furnace with another thermocouple at the nominal temperatures measured by the furnace thermocouple. The thermocouple was positioned inside the cell and parallel to its axis, to measure the temperature inhomogeneity. Temperature measurements showed a maximum temperature at the center of the cell that drops by about 20 K at the ends of cell. Finally, the nominal temperatures were calibrated using measured

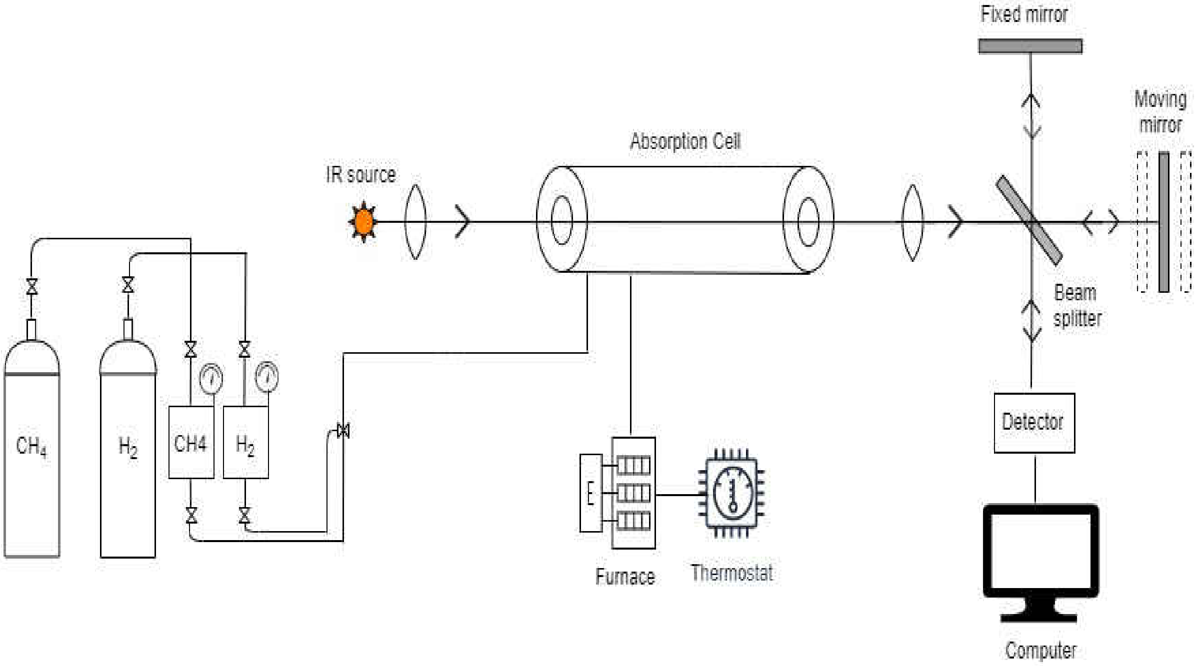

FIG. 46: Schematic view of the experimental setup including the IR source, the absorption cell, and Bruker 125/120 HR FTS.

temperatures at the center of the cell.

Because of the high temperature nature of the experiment, the cell was made of quartz (SiO_2) that has a high melting point. The 50.8 cm long cell used quartz lenses (25 cm focal length) as cell windows that were fused to the cell body. Emitted light from an infrared source (glowbar) was collimated, passed through the cell and was then focused onto the entrance aperture of the spectrometer with another quartz lens. The spectral range of 1800-5500 cm^{-1} was selected using a Ge filter and an Insb detector.

Experimental conditions and recorded spectra

The goal of this study was to measure pressure-induced broadening and shifting coefficients of the ν_3 methane lines at high temperatures. The CH_4 infrared spectrum was measured at five different calibrated temperatures of 296 K, 463 K, 681 K, 894 K, and 1098 K in in the 2750-3200 cm^{-1} range. At each temperature, the CH_4 spectrum was measured at five different pressures of H_2 at 50, 150, 240, 320, and 400 Torr as well as pure CH_4 for which the partial pressure of CH_4 was 0.5 Torr.

At the high temperature of the experiment, there is emission from the cell and from hot CH_4 in the recorded spectra. In this experiment, the true transmittance spectrum of CH_4 is required; therefore it is necessary to correct for emission. Four spectra were recorded: A, gas absorption (glowbar source with gas); B, gas emission (no glowbar with gas); C, reference (glowbar source without gas); and D, cell emission (no source and no gas). An example of four recorded spectra and the resulting gas transmittance is shown in Figure 47. Each of the emission and absorption spectra were an average of 128 co-adds and the transmission spectrum is calculated as [207]

$$\tau = \frac{A - B}{D - C}. \tag{85}$$

Data analysis

Spectrum preparation: line position calibration and continuum/baseline correction

All CH_4 spectra were converted from their interferograms using “boxcar” apodization with a zero filling factor of 2. The continuum baseline of the transmission spectra were not always at 100%. This is caused mainly by drifting of the infrared source over the period of data acquisition. The Bruker OPUS software was used for the continuum baseline correction.

To calibrate the line positions, the measured spectra were compared to the HITRAN 2012 [41] database. For each temperature, a pure CH_4 spectrum with no added H_2 was measured. The line positions were fitted and extracted. Several isolated line positions were selected and compared to HITRAN values. For each temperature, a calibration factor was calculated by averaging over line position ratios for the selected lines. Calibration factor for temperatures 296 K, 463 K, 681 K, 894 K, and 1098 K are 0.999996860 (0.009484354), 0.999996917 (0.009337925), 0.999996980 (0.009152939), 0.999997302 (0.008128944), 0.999997317 (0.00813221), respectively.

Line profiles and line parameter retrieval

To measure the line parameters of CH_4, a multi-spectrum-weighted non-linear least squares fit was performed. To improve the determination of line parameters, fitting was done with software developed at the German Space Agency (DLR) [202].

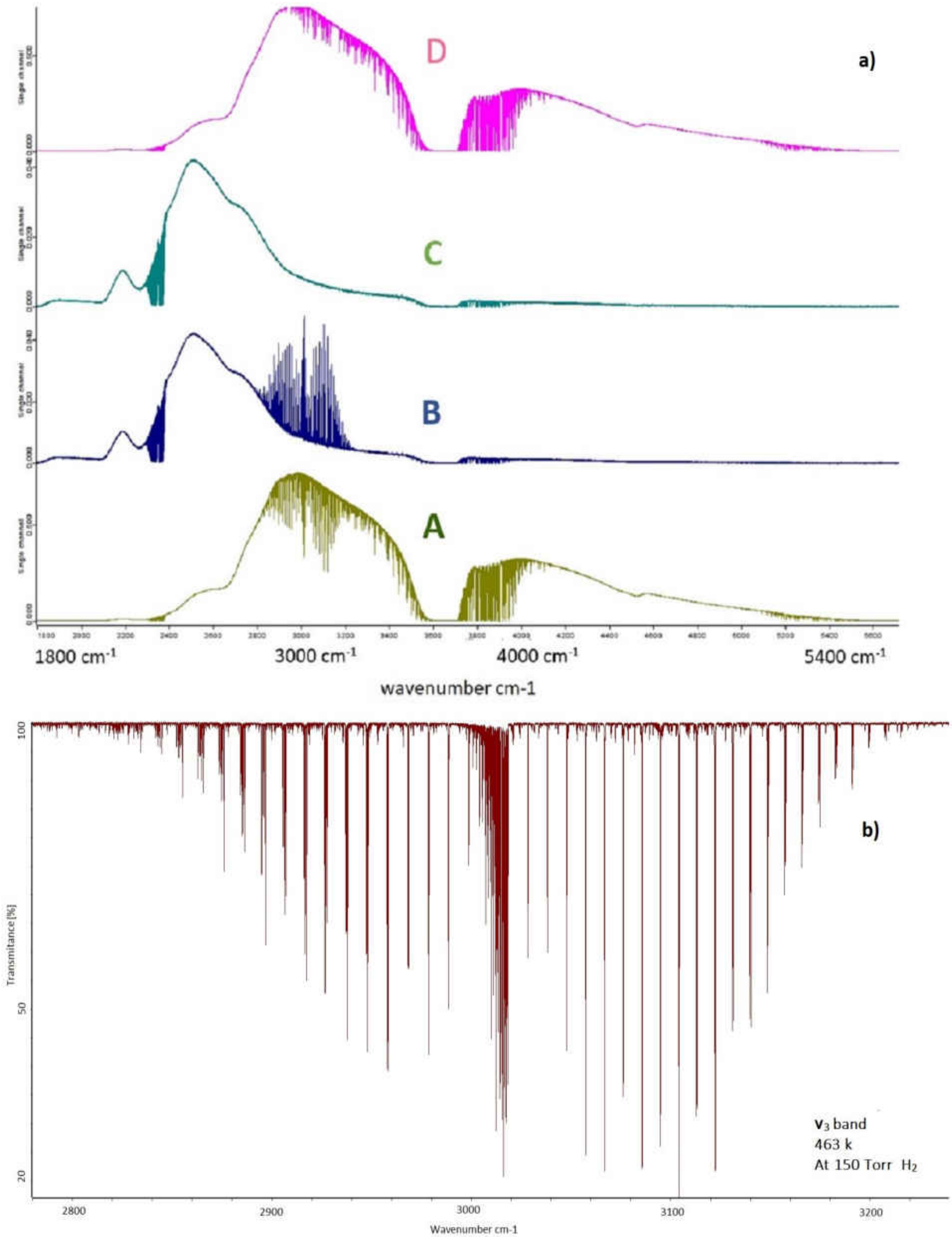

FIG. 47: (a) Four measured spectra A. gas absorption B. gas emission C. cell emission D. glowbar reference (b) the resulting gas transmittance at 150 Torr and 463 K.

For each temperature a simultaneous non-linear least squares fit for spectra recorded at multiple pressures of H_2 was carried out. The recorded spectra show broadened lines as a result of two mechanisms: Maxwell-Boltzmann velocity distribution that results in Doppler broadening, and collisional broadening often represented by a Lorentzian profile. A Voigt profile is a convolution of a Gaussian and a Lorentzian profile [18] and is frequently used for spectral fitting because of its relative simplicity.

In this study, initially, the Voigt lineshape was used to fit the CH_4 lines. Line position (cm^{-1}), line intensity (cm/molecule), Lorentzian Half-Width at Half Maximum (HWHM) of pressure broadening (γ_0), and Lorentzian pressure shift (δ_0) parameters in units of cm^{-1}/atm were fitted simultaneously. Doppler broadening was set to a fixed calculated value at the measured temperature. Another line profile used to fit the methane lines is a quadratic speed-dependent hard collision (qsDHC) model in the Hartmann-Tran implementation [201, 202]; Rosenkranz first order line mixing was also used [205, 206]. In addition to γ_0 and δ_0, this line profile takes into account speed dependence of pressure-induced broadening (γ_2), pressure-induced shifting (δ_2), the effect of velocity changing collisions known as Dicke narrowing (ν_{VC}), and Rosenkranz first order line mixing (Y). For the non-Voigt analysis, we applied the symmetry line coupling selection rules in which only neighboring $A_1 \leftrightarrow A_2$, $F_1 \leftrightarrow F_2$ and $E \leftrightarrow E$ can couple [208]. In this study, γ_2 was set to zero. Finally, we fixed the Dicke narrowing coefficient to the theoretical value calculated by

$$\nu_{VC} = \frac{kT}{2\pi m D(T)} \tag{86}$$

where k is the Boltzmann constant, m is the molar mass and *D(T)* is the temperature dependent diffusion coefficient [209].

Fit procedure

The multi-spectrum fitting program reproduces the measured spectra at each hydrogen pressure in separate windows. The fit program divides the spectrum into micro-windows with a spectral width of ~ 2 cm^{-1}; this makes the continuum baseline less critical in the fitting. At high temperatures, decomposition of CH_4 occurs, which leads to a decrease in the partial pressure of CH_4 (initially at 0.5 Torr). To determine a true number density, a single spectrum fit was done for each pressure of H_2 at each temperature. The number density factor was adjusted for a number of selected lines

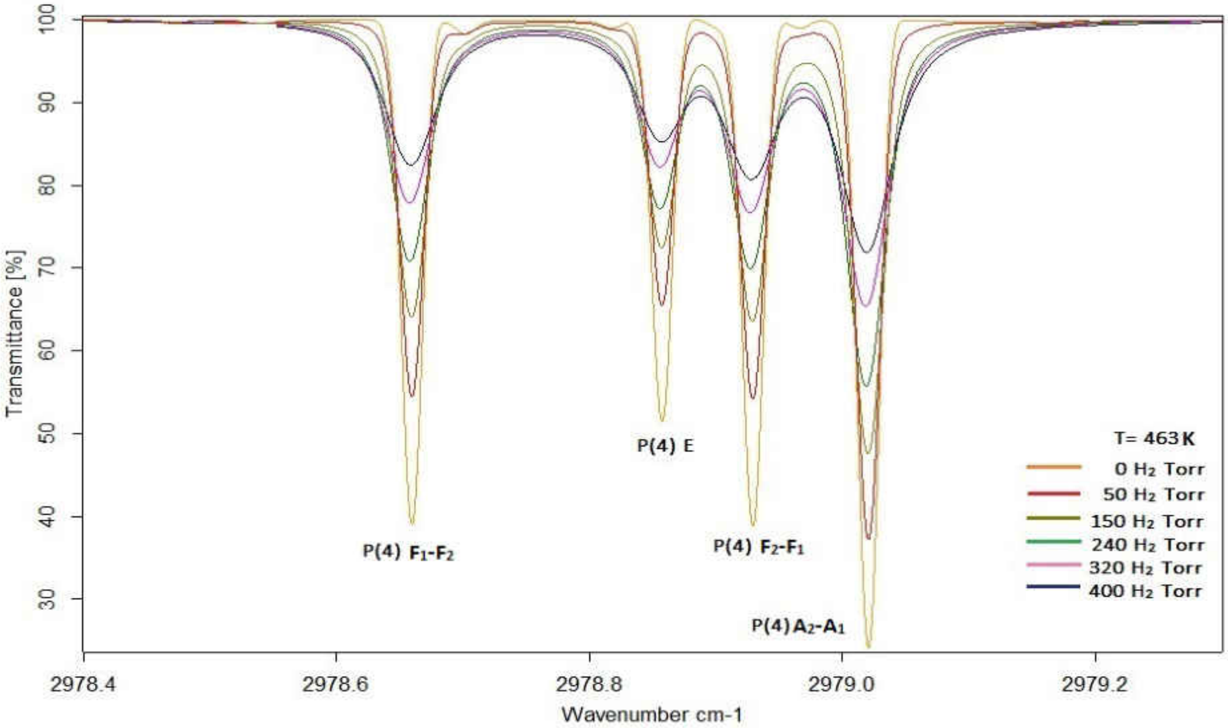

FIG. 48: Measured spectra of P(4) line of ν_3 band of CH_4 with assigned symmetries, with different pressures of H_2 at 463 K

while the line intensity was kept fixed at HITRAN 2012 [41] values. A single factor was obtained by averaging the adjusted number density for the selected lines.

Consequently, as the initial guess, a multi-spectrum fit was carried out with initial line parameters taken from the HITRAN 2012 database [41] with air as the broadening agent. Once an initial run of the multi-spectrum fit was done, the parameters with non-physical values or undetermined parameters were removed from the fit for the next iteration.

Results and discussion

Pressure-induced line broadening (γ_0)

Increasing hydrogen pressure leads to the broadening of spectral lines (see Figure 48). These line broadenings depend on the temperature at which the spectrum is recorded. In the literature, temperature-dependence of the line broadening parameter is usually expressed in the single power law (SPL) form of

$$\frac{\gamma_0(T)}{\gamma_0(T_0)} = (\frac{T_0}{T})^n, \tag{87}$$

in which T_0 is the reference temperature and n is the temperature-dependence coefficient. The SPL is derived under the assumptions that 1) temperature range is small, 2) the intermolecular potential only contains one term; and 3) all collisions are on resonance [203]. In this study, a wider temperature range from 296 K to about 1100 K was used to investigate the broadening parameters of CH_4. Recent studies on the temperature-dependence of pressure-induced broadening show that in the case of wide temperature ranges the SPL is not sufficient to predict the temperature-dependence of line parameters [203]. Here, a double power law (DPL),

$$\gamma_0(T) = c_1(\frac{T_0}{T})^{n_1} + c_2(\frac{T_0}{T})^{n_2}, \tag{88}$$

was used to fit the temperature dependence of the pressure-induced broadening parameter (γ_0), where c_1, n_1, c_2 and n_2 are constants to be determined. A non-linear least-squares fit is conducted to determine the c_1, n_1, c_2 and n_2 coefficients and root mean square error,

$$RMSE = \sqrt{\frac{\sum_{i=1}^{n}[Y_i(\text{data}) - Y_i(\text{model})]^2}{n}}, \tag{89}$$

was calculated. The n_1 and n_2, temperature-dependence coefficients, as well as c_1 and c_2 coefficients, for the line broadening parameter, obtained from both Voigt and qsDHC+LM line profiles, were determined for both P and R branches in the ν_3 band of methane. Figure 49 shows the pressure-induced broadening coefficients (γ_0) for the selected R(0), R(1), R(6) $A_1 - A_2$, P(4) $F_1 - F_2$, P(5) $F_2 - F_1$, and P(7) $F_1 - F_2$ lines, with associated DPL fit functions, in cm^{-1}/atm units versus temperature in kelvin. Overall, the calculated RMSE for the Voigt profile is in the same range as the qsDHC+LM lineshape profile. Coefficients of DPL for the selected lines are presented in Table 21.

In addition, the rotational dependence of pressure-induced broadening coefficients is analyzed for the P and R branches of the ν_3 band. The γ_0 coefficients calculated using both Voigt and qsDHC+LM line profiles are plotted versus rotational quantum number (J'') for 296 K, 463 K, 681 K, 894 K, and 1098 K, separately. Figure 50 (a-e) shows J dependence of γ_0 coefficients calculated using Voigt profile for the aforementioned temperature range respectively. To show the J dependence, a rotational

TABLE 21: Double power law coefficients for temperature dependence of broadening parameters from Voigt and non-Voigt profiles

Line	Voigt						non-Voigt			
	C_1	n_1	C_2	n_2	RMSE	C_1	n_1	C_2	n_2	RMSE
R(0)	-1.82081	-0.34687	2.81968	-0.10273	4.01×10^{-4}	-2.77052	1.88204	3.76893	1.36351	1.3×10^{-3}
R(1)	-1.15702	1.64141	2.15719	0.9940	9.71×10^{-4}	-0.36537	2.78139	1.36514	0.80986	8.99×10^{-4}
R(6) A_1–A_2	-4.40593	1.43234	5.40529	1.19718	7.47×10^{-4}	-1.98694	1.45239	2.98602	1.05258	8.31×10^{-4}
P(4) F_1–F_2	-1.04150	1.68325	2.04084	0.87757	3.5×10^{-4}	-0.55498	2.14591	1.55463	0.76998	9.41×10^{-4}
P(5) F_2–F_1	-3.68683	1.46379	4.68563	1.15923	5.94×10^{-4}	-1.71655	1.74237	2.71552	1.05555	6.78×10^{-4}
P(7) F_1–F_2	3.55567	1.19186	-2.55636	1.64838	4.49×10^{-4}	-0.45517	2.64118	1.45489	0.83086	9.47×10^{-4}

quantum number index m is used, where $m = -J$ for the P branch, and $m = J + 1$ for the R branch. J dependence of γ_0 for each A, E and F symmetry components within each J manifold are distinguished to better illustrate the J dependence for each symmetry component. The scatter among values for the same symmetry at a single J value shows differences for transitions between different sub-levels. For instance, P(8) F_1–F_2 line has a different line broadening than the P(8) F_2–F_1 line. Error bars are also included for γ_0 in Figure 50. The fit errors are $< 1\%$ for γ_0 values with the exception of a few lines mostly at higher Js.

Overall, γ_0 shows a decreasing trend with increasing m for all temperatures. γ_0 values are distributed between ($\sim$ 0.085 – $\sim$ 0.065) cm^{-1}/atm, ($\sim$ 0.075 – $\sim$ 0.06) cm^{-1}/atm, ($\sim$ 0.065 – $\sim$ 0.045) cm^{-1}/atm, ($\sim$ 0.05 – $\sim$ 0.035) cm^{-1}/atm and ($\sim$ 0.045 – $\sim$ 0.02) cm^{-1}/atm at 296 K, 463 K, 681 K, 894 K, and 1098 K temperatures, respectively. This shows a decrease of 20 to 30% for γ_0 with increasing J for temperatures up to 894 K and a 40% decrease in γ_0 with increasing J for 1098 K.

The symmetry dependence of γ_0 parameters show a weaker line broadening for E symmetry compared to the values corresponding to A and F symmetries, similar to previous observations [196, 200]. Figure 50 (f) also shows the J dependence of γ_0 values, averaged over each J manifold to remove the symmetry dependence, which also shows a decreasing trend with increasing m.

In addition to γ_0 coefficients determined by the Voigt profile, the qsDHC+LM line profile was also used to obtain γ_0 values. A comparison between parameters determined using Voigt and non-Voigt line profiles is useful. Similarly, rotational and symmetry dependences of γ_0 parameters determined using qsDHC+LM profile were analyzed. J dependence of γ_0 parameters for the P and R branches of methane obtained using qsDHC+LM profile for 296 K, 463 K, 681 K, 894 K, and 1098 K is presented in Figure 51 (a-e) respectively. Similar to the case for Voigt profile, γ_0 parameters decrease by increasing m. Also, similarly, E symmetry shows the greatest decrease in γ_0 values with increasing J. It worth noting that, in this case, decrease of γ_0 values with m is slightly different for the P and R branch (see Figure 51). For the P branch, majority of γ_0 values are distributed between ($\sim$ 0.085 – $\sim$ 0.065) cm^{-1}/atm, ($\sim$ 0.075 – $\sim$ 0.055) cm^{-1}/atm, ($\sim$ 0.06 – $\sim$ 0.045) cm^{-1}/atm, ($\sim$ 0.05 – $\sim$ 0.035) cm^{-1}/atm and ($\sim$ 0.047 – $\sim$ 0.025) cm^{-1}/atm at 296 K, 463 K, 681 K, 894 K, and 1098 K temperatures, respectively. This shows a decrease of 18 to 25%

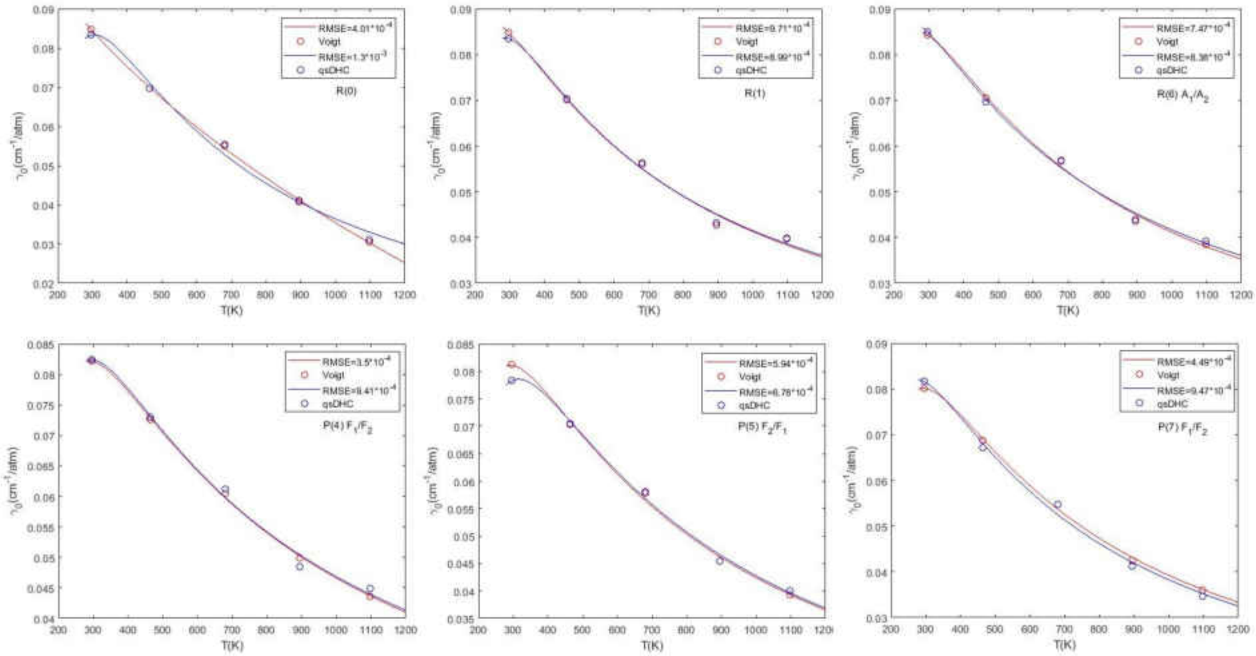

FIG. 49: Double power law fit to the broadening parameters for the selected R(0), R(1) and R(6) A_1–A_2, P(4) F_1–F_2, P(5) F_2–F_1 and P(7) F_1–F_2 lines, for the Voigt and non-Voigt profiles. Red and blue circles show γ_0 for the Voigt and non-Voigt profiles, respectively. Red and blue solid lines are DPL fits for the Voigt and non-Voigt profiles, respectively.

from the maximum γ_0 value for the first three temperatures, and about 40% for the last two temperatures. γ_0 values for the R branch are slightly more scattered and the decrease in higher Js is steeper, compared to the P branch. The majority of γ_0 values for the R branch are distributed between ($\sim$ 0.085 – $\sim$ 0.045) cm^{-1}/atm, ($\sim$ 0.075 – $\sim$ 0.055) cm^{-1}/atm, ($\sim$ 0.06 – $\sim$ 0.03) cm^{-1}/atm, ($\sim$ 0.05 – $\sim$ 0.035) cm^{-1}/atm and ($\sim$ 0.047 – $\sim$ 0.02) cm^{-1}/atm at 296 K, 463 K, 681 K, 894 K, and 1098 K temperatures, respectively. This shows a decrease of 25 to 45% from the maximum γ_0 value for the R branch for the majority of lines. Note that there are a few lines with higher rotational quantum numbers of $|m| \geq 14$ that show a steeper decrease in γ_0 values than 45%. In comparison to the Voigt profile, overall, the obtained γ_0 by qsDHC+LM profile shown in Figure 51 (a-e) shows a similar decreasing trend of γ_0 with increasing $|m|$ (see Figure 50 (a-e)). Figure 51 (f) shows γ_0 values averaged over symmetry for each J manifold which have a decreasing trend by increasing $|m|$. Compared to Figure 50 (f), the γ_0 values averaged over symmetry and obtained by qsDHC+LM profile have closer values for each J for the last two temperatures of

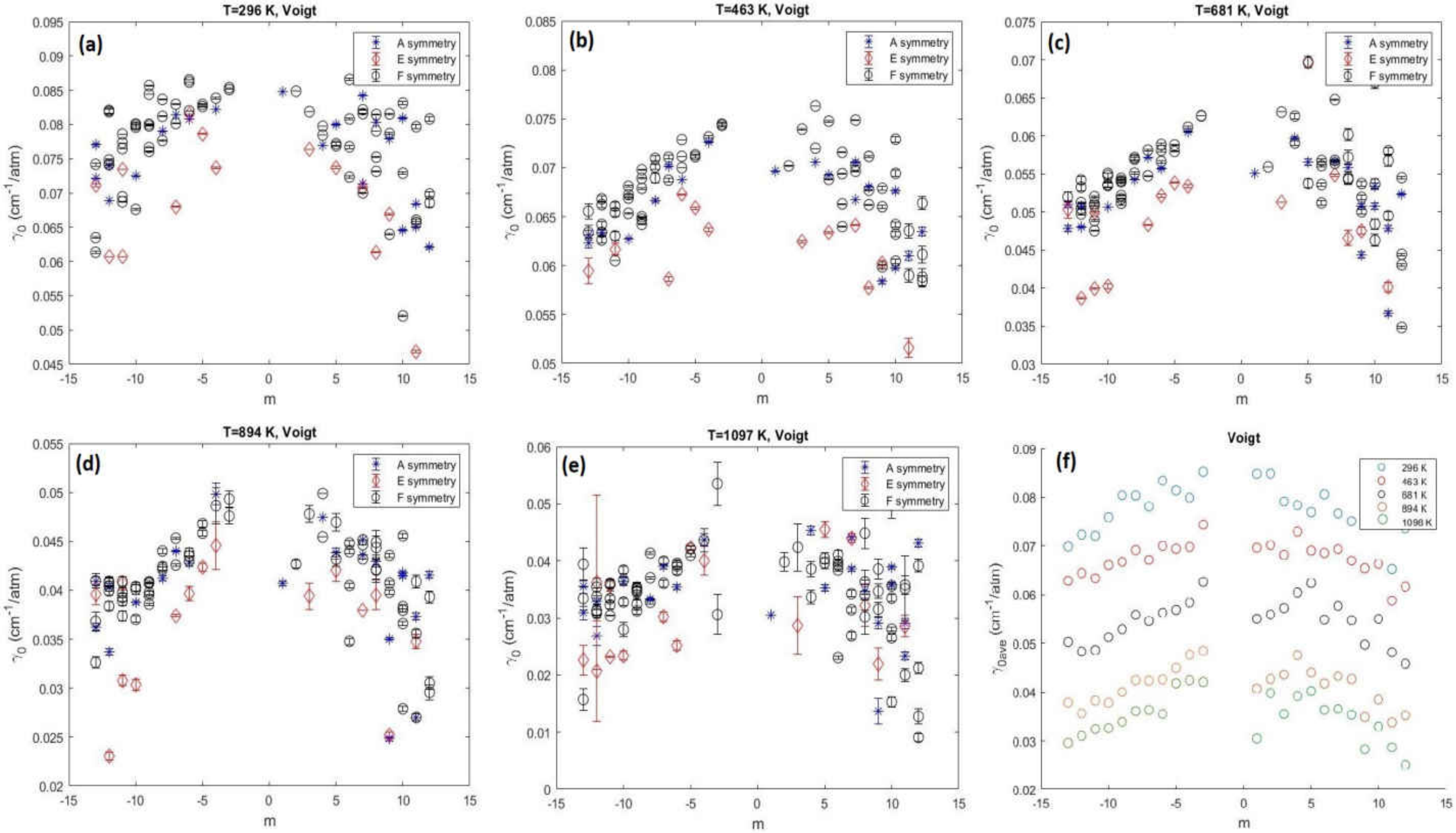

FIG. 50: Variation of pressure-induced broadening coefficients calculated by the Voigt profile with rotational quantum number index m. (m=−J for P branch and m=J+1 for R branch) at 296 K, 463 K, 681 K, 894 K, and 1098 K. The broadening parameters are separated to A, E and F symmetries. The lines with E symmetry show weakest broadening.

894 K and 1098 K (see Figure 51 (f)).

Pressure-induced line shift (δ_0)

Pressure-induced shifts are another consequence of collisions (H_2 in this work). Pressure shift parameters were determined by performing a multi-spectrum non-linear least squares fitting procedure, used in this study for 296 K, 463 K, 681 K, 894 K, and 1098 K respectively. In addition, temperature-dependence of pressure-induced shifts (δ_0) are studied. Conventionally, temperature-dependence of δ_0 is expressed either in the power law form of

$$\delta_0(T) = \delta_0(T_0)(\frac{T_0}{T})^q, \tag{90}$$

or in the linear form of

$$\delta_0(T) = \delta_0(T_0) + \delta'(T - T_0), \tag{91}$$

where $\delta_0(T)$ is the pressure shift at temperature T, $\delta_0(T_0)$ is the pressure shift at reference temperature T_0, q and δ' are the pressure shift coefficients for the power and linear forms, respectively.

The temperature-dependence of δ_0 obtained by both Voigt and qsDHC+LM profiles was studied. A linear increase of δ_0 values was observed for the lower temperatures 296 K, 463 K, and 681 K, however there is a deviation from a linear trend at 894 K and 1098 K. A linear form of δ_0 temperature-dependence was adopted but did not include data for 894 K and 1098 K. A linear fit of first three temperatures was carried out to determine the temperature-dependence of pressure shift for both Voigt and qsDHC+LM profiles. Figure 52 shows a linear fit for the temperature-dependence of δ_0 with a few selected lines of P(7) F_1–F_2, P(9) A_2–A_1, and R(6) A_1–A_2 for both Voigt and qsDHC+LM profiles with corresponding δ', which shows an increasing linear trend of δ_0 values with temperature. Table 22 lists a set of selected CH_4 lines with their corresponding temperature-dependence parameters (δ') for the Voigt and qsDHC profiles. For the lines presented in Table 22, δ' coefficients range between 0.66×10^{-5} and 2.4×10^{-5} with an average value of 1.51×10^{-5} for the Voigt profile, and between 0.60×10^{-5} and 1.66×10^{-5} with an average value of 1.09×10^{-5} for the non-Voigt profile.

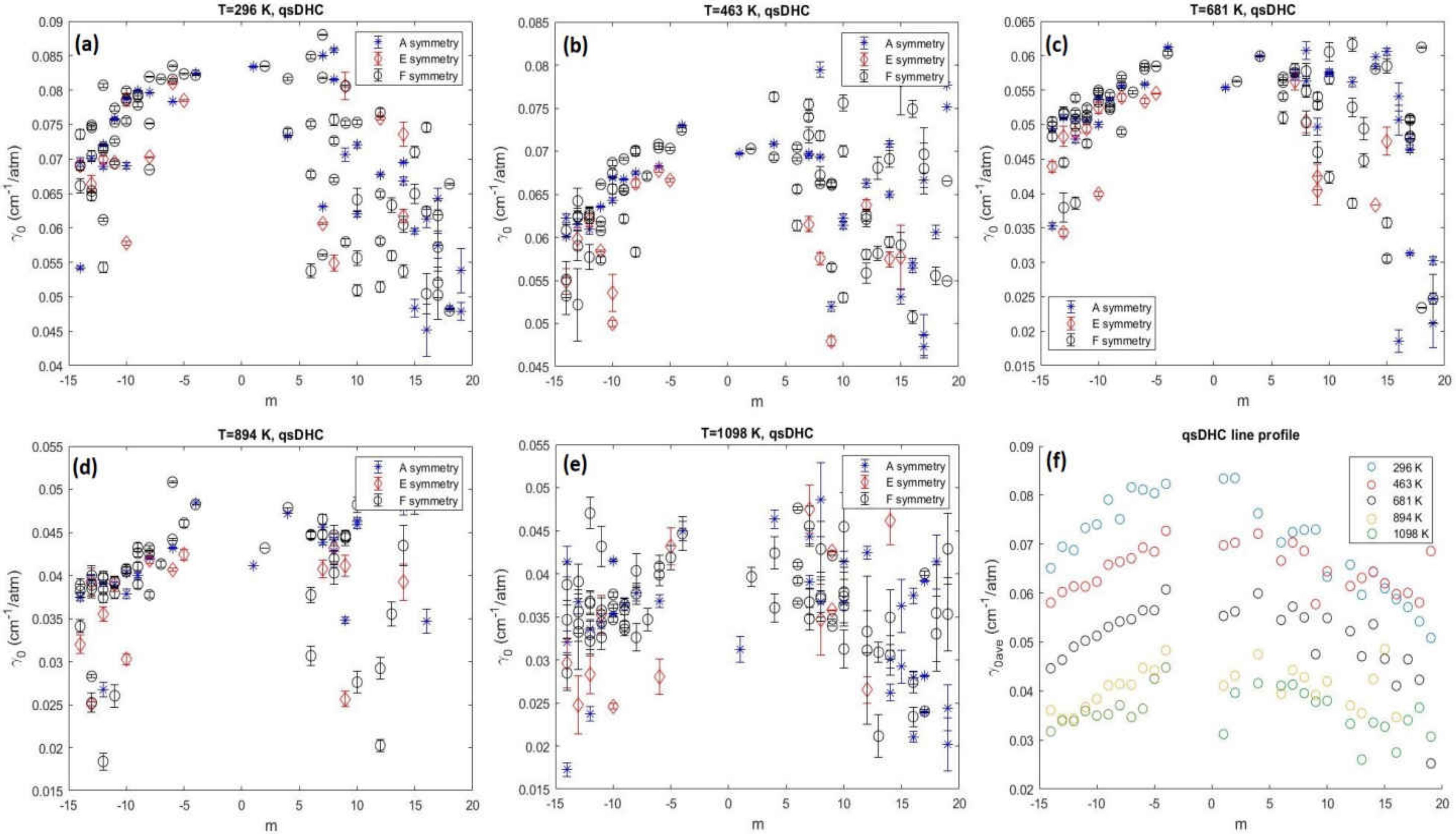

FIG. 51: Variation of pressure-induced broadening coefficients calculated by the non-Voigt profile with rotational quantum number index m. (m=−J for P branch and m=J+1 for R branch) at 296 K, 463 K, 681 K, 894 K, and 1098 K. The broadening parameters are separated to A, E and F symmetries. The lines with E symmetry show weakest broadening.

TABLE 22: Temperature-dependence parameter for pressure shift for Voigt and non-Voigt profiles

Voigt			non-Voigt		
Line	δ'	error	Line	δ'	error
P(13) E[a]	1.09E-05	4.71E-06	P(14) F_1	1.19E-05	4.27E-06
P(12) F_2	3.17E-05	1.16E-05	P(13) E	1.02E-05	2.32E-05
P(12) A_2	1.81E-05	1.79E-06	P(13) A_1	1.31E-05	2.92E-05
P(12) E	5.25E-06	6.57E-06	P(13) F_1	1.13E-05	8.23E-06
P(12) F_1	1.34E-05	4.47E-06	P(12) F_1	1.35E-05	3.95E-06
P(12) F_2	1.19E-05	3.04E-06	P(12) F_2	8.33E-06	3.83E-06
P(11) E	1.07E-05	4.23E-06	P(11) E	1.02E-05	1.15E-06
P(11) F_2	1.98E-05	6.07E-06	P(11) F_1	1.18E-05	5.51E-06
P(11) F_1	1.13E-05	1.20E-06	P(11) F_2	1.59E-05	1.26E-05
P(11) F_2	1.39E-05	6.59E-06	P(11) A_2	1.03E-05	1.97E-06
P(11) A_2	1.06E-05	3.79E-06	P(10) E	7.21E-06	3.65E-06
P(11) F_1	5.07E-06	3.55E-07	P(10) A_1	9.19E-06	2.76E-06
P(10) E	9.67E-06	4.49E-06	P(9) A_1	1.59E-05	6.07E-06
P(10) F_2	1.62E-05	1.06E-06	P(8) F_1	1.67E-05	6.49E-06
P(10) A_1	9.91E-06	4.56E-06	P(8) F_2	1.14E-05	5.10E-06
P(10) F_1	1.26E-05	3.85E-06	P(8) A_1	6.22E-06	4.30E-06
P(10) F_2	1.24E-05	1.85E-06	P(6) F_1	1.35E-05	7.53E-06
P(10) A_2	1.09E-05	1.28E-06	P(6) F_2	1.67E-05	2.07E-06
P(10) F_1	1.71E-05	3.57E-06	P(6) A_2	1.31E-05	3.14E-06
P(9) F_1	1.76E-05	1.09E-05	P(6) F_1	8.19E-06	3.90E-07
P(9) A_1	1.47E-05	8.96E-07	P(5) E	8.28E-06	1.97E-05
P(9) F_2	1.28E-05	5.50E-06	P(5) F_2	1.14E-05	3.44E-06
P(9) F_1	8.14E-06	5.59E-06	P(5) F_1	1.66E-05	6.35E-06
P(9) F_2	1.31E-05	3.10E-06	P(4) F_2	8.58E-06	8.90E-06
P(9) F_1	9.09E-06	3.41E-06	P(4) F_1	1.43E-05	5.60E-06
P(8) F_2	6.90E-06	2.85E-07	P(4) A_1	8.70E-06	4.72E-06
P(8) F_1	1.53E-05	3.03E-06	R(3) A_2	6.87E-06	1.49E-07
P(8) F_2	1.08E-05	4.61E-06	R(3) F_1	1.83E-05	7.09E-06
P(8) F_1	9.55E-06	4.54E-06	R(5) F_1	5.96E-06	2.63E-06
P(8) A_1	7.78E-06	4.05E-06	R(6) A_2	7.10E-06	5.72E-06

TABLE 22 – continued from previous page

Voigt			non-Voigt		
P(7) E	1.28E-05	5.36E-06	R(7) F_1	1.25E-05	1.45E-06
P(7) F_2	1.28E-05	1.36E-06	...	...	...
P(7) A_2	1.08E-05	3.29E-06	...	...	...
P(7) F_1	1.07E-05	3.52E-06	...	...	...
P(6) F_2	1.66E-05	5.65E-06	...	...	...
P(6) A_2	1.36E-05	1.21E-06	...	...	...
P(6) F_2	1.04E-05	2.44E-06	...	...	...
P(6) E	8.06E-06	5.33E-06	...	...	...
P(5) F_1	7.85E-06	2.12E-06	...	...	...
P(5) E	9.53E-06	2.52E-06	...	...	...
P(5) F_2	1.32E-05	4.66E-07	...	...	...
P(5) F_1	1.12E-05	2.25E-06	...	...	...
P(4) F_2	9.91E-06	3.39E-06	...	...	...
P(4) E	1.05E-05	2.16E-06	...	...	...
P(4) F_1	1.27E-05	1.06E-06	...	...	...
P(4) A_1	9.41E-06	3.73E-07	...	...	...
P(3) A_2	1.06E-05	4.11E-06	...	...	...
P(3) F_1	1.22E-05	4.64E-06	...	...	...
R(0)	5.58E-06	1.86E-06	...	...	...
R(1) F_1	5.67E-06	6.39E-08	...	...	...
R(3) F_1	8.96E-06	2.12E-06	...	...	...
R(5) F_2	7.53E-06	5.94E-06	...	...	...
R(5) F_1	7.53E-06	5.94E-06	...	...	...
R(6) A_2	7.29E-06	5.96E-06	...	...	...
R(7) F_2	3.19E-06	1.47E-05	...	...	...
R(8) F_1	1.65E-05	6.39E-06	...	...	...
R(9) A_1	1.57E-05	1.01E-05	...	...	...

[a] Symmetry is for the lower rotational level.

Additionally, J dependence of δ_0 parameters obtained using both Voigt and non-Voigt profiles were analyzed. Symmetry dependence was also considered in the analysis. Rotational dependence of δ_0 values determined using Voigt profile is shown in

Figure 53 (a-e).

The J dependence of δ_0 parameter shows a different trend compared to γ_0. In the P branch, for the majority of lines, δ_0 values are less scattered and vary slowly with $|m|$. δ_0 values are distributed around ∼ −0.005 cm^{-1}/atm, (∼ − 0.004 – ∼ − 0.002) cm^{-1}/atm, ∼ −0.001 cm^{-1}/atm, (∼ − 0.0005 – ∼ − 0.002) cm^{-1}/atm, and (∼ − 0.002 – ∼ 0.002) cm^{-1}/atm for 296 K, 463 K, 681 K, 894 K, and 1098 K temperatures, respectively. Note that there are a few outliers from these limits especially at 1098 K.

In the R branch, δ_0 are more scattered at each J and we observe significant variation in magnitude and sign of δ_0 values with increasing J (see Figure 53). The majority of these values with exception of a few outliers are distributed between (∼ − 0.015 – ∼ 0.015) cm^{-1}/atm, (∼ − 0.006 – ∼ 0.006) cm^{-1}/atm, (∼ − 0.005 – ∼ 0.005) cm^{-1}/atm and (∼ − 0.002 – ∼ 0.004) cm^{-1}/atm for 296 K, 463 K, 681 K, 894 K, and 1098 K, respectively. Also note that, δ_0 values for the P branch with the exception of 1098 K have negative values.

Similarly, the rotational dependence analysis of δ_0 values obtained using non-Voigt profile was studied which is presented in Figure 54, and shows a similar pattern of rotational dependence to the case of the Voigt profile. In the P branch, δ_0 values are less scattered and the majority of δ_0 values are distributed between (∼ − 0.004 – ∼ − 0.006) cm^{-1}/atm, (∼ − 0.007 – ∼ − 0.003) cm^{-1}/atm, ∼ − 0.002 cm^{-1}/atm, (∼ − 0.002 – ∼ − 0.0005) cm^{-1}/atm, and (∼ − 0.005 – ∼ − 0.0005) cm^{-1}/atm for 296 K, 463 K, 681 K, 894 K, and 1098 K, respectively. Note that all the δ_0 values for the P branch have negative values. The majority of these values in the R branch, with exception of a few outliers are distributed between (∼ − 0.013 – ∼ 0.01) cm^{-1}/atm, (∼ − 0.01 – ∼ 0.005) cm^{-1}/atm, (∼ − 0.01 – ∼ 0.01) cm^{-1}/atm, and (∼ − 0.006 – ∼ 0.006) cm^{-1}/atm, (∼ − 0.002 – ∼ 0.006) cm^{-1}/atm for 296 K, 463 K, 681 K, 894 K, and 1098 K temperatures, respectively (see Figure 54). In comparison, δ_0 values determined for the non-Voigt profile tend be slightly more scattered than those calculated using Voigt profile, especially in the R branch.

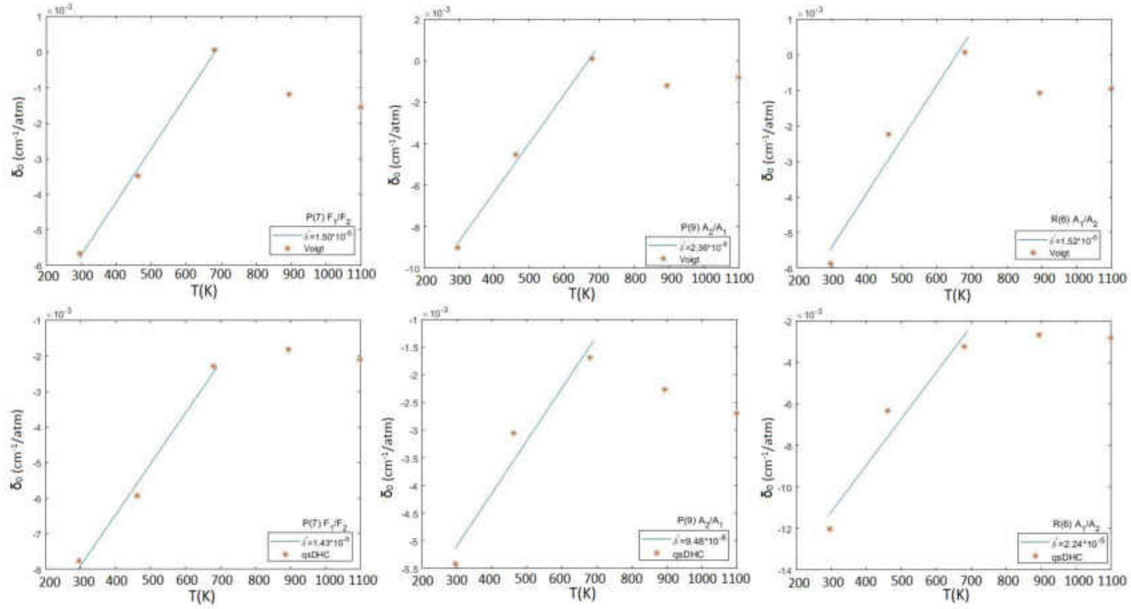

FIG. 52: Temperature-dependence of pressure shift (δ_0) calculated using Voigt (upper panel) and non-Voigt (lower panel). The red asterisk show the line shift at each temperature and the solid blue line is the linear fit for the first three temperatures. The temperature dependent parameter (δ') for the selected P(7) F_1–F_2, P(9) A_2–A_1 and R(6) A_1–A_2 are 1.5×10^{-5}, 2.36×10^{-5} and 1.52×10^{-5} respectively for the Voigt profile and 1.48×10^{-5}, 9.48×10^{-6} and 2.24×10^{-5} respectively for non-Voigt profile.

Speed dependent pressure shift (δ_2) and line mixing parameter (Y)

The use of qsDHC+LM line profile also enables determination of the speed dependence of the pressure shift parameter (δ_2). In this work, we determined δ_2 for the non-Voigt profile at each temperature for the number of CH_4 lines. Also, the temperature-dependence of δ_2 values were analyzed. In the case of speed dependent pressure shift, a single power law was a better fit of temperature dependence than linear form. A power law relation of

$$\delta_2(T) = \delta_2(T_0)(\frac{T_0}{T})^q, \tag{92}$$

shows the temperature dependence of δ_2, where $\delta_2(T)$ is the speed dependent pressure shift at temperature T, $\delta_2(T_0)$ is the speed dependent pressure shift at reference temperature, and q is the temperature-dependence coefficient. Figure 55 shows temperature-dependence of δ_2 in logarithmic scale, for the selected lines of

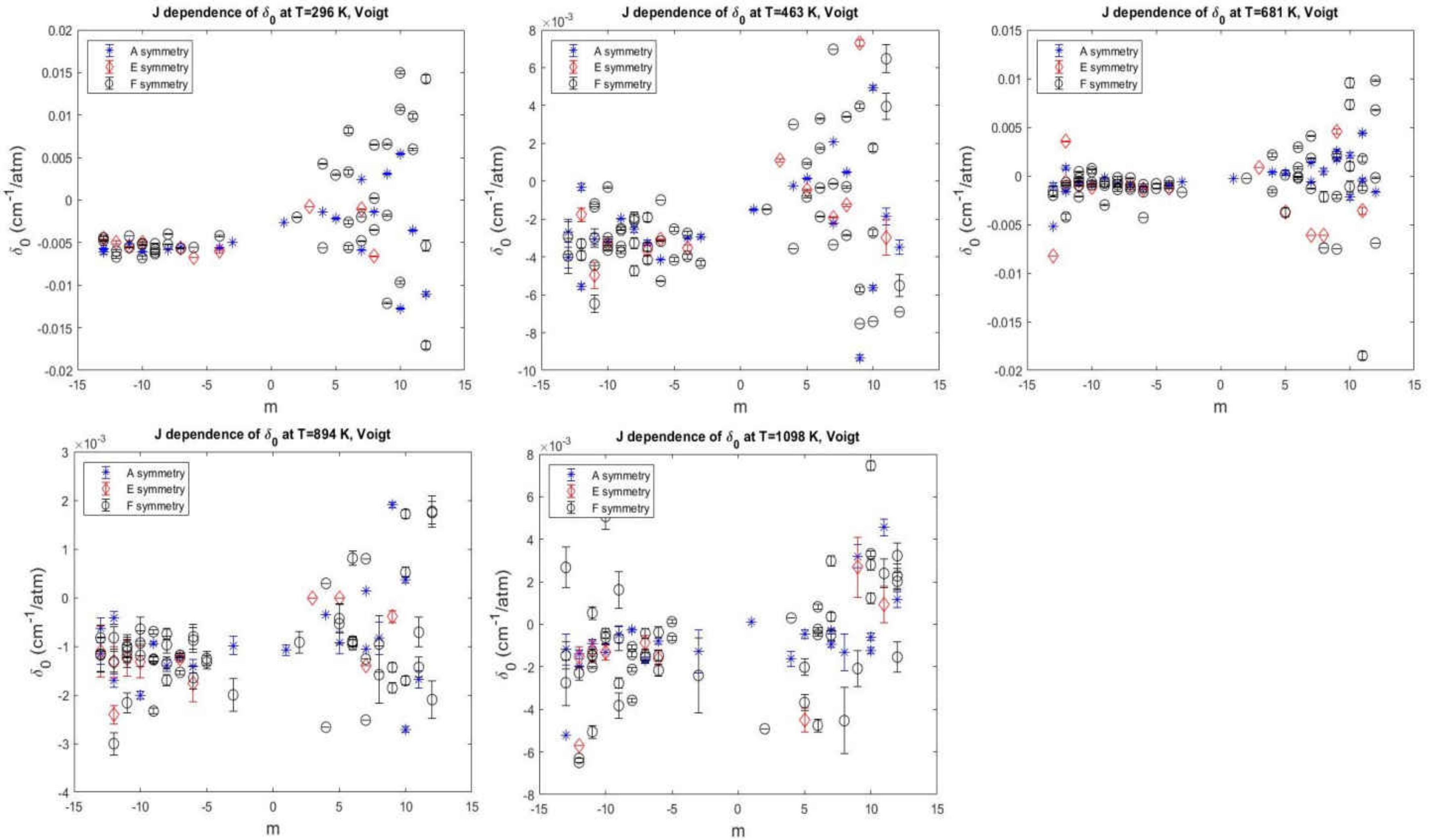

FIG. 53: Variation of pressure shift coefficients calculated by the Voigt profile with rotational quantum number index m. (m=−J for P branch and m=J+1) for R branch at 296 K, 463 K, 681 K, 894 K, and 1098 K. The shift parameters are separated to A, E and F symmetries.

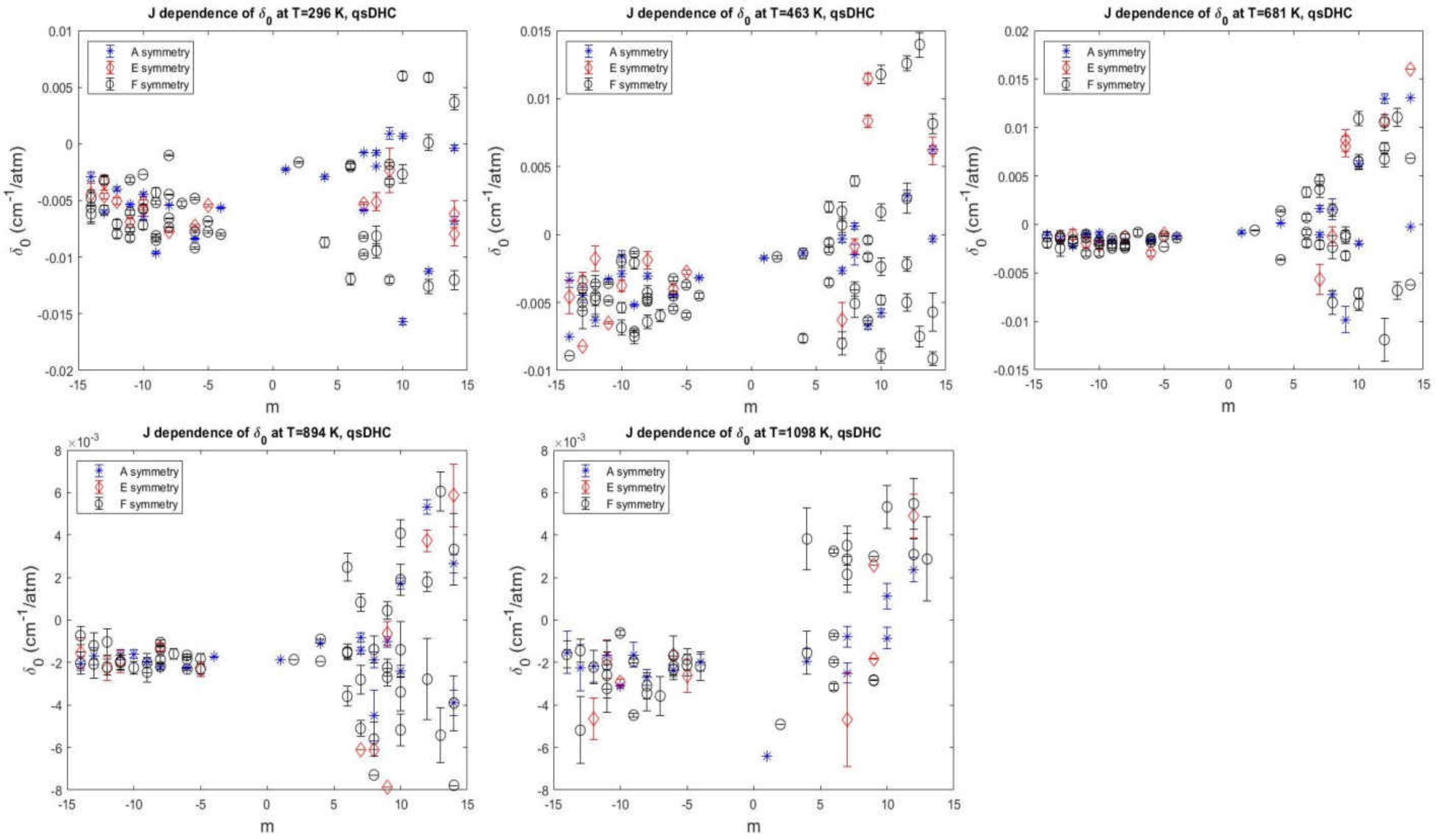

FIG. 54: Variation of pressure shift coefficients calculated by the non-Voigt profile with rotational quantum number index m. (m=−J for P branch and m=J+1) for R branch at 296 K, 463 K, 681 K, 894 K, and 1098 K. The shift parameters are separated to A, E and F symmetries.

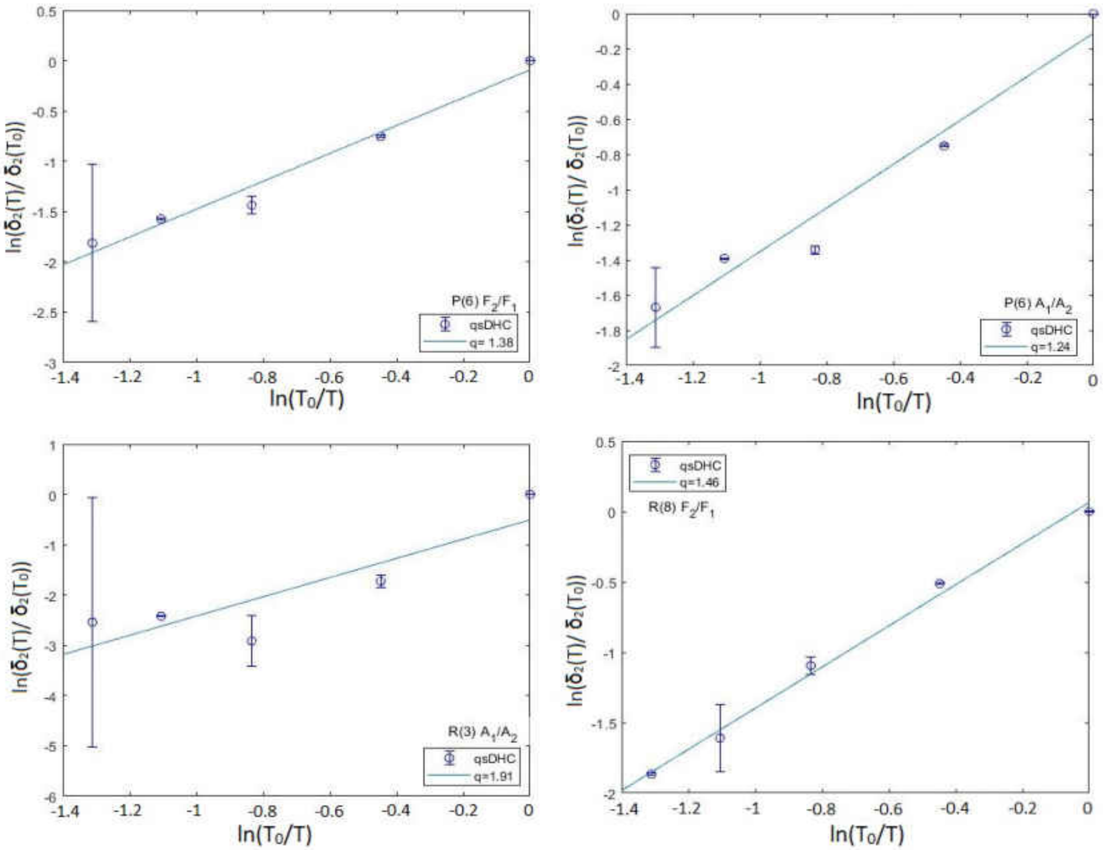

FIG. 55: Temperature-dependence of speed dependent pressure shift (δ_2) calculated using the non-Voigt profile. The blue circles show δ_2 values at each temperature. A linear fit (solid line) is done to determine temperature dependent parameter (q) for the selected P(6) F_2–F_1, P(6) A_1–A_2 and R(3) A_1–A_2 and R(8) F_2–F_1 that are 1.38, 1.24, 1.91 and 1.46 respectively.

P(6) F_2–F_1, P(6) A_1–A_2, R(3) A_{12}, and R(8) F_2–F_1. A linear fit was performed for these lines and temperature-dependence parameters of 1.38, 1.24, 1.91, and 1.46 were determined from the fit. Table 23 lists a number of selected CH_4 lines and the corresponding determined temperature-dependence coefficients (q) for δ_2 values.

TABLE 23: Temperature-dependence parameters of speed dependent pressure shift for non-Voigt profile

Line	q
P(14) F_1[a]	1.61342
P(13) F_2	1.31566
P(13) A_1	1.24383
P(12) A_2	1.64762
P(12) F_1	1.44440
P(12) F_2	1.03710
P(11) F_1	0.57621
P(11) F_2	1.93763
P(11) A_2	0.62059
P(10) E	0.54125
P(10) F_1	1.64767
P(9) A_1	1.11652
P(8) F_2	0.61437
P(6) F_1	1.38613
P(6) A_2	1.24361
P(5) F_2	0.70660
P(4) F_1	1.10814
R(3) A_2	1.91359
R(5) F_1	1.10459
R(7) F_2	0.6499
R(8) F_1	1.46114

[a] Symmetry is for the lower rotational level.

At higher pressures the line mixing that results from the coupling between neighboring lines [209, 210] becomes important. qsDHC+LM profile accounts for Rosenkranz first order line mixing. The line mixing parameters were also included in the multi-spectrum fit. Only neighboring lines were considered in line mixing and the symmetry selection rule were applied in which only $A_1 \leftrightarrow A_2$, $F_1 \leftrightarrow F_2$, and $E \leftrightarrow E$ can couple [209]. The calculated line mixing parameter with corresponding lines at each temperature are presented in Table 24.

TABLE 24: First order Rosenkranz line mixing coefficients (Y) for each temperature with corresponding errors

Line\Y(T)	Y(296)	Y(463)	Y(681)	Y(894)	Y(1098)
P(14) F_1	0.0793(0.0418)	–	–	–	–
P(14) F_1	–	–	–	0.0569(0.0418)	–
P(14) F_2	–	0.8375(0.1179)	–	–	–
P(13) F_2	−0.0691(0.0105)	0.1307(0.0397)	0.0883(0.0323)	0.086(0.0423)	–
P(13) F_1	−0.1246(0.0098)	0.278(0.042)	–	–	–
P(13) F_2	0.0504(0.0116)	–	–	–	–
P(13) F_1	–	0.5301(0.0502)	–	–	–
P(13) F_2	−0.0548(0.0171)	−0.0644(0.0463)	–	–	0.1761(0.069)
P(12) F_1	0.0424(0.0089)	–	–	−0.0451(0.0279)	−0.2341(0.0401)
P(12) F_1	0.0285(0.0111)	–	0.0416(0.0196)	–	–
P(11) F_2	−0.2291(0.0082)	0.1249(0.0028)	–	–	–
P(11) F_1	0.0628(0.0042)	0.0207(0.0028)	–	–	–
P(11) F_2	0.108(0.0039)	0.0922(0.0092)	–	–	–
P(11) F_1	–	–	–	0.0839(0.0278)	–
P(10) F_1	0.0223(0.0086)	−0.0665(0.0132)	0.0412(0.0137)	0.078(0.0236)	–
P(10) F_2	0.0163(0.0112)	0.1272(0.0169)	0.0902(0.0142)	0.0383(0.0235)	−0.0699(0.0071)
P(9) F_1	−0.3236(0.0036)	–	−0.0217(0.0134)	−0.0701(0.0207)	0.0996(0.0477)
P(9) A_1	–	0.0179(0.0027)	–	–	–
P(9) F_1	0.0927(0.004)	−0.1517(0.0045)	–	0.0257(0.0226)	−0.1817(0.0449)
P(9) E	−0.065(0.0058)	–	0.0551(0.0222)	–	–
P(9) F_2	0.3579(0.0212)	−0.1655(0.0288)	0.0861(0.0001)	–	0.1584(0.0062)
P(9) F_1	−0.2582(0.0227)	0.2475(0.0294)	0.006(0.0001)	−0.3412(0.0315)	–
P(8) F_2	0.195(0.0013)	–	0.0538(0.0096)	–	–
P(8) E	0.0154(0.0017)	0.2085(0.0156)	0.0916(0.0141)	–	–
P(8) F_1	−0.1041(0.0012)	–	−0.032(0.0083)	−0.0656(0.0077)	0.0472(0.0416)
P(8) F_2	0.0607(0.0011)	0.0562(0.0081)	0.054(0.0082)	0.0139(0.0076)	0.1695(0.0229)
P(7) F_2	0.1392(0.0066)	−0.0323(0.0148)	0.0955(0.015)	0.1701(0.0167)	–
P(7) F_1	−0.095(0.0069)	0.1352(0.0161)	0.0238(0.0158)	–	0.1952(0.0507)
P(6) F_1	0.3076(0.0025)	0.1539(0.0054)	0.0602(0.0105)	–	–
P(6) F_2	−0.1195(0.0021)	–	−0.0186(0.0096)	–	–
P(5) F_2	−0.0439(0.0017)	−0.0246(0.0045)	−0.0296(0.0012)	–	–
P(5) F_1	0.0434(0.0017)	0.0914(0.0048)	0.0454(0.0012)	–	–

Line\Y(T)	Y(296)	Y(463)	Y(681)	Y(894)	Y(1098)
P(4) F_2	–	–	–	0.1072(0.0001)	–
P(4) F_1	–	–	–	0.058(0.0001)	–
R(3) F_2	–	0.1296(0.0071)	–	–	−0.1439(0.0558)
R(3) F_1	–	–	0.0135(0.0042)	−0.1831(0.0001)	–
R(5) F_1	–	–	–	0.0515(0.0174)	–
R(5) E	–	0.1439(0.01)	–	–	–
R(5) F_2	−0.3189(0.0162)	0.0585(0.0078)	–	–	–
R(5) F_1	0.3035(0.0161)	–	0.0686(0.0141)	−0.0314(0.0163)	–
R(6) F_1	–	0.8595(0.031)	–	0.1337(0.0267)	–
R(6) F_2	–	–	–	–	−0.1439(0.0372)
R(7) F_2	0.1182(0.0051)	0.6121(0.0767)	–	0.0948(0.0437)	–
R(7) F_1	–	−0.5196(0.0863)	–	–	–
R(8) F_2	0.0153(0.0049)	0.0627(0.009)	0.0314(0.0253)	–	0.0297(0.0006)
R(8) E	–	0.0918(0.0063)	0.1853(0.0207)	–	–
R(8) A_1	0.081(0.0052)	–	–	–	–
R(9) F_2	–	0.1671(0.0131)	–	–	–
R(13) F_1	0.1282(0.0165)	0.0425(0.0307)	–	–	–

Symmetry is for the lower rotational level.

Recent studies

One recent study on the CH_4 line broadening by H_2 at high temperature was carried out by Garib-Nejad et al. [193]. In their work, they determined γ_0 and δ_0 values for the P branch for three different pressures of H_2 at three temperatures of 300 K, 500 K, and 700 K. They reported γ_0 and δ_0 values, averaged over temperatures and J quantum numbers. In contrast, we measured CH_4 broadening parameters for five different pressures of H_2 at five different temperatures ranging from 296 K to 1098 K. The resulting γ_0 values averaged over temperature range of 296 K to 894 K, ranges from 0.067 cm^{-1}/atm for J=3–13 which is in agreement with the γ_0 values averaged over temperature and J from 0.067 cm^{-1}/atm to 0.053 cm^{-1}/atm, reported by Garib-Nejad et al. [193] for the same rotational quantum number range.

Summary and conclusions

Spectra of CH_4 for the ν_3 band at five different 296 K, 463 K, 681 K, 894 K, and 1098 K temperatures were recorded using a high resolution (0.01 cm^{-1}) Fourier transform IR spectrometer. Five different pressures, 0 Torr, 50 Torr, 150 Torr, 240 Torr, 320 Torr and 400 Torr of H_2 were used at each temperature. Transmission spectra of the ν_3 CH_4 band were obtained by correcting for the cell and CH_4 emission. The transmission spectra were calibrated using the HITRAN 2012 [41] database. Multispectrum least squares fits of CH_4 lines were carried out, at different H_2 pressures for each temperature, using Voigt and Hartmann–Tran lineshapes.

Additionally, the temperature-dependence of the γ_0, δ_0, and δ_2 parameters was also determined. Finally, the rotational dependence of pressure-induced broadening and shifting coefficients was studied. The results show a significant J dependence of γ_0 coefficients. J dependence of δ_0 coefficients are different in the P and R branches. The δ_0 values are less scattered in the P branch compared to the R branch.

There are very few studies where the pressure-induced broadening and shift parameters at high temperatures are determined [193]. Our study provides a comprehensive set of pressure-induced broadening (γ_0) and shifting (δ_0) parameters, including speed dependence of the line shift (δ_2) and line mixing (Y) for both P and R branches at high temperatures. Our data is intended to contribute to the spectroscopic analysis of H_2-dominated hot exoplanets and brown dwarfs.

BIBLIOGRAPHY

[1] Larson HP, Infrared spectroscopic observations of the outer planets, their satellites, and the asteroids, *Ann Rev Astron Astrophys* 1980;18:43–75.

[2] Tinetti G, Encrenaz T, Coustenis A, Spectroscopy of planetary atmospheres in our Galaxy, *Astron Astrophys Rev* 2013;21:63.

[3] Bates BC, Kundzewicz ZW, Wu S, Palutikof JP. IPCC Technical Paper VI. *Eds. IPCC Secretariat, Geneva* 2008;210 pp.

[4] Jacob D J, Introduction to Atmospheric Chemistry, 2000, (Princeton University Press).

[5] Martins DK, Development of methods for measurement of biosphere-atmosphere exchange of carbon and nitrogen, Doctoral dissertation, 2009, (Purdue University),

[6] Hall M, McKemy D, Lee A, Coriolis Effect, [online] Available from: `https://climate.ncsu.edu/edu/Coriolis` (Accessed 9 February 2020), 2011.

[7] Steward B, Jacobs J, Alton S, How to read a weather map: beginners guide, [online] Available from: `http://www.nwclimate.org/guides/weather-charts-tutorial/` (Accessed 9 February 2020), 2017.

[8] Bönisch H, Engel A, Birner T, Hoor P, Tarasick DW, Ray EA, On the structural changes in the Brewer-Dobson circulation after 2000, *Atmos Chem Phys* 2011;11:3937.

[9] Henderson, FM, Lewis, AJ, Principles and Applications of Imaging Radar. Manual of Remote Sensing: Third edition, 1998, Volume 2 John Wiley and Sons, Inc., Somerset, NJ (United States).

[10] Hattori S, Danielache SO, Johnson MS, Schmidt JA, Kjærgaard HG, Toyoda S, Ueno Y, Yoshida N, Ultraviolet absorption cross sections of carbonyl sulfide isotopologues $OC^{32}S$, $OC^{33}S$, $OC^{34}S$ and $O^{13}CS$: isotopic fractionation in photolysis and atmospheric implications, *Atmos Chem Phys* 2011;11:10293.

[11] Lee KH, Li Z, Kim YJ, Kokhanovsky A, Atmospheric aerosol monitoring from satellite observations: a history of three decades, *Atmos Bio Env Mon* 2009, (Springer).

[12] Finlayson-Pitts BJ, Pitts Jr JN, Chemistry of the upper and lower atmosphere: theory, experiments, and applications, 1999, (Elsevier).

[13] Solar Occultation, [online] Available from: `http://www.ace.uwaterloo.ca/solar_occultation.php` (Accessed 9 February 2020).

[14] Bernath PF, McElroy CT, Abrams MC, Boone CD, Butler M, Camy-Peyret C, Carleer M, Clerbaux C, Coheur PF, Colin R, et al., Atmospheric Chemistry Experiment (ACE): mission overview, *Geophys Res Lett* 2005;32:15.

[15] Bernath PF, The Atmospheric Chemistry Experiment (ACE), *J Quant Spectrosc Radiat Transf* 2017;186:3–16.

[16] Boone CD, Nassar R, Walker KA, Rochon Y, McLeod SD, Rinsland CP, Bernath PF, Retrievals for the atmospheric chemistry experiment Fourier-transform spectrometer, *Appl Opt* 2005;44:7218–7231.

[17] Benedict M, Molecular structure and spectra, [online] Available from: `https://titan.physx.u-szeged.hu/~dpiroska/atmolfiz/molecular_structure_and_spectra.html` (Accessed 25 February 2020), 2011.

[18] Bernath PF, Spectra of Atoms and Molecules 2015, (Oxford University Press).

[19] Klein R, Rosmus P, Ab initio calculations of infrared transition probabilities in the electronic ground states of AlF and AlF^+, *Theoretica Chim Acta* 1984;66:21–29.

[20] Hanson RK, Spearrin RM, Goldenstein CS, Spectroscopy and optical diagnostics for gases, 2016, (Springer).

[21] Naylor DA, Gom BG, van der Wiel MH, Makiwa G, Astronomical imaging Fourier spectroscopy at far-infrared wavelengths, *Canad J Physics* 2013;91:870–878.

[22] Hollas JM, Modern spectroscopy. 2004, (John Wiley & Sons).

[23] Myhre G, Shindell D, Pongratz J, Anthropogenic and natural radiative forcing, 2014, (Cambridge University Press),

[24] Stocker TF, Qin D, Plattner GK, Tignor M, Allen SK, Boschung J, Nauels A, Xia Y, Bex V, Midgley PM, et al., Climate change 2013: The physical science basis, 2013, (Cambridge University Press).

[25] Brown AT, Volk CM, Schoebert MR, Boone CD, Bernath PF, Stratospheric lifetimes of CFC-12, CCl_4, CH_4, CH_3Cl and N_2O from measurements made by the Atmospheric Chemistry Experiment-Fourier Transform Spectrometer, *Atmos Chem Phys* 2013;13:14.

[26] Finlayson-Pitts BJ, Pitts Jr JN, Chemistry of the Upper and Lower Atmosphere: Theory, Experiments, and Applications, 1999, (Elsevier).

[27] Yung YL, Miller CE, Isotopic fractionation of stratospheric nitrous oxide, *Science* 1997;278:1778–1780.

[28] Schmidt JA, Johnson MS, Schinke R, Isotope effects in N_2O photolysis from first principles, *Atmos Chem Phys* 2011;11:8965.

[29] Semeniuk K, McConnell JC, Jin JJ, Jarosz JR, Boone CD, Bernath PF, N_2O production by high energy auroral electron precipitation, *J Geophys Res: Atmos* 2008;113:D16302.

[30] Sheese PE, Walker KA, Boone CD, Bernath PF, Funke B, Nitrous oxide in the atmosphere: First measurements of a lower thermospheric source, *Geophys Res Lett* 2016;43:2866–2872.

[31] Kaiser J, Röckmann T, Brenninkmeijer CAM, Complete and accurate mass spectrometric isotope analysis of tropospheric nitrous oxide, *J Geophys Res: Atmos* 2003;108:(D15):4476.

[32] Griffith DWT, Toon GC, Sen B, Blavier JF, Toth RA, Vertical profiles of nitrous oxide isotopomer fractionation measured in the stratosphere, *Geophys Res Lett* 2000;27:2485–2488.

[33] Griffith DWT, Parkes SD, Haverd V, Paton-Walsh C, Wilson SR, Absolute calibration of the intramolecular site preference of ^{15}N fractionation in tropospheric N2O by FT-IR spectroscopy, *Anal Chem* 2009;81:2227–2234.

[34] Snider DM, Venkiteswaran JJ, Schiff SL, Spoelstra J, From the ground up: global nitrous oxide sources are constrained by stable isotope values, *PloS one* 2015;10:3.

[35] Bernard S, Röckmann T, Kaiser J, Barnola JM, Fischer H, Blunier T, Chappellaz J, Constraints on N_2O budget changes since pre-industrial time from new firn air and ice core isotope measurements, *Atmos Chem Phys* 2006;6:493–503.

[36] Toyoda S, Kuroki N, Yoshida N, Ishijima K, Tohjima Y, Machida T, Decadal time series of tropospheric abundance of N_2O isotopomers and isotopologues in the Northern Hemisphere obtained by the long-term observation at Hateruma Island, Japan, *J Geophys Res:Atmospheres* 2013;118:3369–3381.

[37] Plieninger J, Clarmann TV, Stiller GP, Grabowski U, Glatthor N, Kellmann S, Linden A, Haenel, F, Kiefer M, Höpfner M, et al., Methane and nitrous oxide retrievals from MIPAS-ENVISAT, *Atmos Meas Tech* 2015;8:4657–4670.

[38] Xiong X, Maddy ES, Barnet C, Gambacorta A, Patra PK, Sun F, Goldberg M, Retrieval of nitrous oxide from Atmospheric Infrared Sounder: Characterization and validation, *J Geophys Res: Atmos* 2014;119:9107–9122.

[39] Roche AE, Kumer JB, Nightingale RW, Mergenthaler JL, Ely GA, Bailey PL, Massie ST, Gille JC, Edwards DP, Gunson MR, et al., Validation of CH_4 and N_2O measurements by the cryogenic limb array etalon spectrometer instrument on the Upper Atmosphere Research Satellite, *J Geophys Res: Atmos* 1996;101:9679–9710.

[40] Boone CD, Walker KA, Bernath PF, Version 3 retrievals for the atmospheric chemistry experiment Fourier transform spectrometer (ACE-FTS), *Appl Opt* 2013;10:103–127.

[41] Rothman LS, Gordon IE, Babikov Y, Barbe A, Benner DC, Bernath PF, Birk M, Bizzocchi L, Boudon V, Brown LR, et al., The HITRAN2012 molecular spectroscopic database, *J Quant Spectrosc Radiat Transf* 2013;130:4–50.

[42] Sheese PE, Boone CD, Walker KA, Detecting physically unrealistic outliers in ACE-FTS atmospheric measurements, *Atmos Meas Tech* 2015;8:741–750.

[43] Kaiser J, Engel A, Borchers R, Röckmann T, Probing stratospheric transport and chemistry with new balloon and aircraft observations of the meridional and vertical N_2O isotope distribution, *Atmos Chem Phys* 2006;6:3535–3556.

[44] Khalil MAK, Rasmussen RA. Global sources, lifetimes and mass balances of carbonyl sulfide (OCS) and carbon disulfide (CS_2) in the Earth's atmosphere. *Science* 1967;18:1805.

[45] Yousefi M, Bernath PF, Boone CD, Toon GC. Global measurements of atmospheric carbonyl sulfide (OCS), $OC^{34}S$ and $O^{13}CS$. *J Quant Spec Rad Trans* 2019;238:106554.

[46] Kettle AJ, Kuhn U, von Hobe M, Kesselmeier J, Andreae MO. Global budget of atmospheric carbonyl sulfide: Temporal and spatial variations of the dominant sources and sinks. *Geophys Res Lett* 2002;107:4658.

[47] Montzka SA, Aydin M, Battle M, Butler JH, Saltzman ES, Hall BD, Clarke AD, Mondeel D, Elkins JW. A 350-year atmospheric history for carbonyl sulfide inferred from Antarctic firn air and air trapped in ice. *Geophys Res Lett* 2004;109:D22302.

[48] Notholt J, Kuang Z, Rinsland CP, Toon GC, Rex M, Jones N, Albrecht T, Deckelmann H, Krieg J, Weinzierl C, Bingemer H, Weller R, Schrems O. Enhanced upper tropical tropospheric COS: impact on the stratospheric aerosol layer. *Science* 2003;10:307.

[49] Montzka SA, Calvert P, Hall BD, Elkins JW, Conway TJ, Tans PP, Sweeney C. On the global distribution, seasonality, and budget of atmospheric carbonyl sulfide (COS) and some similarities to CO_2. *Geophys Res Lett* 2007;112:D09302.

[50] Crutzen PJ. The possible importance of CSO for the sulfate layer of the stratosphere. *Geophys Res Lett* 1976;3:73.

[51] Chin M, Davis DD. A reanalysis of carbonyl sulfide as a source of stratospheric background sulfur aerosol. *Geophys Res Lett* 1995;100:8993.

[52] Burkholder JB, Sander SP, Abbatt JPD, Barker JR, Huie RE, Kolb CE, Kurylo MJ, Orkin VL, Wilmouth DM, Wine PH. Chemical kinetics and photochemical data for use in atmospheric studies: Evaluation number 18. *Jet Propulsion Laboratory* 2015.

[53] Danielache SO, Johnson MS, Nanbu S, Grage MML, McLinden CA, Yoshida N. Ab initio study of sulfur isotope fractionation in the reaction of OCS with OH. *Chem Phys Lett* 2008;450:214.

[54] Barkley MP, Palmer PI, Boone CD, Bernath PF. Global distributions of carbonyl sulfide in the upper troposphere and stratosphere. *Geophys Res Lett* 2008;35:L14810.

[55] Sedlacek WA, Mroz EJ, Lazrus AL, Gandrud BW. A decade of stratospheric sulfate measurements compared with observations of volcanic eruptions. *J Geophys Res: Oceans* 1983;88:3741

[56] Watts SF. The mass budgets of carbonyl sulfide, dimethyl sulfide, carbon disulfide and hydrogen sulfide. *Atmos Env* 2000;34:761

[57] Wilson JC, Lee SH, Reeves JM, Brock CA, Jonsson HH, Lafleur BG, et al.. Steady-state aerosol distributions in the extra-tropical, lower stratosphere and the processes that maintain them. *Atmos Chem Phys* 2008;8:6617.

[58] Bernath PF, Yousefi M, Buzan E, Boone CD. A Near-Global Atmospheric Distribution of N_2O Isotopologues. *Geophys Res Lett* 2017;44:10.

[59] Garofalo L, Kanu A, Hoag KJ, Boering KA. The effects of stratospheric chemistry and transport on the isotopic compositions of long-lived gases measured at Earth's surface. *Advances in Atmospheric Chemistry* 2018, (World Scientific).

[60] Castleman Jr AW, Munkelwitz HR, Manowitz B. Isotopic studies of the sulfur component of the stratospheric aerosol layer. *Tellus* 1974;26:222.

[61] Krysztofiak G, Veng Té Y, Catoire V, Berthet G, Toon GC, et al.. Carbonyl sulfide (OCS) variability with latitude in the atmosphere. *Atmosphere-Ocean* 2015;53:89.

[62] Leung FYT, Colussi AJ, Hoffmann MR, Toon GC. Isotopic fractionation of carbonyl sulfide in the atmosphere: Implications for the source of background stratospheric sulfate aerosol. *Geophys Res Lett* 2002;29:1474.

[63] Miller CE, Yung YL. Photo-induced isotopic fractionation. *Geophys Res Lett* 2000;105:29039.

[64] Collusi AJ, Leung FY, Hoffmann MR. Electronic spectra of carbonyl sulfide sulfur isotopologues. *Environmental Chemistry* 2004;1:44.

[65] Hattori S, Danielache SO, Johnson MS, Schmidt JA, Kjaergaard HG, Toyoda S, Ueno Y, Yoshida N. Ultraviolet absorption cross sections of carbonyl sulfide isotopologues $OC^{32}S$, $OC^{33}S$, $OC^{34}S$ and $O^{13}CS$: isotopic fractionation in photolysis and atmospheric implications. *Atmos Chem Phys* 2011;11:10293.

[66] Lin Y, Sim MS, Ono S. Multiple-sulfur isotope effects during photolysis of carbonyl sulfide. *Atmos Chem Phys Discuss* 2011;11:14233.

[67] Hattori S, Toyoda A, Toyoda S, Ishino S, Ueno Y, Yoshida N. Determination of the Sulfur Isotope Ratio in Carbonyl Sulfide Using Gas Chromatography/Isotope Ratio Mass Spectrometry on Fragment Ions $^{32}S^+$, $^{33}S^+$, and $^{34}S^+$. *Anal Chem* 2015;87:477.

[68] Leifer R. Project Airstream: OCS measurements in the stratosphere and troposphere. *J Geophys Res* 1989;94:5173.

[69] Engel A, Schmidt U. Vertical profile measurements of carbonyl sulfide in the stratosphere. *Geophys Res Lett* 1994;21:2219.

[70] Toon G C, L.Blavier J F, Sung K. Atmospheric carbonyl sulfide (OCS) measured remotely by FTIR solar absorption spectrometry. *Atmos Chem Phys* 2018;18:1923.

[71] Bernath PF, McElroy CT, Abrams MC, Boone CD, et al. Atmospheric Chemistry Experiment (ACE): Mission overview. *Geophys Res Lett* 2005;32:L15S01.

[72] Boone CD, Walker K, Bernath PF. Version 3 retrievals for the Atmospheric Chemistry Experiment Fourier Transform Spectrometer (ACE-FTS) in: P.F. Bernath (Ed.) The Atmospheric Chemistry Experiment ACE at 10: A Solar

Occultation Anthology. 2013;pp.103-127, (A. Deepak Publishing, Hampton, Virginia, USA).

[73] Rothman LS, Gordon IE, Barbe A, et al. The HITRAN 2008 Molecular Spectroscopic Database. *J Quant Spectrosc Radiat Transf* 2009;110:533.

[74] Velazco VA, Toon GC, Blavier JFL, Kleinböhl A, Manney GL, Daffer, et al.. Validation of the Atmospheric Chemistry Experiment by noncoincident MkIV balloon profiles. *J Geophys Res* 2011;116:D06306.

[75] Kuebbeler M, Lohmann U, Feichter J. Effects of stratospheric sulfate aerosol geo-engineering on cirrus clouds. *Geophys Res Lett* 2012;39:L23803.

[76] Schmidt JA, Johnson MS, Hattori S, Yoshida N, Nanbu S, Schinke R. OCS photolytic isotope effects from first principles: sulfur and carbon isotopes, temperature dependence and implications for the stratosphere. *Atmos Chem Phys* 2013;13:1511.

[77] Hattori S, Schmidt JA, Mahler DW, Danielache SO, Johnson MS, Yoshida N. Isotope effect in the Carbonyl Sulfide reaction with O(^{3}P). *J Phys Chem A* 2012;116:3521.

[78] Schmidt JA, Johnson MS, Jung Y, Danielache SO, Hattori S, Yoshida N. Predictions of the sulfur and carbon kinetic isotope effects in the OH+OCS reaction. *Chem Phys Lett* 2012;531:64.

[79] Yousefi M, Bernath PF, Line Lists for AlF and AlCl in the $X^1\Sigma^+$ Ground State, *Astrophys J Supp* 2018;10:237.

[80] Hedderich HG, Dulick M, Bernath PF, High resolution emission spectroscopy of AlCl at 20 μm, *J Chem Phys* 1993;99:8363–8370.

[81] Rogowski DF, Fontijn A, The radiative lifetime of AlCl $A^1\Pi$, *Chem Phys Lett* 1987;137:219–222.

[82] McGregor WK, Drakes JA, Beale KS, Sherrell FG, AlCl absorption feature in solid rocket plume radiation, *J Thermophys Heat Trans* 1993;7:736–739.

[83] Cernicharo J, Guélin M, Metals in IRC$^+$ 10216-Detection of NaCl, AlCl, and KCl, and tentative detection of AlF, *Astronom & Astrophys* 1987;183:L10–L12.

[84] Ziurys LM, Apponi AJ, Phillips TG, Exotic fluoride molecules in IRC+ 10216: confirmation of AlF and searches for MgF and CaF, *Astrophys J* 1994;433:729–732.

[85] Agúndez M, Fonfría JP, Cernicharo J, Kahane C, Daniel F, Guélin M, Molecular abundances in the inner layers of IRC$^+$ 10216, *Astronom & Astrophys* 2012;543:A48.

[86] Kwok S, Physics and Chemistry of the Interstellar Medium, 2007, (University Science Books).

[87] Tsuji TT, Molecular abundances in stellar atmospheres. II., *Astronom & Astrophys* 1973;23:411–431.

[88] Highberger JL, Savage C, Bieging JH, Ziurys LM, Heavy-metal chemistry in proto-planetary nebulae: Detection of MgNC, NaCN, and AlF toward CRL 2688, *Astrophys J* 2001;562:790.

[89] Decin L, Richards AMS, Waters LBFM, Danilovich T, Gobrecht D, Khouri T, Homan W, Bakker JM, Van de Sande M, Nuth JA, et al., Study of the aluminium content in AGB winds using ALMA-Indications for the presence of gas-phase (Al_2O_3) n clusters, *Astronom & Astrophys* 2017;608:A55.

[90] Asplund M, Grevesse N, Sauval AJ, Scott P, The chemical composition of the Sun, *Annual Review of Astronom & Astrophys* 2009;47:481–522.

[91] Lodders K, Fegley B, Chemistry of Low Mass Substellar Objects, *Astrophys Update 2* 2006:1–28, (Springer).

[92] Bernath PF, Molecular opacities for exoplanets, *Philos Trans A Math Phys Eng Sci* 2014;372:20130087.

[93] Mahieu E, Dubois I, Bredohl H, The $A^1\Pi$-$X^1\Sigma^+$ transition of AlCl, *J Mol Spec* 1989;134:317–328.

[94] Wyse FC, Gordy W, Millimeter wave rotational spectra of AlCl, AlBr, and AlI, *J Chem Phys* 1972;56:2130–2136.

[95] Hensel KD, Styger C, Jäger W, Merer AJ, Gerry MCL, Microwave spectra of metal chlorides produced using laser ablation, *J Chem Phys* 1993;99:3320–3328.

[96] Hedderich HG, Bernath PF, The infrared emission spectrum of gaseous AIF, *J Mol Spec* 1992;153:73–80.

[97] Zhang KQ, Guo B, Braun V, Dulick M, Bernath PF, Infrared emission spectroscopy of BF and AlF, *J Mol Spec* 1995;170:82–93.

[98] Horiai K, Uehara H, Infrared diode laser spectroscopy of the Δv= 2 band of AlF, *Spectrochim Acta A: Mol Biomol Spec* 2006;63:1009–1012.

[99] Hoeft J, Lovas FJ, Tiemann E, Törring T, Microwave absorption spectra of AlF, GaF, InF, and TIF, *Zeitschrift für Naturforschung A* 1970;25:1029–1035.

[100] Lide Jr, David R, High-Temperature Microwave Spectroscopy: AlF and AlCl, *J Chem Phys* 1965;42:1013–1018.

[101] Wan M, Yuan Di, Jin C, Wang F, Yang Y, Yu Y, Shao J, Laser cooling of the AlCl molecule with a three-electronic-level theoretical model, *J Chem Phys* 2016;145:024309.

[102] Werner H, Knowles PJ, Knizia G, Manby FR, Schütz M, Wiley Interdiscip, *Rev: Comput Mol Sci* 2012;2:242–253.

[103] Bauschlicher CW, Langhoff SR, Komornicki A, The calculation of the dipole moments of NiH, TiO, and FeO, *Theoretica Chimica Acta* 1990;77:263–279.

[104] Frohman DJ, Bernath PF, Brooke, James SA, Molecular line lists: The ro-vibrational spectra of NaF and KF, *J Quant Spectrosc Radiat Transf* 2016;169:104–110.

[105] Le Roy RJ, dPotFit: A computer program to fit diatomic molecule spectral data to potential energy functions, *J Quant Spectrosc Radiat Transf* 2017;186:179–196.

[106] Le Roy RJ, RKR1: A computer program implementing the first-order RKR method for determining diatomic molecule potential energy functions, *J Quant Spectrosc Radiat Transf* 2017;186:158–166.

[107] Le Roy RJ, Pashov A, betaFIT: A computer program to fit pointwise potentials to selected analytic functions, *J Quant Spectrosc Radiat Transf* 2017;186:210–220.

[108] Barton EJ, Chiu C, Golpayegani S, Yurchenko SN, Tennyson J, Frohman DJ, Bernath PF, ExoMol molecular line lists V: The ro-vibrational spectra of NaCl and KCl, *Monthly Notices of the Royal Astronomical Society* 2014;442:1821–1829.

[109] Le Roy RJ, Improved parameterization for combined isotopomer analysis of diatomic spectra and its application to HF and DF, *J Mol Spec* 1999;194:189–196.

[110] Le Roy RJ, Huang Y, Representing Born–Oppenheimer breakdown radial correction functions for diatomic molecules, *J Mol Struct: THEOCHEM* 2002;591:175–187.

[111] Le Roy RJ, LEVEL: A computer program for solving the radial Schrödinger equation for bound and quasibound levels, *J Quant Spectrosc Radiat Transf* 2017;186:167–178.

[112] Langhoff SR, Bauschlicher Jr CW, Taylor PR, Theoretical studies of AlF, AlCl, and AlBr, *J Chem Phys* 1988;88:5715–5725.

[113] Brites V, Hammoutène D, Hochlaf M, Spectroscopy, metastability, and single and double ionization of AlCl, *Journal Phys Chem A* 2008;112:13419–13426.

[114] Herman R, Wallis RF, Influence of Vibration-Rotation Interaction on Line Intensities in Vibration-Rotation Bands of Diatomic Molecules, *J Chem Phys* 1955;23:637–646.

[115] Medvedev ES, Meshkov VV, Stolyarov AV, Ushakov VG, Gordon IE, Impact of the dipole-moment representation on the intensity of high overtones, *J Mol Spec* 2016;330:36–42.

[116] Pickett HM, The fitting and prediction of vibration-rotation spectra with spin interactions, *J Mol Spec* 1991;148:371–377.

[117] Yousefi M, Bernath PF, Hodges J, Masseron T. A new line list for the $A^2\Sigma^+$–$X^2\Pi$ electronic transition of OH. *J Quant Spectrosc Radiat Transf* 2018;217:416–424.

[118] Prinn RG, Weiss RF, Miller BR, Huang J, Alyea FN, Cunnold DM, et al. Atmospheric trends and lifetime of CH_3CCl_3 and global OH concentrations. *Science* 1995;269:187–92.

[119] Atkinson R, Arey J. Atmospheric degradation of volatile organic compounds. *Chem Rev* 2003;103(12):4605–38.

[120] Lelieveld J, Dentener FJ, Peters W, Krol MC. On the role of hydroxyl radicals in the self-cleansing capacity of the troposphere. *Atmos Chem Phys* 2004;4:2337–44.

[121] Mélendez J, Barbuy B. Keck NIRSPEC Infrared OH Lines: Oxygen Abundances in Metal-poor Stars down to [Fe/H] =–2.9*. *Astrophys J* 2002;575:474–483.

[122] Asplund M, Grevesse N, Sauval AJ, Allende Prieto C, Kiselman D. Line formation in solar granulation IV. [OI], OI and OH lines and the photospheric O abundance. *Astron Astrophys* 2004;417:751–768.

[123] Goicoechea JR and Cernicharo J. Far-Infrared OH Fluorescent Emission in Sagittarius B2*. *Astrophys J* 2002;576:L77.

[124] Piccioni G, Drossart P, Zasova L, Migliorini A, Gérard JC, Mills FP, Shakun A, García Muñoz A, Ignatiev N, Grassi D, Cottini V, Taylor FW, Erard S and the VIRTIS-Venus Express Technical Team. First detection of hydroxyl in the atmosphere of Venus. *Astrophys J* 2008;483:L29 - L33.

[125] Meinel AB. OH Emission Bands in the Spectrum of the Night Sky. II. *Astrophys J* 1950;112:120.

[126] Cosby PC, Slanger TG. OH spectroscopy and chemistry investigated with astronomical sky spectra. *Can J Phys* 2007;85(2):77-99.

[127] Grevesse N, Sauval AJ, van Dishoeck EF. An analysis of vibration-rotation lines of OH in the solar infrared spectrum. *Astron Astrophys*. 1984;141:10-6.

[128] Goldman A, Murcray DG, Lambert DL, Dominy JF. The pure rotation spectrum of the hydroxyl radical and the solar oxygen abundance. *Mon Not R Astron Soc* 1983;203:767–76.

[129] Settersten TB, Farrow RL, Gray JA. Infrared–ultraviolet double–resonance spectroscopy of OH in a flame. *Chem Phys Lett* 2003;369:584–590.

[130] Coxon JA. Optimum molecular constants and term values for the $X^2\Pi$ ($v\leq 5$) and $A^2\Sigma^+$ ($v\leq 3$) states of OH. *Can J Phys* 1980;58(7):933-949.

[131] Engleman Jr. R. Accurate wavenumbers of the $A^2\Sigma^+-X^2\Pi$ (0, 0) and (1, 0) bands of OH and OD. *J Quant Spectrosc Radiat Transf* 1972;12:1347-1350.

[132] Dieke GH, Crosswhite HM. The ultraviolet bands of OH: Fundamental data. *J Quant Spectrosc Radiat Transf* 1962;2:97-199.

[133] Maillard JP, Chauville J, Mantz AW. High-resolution emission spectrum of OH in an oxyacetylene flame from 3.7 to 0.9 μm. *J Mol Spectrosc* 1976;63:120-141.

[134] Coxon JA, Sappey AD, Copeland RA. Molecular constants and term values for the hydroxyl radical, OH: The $X^2\Pi$ ($v= 8, 12$), $A^2\Sigma^+$ ($v= 4-9$), $B^2\Sigma^+$ ($v= 0, 1$) and $C^2\Sigma^+$ ($v= 0, 1$) states. *J Mol Spectrosc* 1991;145:41-55.

[135] Carlone C, Dalby FW. Spectrum of the hydroxyl radical. *Canad J Phys* 1969;47:1945-1957.

[136] Coxon JA, Foster SC. Rotational analysis of hydroxyl vibration-rotation emission bands: Molecular constants for OH $X^2\Pi$, $6\leq v\leq 10$. *Canad J Phys* 1982;60:41-48.

[137] Sappey AD, Copeland RA. Laser double-resonance study of OH ($X^2\Pi_i$, $v = 12$). *J Mol Spectrosc* 1990;143:160-168.

[138] Copeland RA, Jeffries JB, Crosley DR. The OH $A^2\Sigma^+-X^2\Pi$ (4,2) band: Line positions and line widths. *J Mol Spectrosc* 1990;143:183-185.

[139] Stark G, Brault JW, Abrams MC. Fourier-transform spectra of the $A^2\Sigma^+-X^2\Pi$ $\Delta v= 0$ bands of OH and OD. *J Opt Soc Am B* 1994;11:3-32.

[140] Gordon IE, Rothman LS, Hill C, Kochanov RV, Tan Y, Bernath PF, et al. The HITRAN 2016 molecular spectroscopic database. *J Quant Spectrosc Radiat Transf* 2017;203:3-69.

[141] Gillis JR, Goldman A, Stark G, Rinsland CP. Line parameters for the $A^2\Sigma^+-X^2\Pi$ bands of OH. *J Quant Spectrosc Radiat Transf* 2001;68:225-230.

[142] Luque J, Crosley DR. LIFBASE: Database and spectral simulation program (v.2.0). *SRI International Report MP* 1999:99-009.

[143] Luque J, Crosley DR. Transition probabilities in the $A^2\Sigma^+-X^2\Pi$ electronic system of OH. *J Chem Phys* 1998;109:439.

[144] Abrams MC, Davis SP, Rao MLP, Engleman, Jr. R., Brault, JW. High-resolution Fourier transform spectroscopy of the Meinel system of OH. *Astrophys J Sup* 1994;93:351-395.

[145] Mélen F, Sauval AJ, Grevesse N, Farmer CB, Servais Ch, Delbouille L, Roland G. A New Analysis of the OH Radical Spectrum from Solar Infrared Observations. *J Mol Spectrosc* 1995;174:490-509.

[146] Goldman A, Schoenfeld WG, Goorvitch D, Chackerian Jr C, Dothe H, Mélen F, Abrams MC, Selby JEA. Updated line parameters for OH $X^2\Pi-X^2\Pi$ (v''-v') transitions. *J Quant Spectrosc Radiat Transf* 1998;59:543-469.

[147] Bernath PF, Colin R. Revised molecular constants and term values for the $X^2\Pi$ and $B^2\Sigma^+$ states of OH. *J Mol Spectrosc* 2009;257:20–23.

[148] Brooke JSA, Bernath PF, Western CM, Sneden C, Afşar M, Li G, Gordon IE. Line strengths of rovibrational and rotational transitions in the $X^2\Pi$ ground state of OH. *J Quant Spectrosc Radiat Transf* 2016;168:142-157.

[149] Crosley DR, Lengel RK. Relative transition probabilities and the electronic transition moment in the A$-$X system of OH. *J Quant Spectrosc Radiat Transf* 1975;15:579-591.

[150] Wang CC and Killinger DK. Effect of rotational excitation on the band oscillator strength of OH. *Phys Rev A* 1979;20:1495.

[151] Bauschlicher Jr. CW and Langhoff SR. Theoretical determination of the radiative lifetime of the $A^2\Sigma^+$ state of OH. *J Chem Phys* 1987;87:4665.

[152] Bittencourt ACP, Prudente FV, Vianna JDM. The fitting of potential energy and transition moment functions using neural networks: transition probabilities in OH ($A^2\Sigma^+-X^2\Pi$). *Chem Phys* 2004;297:153-161.

[153] Derro EL, Pollack IB, Dempsey LP, Greenslade ME, Lei Y, Radenović DČ, Lester MI. Fluorescence-dip infrared spectroscopy and predissociation dynamics of OH $A^2\Sigma^+$ (v=4) radicals. *J Chem Phys* 2005;122:244313.

[154] Yarkony DR. A theoretical treatment of the predissociation of the individual rovibronic levels of OH/OD ($A^2\Sigma^+$). *J Chem Phys* 1992;97:1838.

[155] Werner HJ, Knowles PJ, Knizia G, Manby FR, Schütz M. Molpro: a general-purpose quantum chemistry program package. *J Chem Phys* 2011;2:242-253.

[156] Western CM. PGOPHER: A program for simulating rotational, vibrational and electronic spectra. *J Quant Spectrosc Radiat Transf* 2017;186:221-242.

[157] Peterson KA, Dunning Jr. TH. Accurate correlation consistent basis sets for molecular core-valence correlation effects: The second row atoms Al-Ar, and the first row atoms B-Ne revisited. *J Chem Phys* 2002;117:10548.

[158] LeRoy RJ. RKR1: A computer program implementing the first-order RKR method for determining diatomic molecule potential energy functions. *J Quant Spectrosc Radiat Transf* 2017;186:158-166.

[159] LeRoy RJ. LEVEL: A computer program for solving the radial Schrödinger equation for bound and quasibound levels. *J Quant Spectrosc Radiat Transf* 2017;186:167-178.

[160] Herman R, Wallis RF. Influence of Vibration-Rotation Interaction on Line Intensities in Vibration-Rotation Bands of Diatomic Molecules. *J Chem Phys* 1955;23:637.

[161] Chackerian Jr. C, Guelachvili G, Piñeiro AL, Tipping RH. Rovibrational intensities for the Δv= 1 bands of the $X^3\Sigma^-$ NH radical: Experiment and theory. *J Chem Phys* 1989;90:641.

[162] Medvedev ES, Ushakov VG, Stolyarov AV, Gordon IE. Intensity anomalies in the rotational and ro-vibrational spectra of diatomic molecules. *J Chem Phys* 2016;147:164309.

[163] German KR. Direct measurement of the radiative lifetimes of the $A^2\Sigma^+$ (v'=0) states of OH and OD. *J Chem Phys* 1975;62:2584.

[164] Copeland RA, Jeffries JB, Crosley DR. Transition probabilities in OH $A^2\Sigma^+-X^2\Pi_i$: bands with v'=0 and 1, v''=0 to 4 . *Chem Phys Lett* 1987;138:425-430.

[165] Billoux T, Cressault Y, Gleizes A. Tables of radiative transition probabilities for the main diatomic molecular systems of OH, CH, CH^+, CO and CO^+ occurring in CO-H_2 syngas-type plasma. *J Quant Spectrosc Radiat Transf* 2014;133:434-444.

[166] Kurucz RL, Furenlid I, Brault J, Testerman L. Solar Flux Atlas from 296 to 1300 nm. *NSO Atlas No. 1.* 1984.

[167] Dekker H, D'Odorico S, Kaufer A, Delabre B, Kotzlowski H. Design, construction, and performance of UVES, the echelle spectrograph for the UT2 Kueyen Telescope at the ESO Paranal Observatory. *Proc SPIE* 2000;184:534-545.

[168] Gray DF. The Observation and Analysis of Stellar Photospheres, 3rd Edition. 2005, (*Cambridge University Press).*

[169] Masseron T, Johnson J, Plez B, van Eck S, Primas F, Goriely S, Jorissen A. A holistic approach to carbon-enhanced metal-poor stars. *Astron Astrophys* 2010;509:A93.

[170] Ryabchikova T, Piskunov N, Kurucz RL, Stempels HC, Heiter U, Pakhomov Yu, Barklem PS. A major upgrade of the VALD database. *Phys. Scr.* 2015;90:054005.

[171] Fernando AM, Bernath PF, Hodges JN, Masseron T. A new line list for the $A^3\Pi - X^3\Sigma^-$ transition of the NH free radical. *J Quant Spectrosc Radiat Transf* 2018;217:29-34.

[172] Swain MR, Deroo P, Griffith CA, Tinetti G, Thatte A, Vasisht G, et al. A ground-based near-infrared emission spectrum of the exoplanet HD 189733b. *Nature* 2010;463:637.

[173] Guillot T, Gautier D. Giant Planets. *Treatise on Geophys* 2015; 2nd edition, (Elsevier).

[174] Venot O, Agundez M, Selsis F, Tessenyi M, Iro N. The atmospheric chemistry of the warm Neptune GJ 3470b: influence of metallicity and temperature on the CH_4/CO ratio. *Astron Astrophys* 2013;562:A51.

[175] Moses JI, Line, MR, Visscher C, Richardson MR, Nettelmann N, Fortney JJ, et al. Compositional diversity in the atmospheres of hot Neptunes, with application to GJ 436b. *Astrophys J* 2013;777:34.

[176] Miller-Ricci E, Fortney JJ. The nature of the atmosphere of the transiting super-Earth GJ 1214b. *Astrophys J Lett* 2010;716:L74.

[177] Hand E. Super-Earths give theorists a super headache. *Nature* 2011;480:302.

[178] Marley MS, Robinson TD. On the cool side: modeling the atmospheres of brown dwarfs and giant planets. *Ann Rev Astro Astrophys* 2015;53:279.

[179] Owen JE. Atmospheric escape and the evolution of Close in Exoplanets. *Ann Rev Earth Planetary Sciences* 2019;47:67.

[180] Orton GS, Fletcher LN, Moses JI, Mainzer AK, Hines D, Hammel HB, et al. Mid-infrared spectroscopy of Uranus from the Spitzer Infrared Spectrometer: 1. Determination of the mean temperature structure of the upper troposphere and stratosphere. *Icarus* 2014;243:494.

[181] Lodders K. Exoplanet Chemistry 2010;ch 8:157, (*John Wiley & Sons, Ltd).*

[182] Guilluy G, Sozzetti A, Brogi M, Bonomo AS, Giacobbe P, Claudi R, et al. Exoplanet atmospheres with GIANO–II. Detection of molecular absorption in the dayside spectrum of HD 102195b. *Astron Astrophys* 2019;625:A107.

[183] Beaulieu JP, Tinetti G, Kipping DM, Ribas I, Barber RJ, Cho JK, et al. Methane in the atmosphere of the transiting hot Neptune GJ436b?. *Astrophys J* 2011;731:16.

[184] Venot O, Agúndez M, Selsis F, Tessenyi M, Iro N. The atmospheric chemistry of the warm Neptune GJ 3470b: Influence of metallicity and temperature on the CH_4/CO ratio. *Astron Astrophys* 2014;562:A51.

[185] Visscher C, Moses JI. Quenching of carbon monoxide and methane in the atmospheres of cool brown dwarfs and hot Jupiter. *Astrophys J* 2011;738:72.

[186] Moses JI, Visscher C, Fortney JJ, Showman AP, Lewis NK, Griffith CA, et al.. Disequilibrium carbon, oxygen, and nitrogen chemistry in the atmospheres of HD 189733b and HD 209458. *Astrophys J* 2011;737:15.

[187] Line MR, Vasisht G, Chen P, Angerhausen D, Yung YL. Thermochemical and photochemical kinetics in cooler hydrogen-dominated extrasolar planets: a methane-poor GJ436b?. *Astrophys J* 2011;738:32.

[188] Seager SV, Sasselov DD. Theoretical transmission spectra during extrasolar giant planet transits. *Astrophys J* 2000;537:916.

[189] Yurchenko SN, Tennyson J, Bailey J, Hollis MDJ, Tinetti G. Spectrum of hot methane in astronomical objects using a comprehensive computed linelist. *Proc Nat Acad Sci* 2014;111:9379.

[190] Varanasi P, Chudamani S. The temperature-dependence of lineshifts, linewidths and line intensities of methane at low temperatures. *J Quant Spectrosc Radiat Transf* 1990;43:1.

[191] Pine AS. Self-, N_2, O_2, H_2, Ar, and He broadening in the ν_3 band Q branch of CH_4. *J Chem Phys* 1992;97:773.

[192] Es-Sebbar ET, Farooq A. Intensities, broadening and narrowing parameters in the ν_3 band of methane. *J Quant Spectrosc Radiat Transf* 2014;149:241.

[193] Gharib-Nezhad E, Heays AN, Bechtel HA, Lyons JR. H_2-induced Pressure-induced broadening and pressure shift in the P-branch of the ν_3 band of CH_4 from 300 to 655 K. *J Quant Spectrosc Radiat Transf* 2019;239:106649.

[194] Fortney JJ. Modeling Exoplanetary Atmospheres: An Overview (A chapter from Astrophysics of Exoplanetary Atmospheres). (Springer) 2018;450:51.

[195] Pine AS, Gabard T. Multispectrum fits for line mixing in the ν_3 band Q branch of methane. *J Mol Spec* 2003;217:105.

[196] Smith MAH, Rinsland CP, Devi VM, Benner DC. temperature-dependence of broadening and shifts of methane lines in the ν_4 band. *Spectrochemica Acta* 1992;48:1257.

[197] Anderson PW. Pressure-induced broadening in the microwave and infra-red regions. *Physical Review.* 1949;76:647.

[198] Neshyba SP, Lynch R, Gamache, R, Gabard T, Champion JP. Pressure-induced widths and shifts for the ν_3 band of methane. *J Chem Phys* 1994;101:9412.

[199] Gabard, T. Calculated line broadening parameters for methane perturbed by diatomic molecules. *J Mol Spec* 2013;291:61.

[200] Smith LN, Secrest D. Close-coupling and coupled state calculations of argon scattering from normal methane. *J Chem Phys* 1981;74:3882.

[201] Tennyson J, Bernath PF, Campargue A, Császár AG, Daumont L, Gamache RR, et al. Recommended isolated-line profile for representing high-resolution spectroscopic transitions (IUPAC Technical Report). *Pure Appl Chem* 2014;86:1931.

[202] Wilzewski JS, Birk M, Loos J, Wagner G. Temperature-dependence laws of absorption lineshape parameters of the CO_2 ν_3 band. *J Quant Spectrosc Radiat Transf* 2018;206:296.

[203] Gamache RR, Vispoel B. On the temperature-dependence of half-widths and line shifts for molecular transitions in the microwave and infrared regions. *J Quant Spectrosc Radiat Transf* 2018;217:440.

[204] Delahaye T, Ghysels M, Hodges JT, Sung K, Armante R, Tran H. Measurement and modeling of air-broadened methane absorption in the MERLIN spectral region at low temperatures. *J Geophys Res: Atmospheres* 2019;124:3556.

[205] Rosenkranz P. Shape of the 5 mm oxygen band in the atmosphere. *IEEE Trans Antennas Propagat* 1975;23:498.

[206] Hartmann JM, Boulet C, Robert D. Collisional effects on molecular spectra: laboratory experiments and models, consequences for applications, 2008, (Elsevier).

[207] Hargreaves RJ, Bernath PF, Bailey J, Dulick M. Empirical linelists and absorption cross sections for methane at high temperatures. *Astrophys J* 2015;813:12.

[208] Pieroni D, Nguyen-Van-Thanh, Brodbeck C, Claveau C, Valentin A, Hartmann JM, et al. Experimental and theoretical study of line mixing in methane spectra. I. The N_2-broadened ν_3 band at room temperature. *J Quant Spectrosc Radiat Transf* 1999;110:7717.

[209] Tang MJ, Shiraiwa M, Pöschl U, Cox RA, Kalberer M. Compilation and evaluation of gas phase diffusion coefficients of reactive trace gases in the atmosphere: Volume 2. Diffusivities of organic compounds, pressure-normalised mean

free paths, and average Knudsen numbers for gas uptake calculations. *Atmos Chem Phys* 2015;15:5585.

[210] Boone CD, Walker KA, Bernath PF. An efficient analytical approach for calculating line mixing in atmospheric remote sensing applications. *J Quant Spectrosc Radiat Transf* 2011;112:980.

VITA

Mahdi Yousefi Atashgah
Department of Physics
Old Dominion University
Norfolk, VA 23529

Education

Ph.D. Physics Old Dominion University, US, *May 2020*

M.Sc. Physics Old Dominion University, US, *May 2015*

M.Sc. Plasma engineering Shahid Beheshti University, Iran, *August 2011*

B.Sc. Physics Tabriz University, Iran, *December 2007*

Publications

H Ghomi, M Yousefi, N Shahabi, M Khoramabadi. Ultrasonic-assisted spark plasma discharge for gold nanoparticles synthesis. *Radiation Effects and Defects in Solids*, **2013**, 68 (11-12), 881-891.

M Yousefi, V Damideh, H Ghomi. Low-energy electron beam extraction from spherical discharge. *IEEE Transactions on Plasma Science*, **2011**, 39 (11), 2554-2555.

PF Bernath, M Yousefi, E Buzan, CD Boone. A Near-Global Atmospheric Distribution of N_2O Isotopologues. *Geophysical Research Letters*, **2017**, 44 (20), 10,735-10,743.

M Yousefi, PF Bernath, J Hodges, T Masseron. A new line list for the $A^2\Sigma^+$-$X^2\Pi$ electronic transition of OH. *Journal of Quantitative Spectroscopy and Radiative Transfer*, **2018**, 217, 416-424.

M Yousefi, PF Bernath. Line Lists for AlF and AlCl in the $X^1\Sigma^+$ Ground State. *The Astrophysical Journal Supplement Series*, **2018**, 237 (1), 8.

M Yousefi, PF Bernath, CD Boone, GC Toon. Global Measurements of Atmospheric OCS, $OC^{34}S$ and $O^{13}CS$. *Journal of Quantitative Spectroscopy and Radiative Transfer*, **2019**, 238,106554.